NiTi SHAPE MEMORY ALLOY THIN FILMS AND HETEROSTRUCTURES

A THESIS

*Submitted in partial fulfilment of the
requirements for the award of the degree*
of
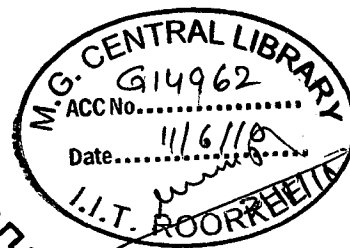DOCTOR OF PHILOSOPHY
in
METALLURGICAL AND MATERIALS ENGINEERING

by
ASHVANI KUMAR

DEPARTMENT OF METALLURGICAL AND MATERIALS ENGINEERING
INDIAN INSTITUTE OF TECHNOLOGY ROORKEE
ROORKEE - 247 667 (INDIA)
JULY, 2009

INDIAN INSTITUTE OF TECHNOLOGY ROORKEE
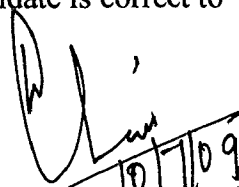## ROORKEE

CANDIDATE'S DECLARATION

I hereby certify that the work which is being presented in the thesis entitled **NiTi Shape Memory Alloy Thin Films and Heterostructures** in partial fulfilment of the requirement for the award of the Degree of Doctor of Philosophy and submitted in the Department of Metallurgical and Materials Engineering of the Indian Institute of Technology Roorkee, Roorkee is an authentic record of my own work carried out during a period from July 2006 to July 2009 under the supervision of Dr. Davinder Kaur, Assistant Professor, Department of Physics & Center of Nanotechnology and Dr. Devendra Singh, Assistant Professor, Department of Metallurgical and Materials Engineering, Indian Institute of Technology Roorkee, Roorkee.

The matter presented in this thesis has not been submitted by me for the award of any other degree of this or any other Institute.

(ASHVANI KUMAR)

This is to certify that the above statement made by the candidate is correct to the best of our knowledge.

(Devendra Singh)
Supervisor

(Davinder Kaur)
Supervisor

Date: JULY 10, 2009

The Ph. D. Viva-Voce Examination of **Mr. Ashvani Kumar**, Research Scholar, has been held on ....

Signature of Supervisors

Signature of External Examiner

ABSTRACT

Shape memory alloy (SMA) thin films of Nickel-Titanium (NiTi) have attracted much attention in recent years as intelligent and functional materials due to their unique properties i.e. superelasticity and shape memory effect, which enable them to be widely used in aerospace, micro-electromechanical systems (MEMS) and various biomedical applications. The phase transformation in SMA thin film is accompanied by significant changes in the mechanical, physical, electrical and optical properties, which could be made use in the design and fabrication of microsensors and micro-actuators. However, there are still some concerns for the wide application of SMA thin films because of their unsatisfactory mechanical and tribological performances, chemical resistance and biological reliability. High nickel content in NiTi alloys often stimulated suspicions for their medical use. The limited hardness and wear resistance of NiTi make it difficult to be used in orthodontic and MEMS applications. Therefore, there is the need to search for stable, corrosion resistance and biocompatible protective coating for biomedical and MEMS applications of NiTi SMA thin films.

The main aim of the present work was to synthesize high quality nanostructured NiTi thin films and TiN/NiTi heterostructures on silicon substrate by magnetron sputtering process in order to (i) study the influence of grain size and film thickness on the texture, surface morphology and phase transformation behavior of NiTi thin films; (ii) study the effect of crystallographic orientation of nanocrystalline TiN thin film on structural, electrical and mechanical properties of TiN/NiTi heterostructures and (iii) demonstrate the applications of TiN/NiTi heterostructures in bio-molecule sensing. A chapter- wise summary of the thesis is given below:

Chapter 1 gives an overview of shape memory alloys and material background. The chapter includes the discussions on synthesis and properties of NiTi SMA thin films. The proper passivation to prevent surface layer degradation of NiTi thin films has also been discussed.

Chapter 2 presents the details of experimental techniques, which we have used for the synthesis and study of the properties of SMA thin films. **Section 2.1 -** Synthesis of thin films in present thesis has been carried out by dc magnetron sputtering technique. We have developed the setup of dc magnetron co-sputtering and optimized various sputtering parameters to obtain good quality equiatomic NiTi thin films. **Section 2.2 -** Gives an overview of characterization techniques used for present work. X-Ray Diffractometer has been used for the phase identification and texture analysis. Surface morphology and microstructure were studied using Field Emission Scanning Electron Microscopy (FE-SEM) and Atomic Force Microscopy (AFM). Transmission Electron Microscopy (TEM) was used for phase identification and high resolution imaging. Phase transformation behavior of these films was studied using four probe electrical resistivity set up. Further mechanical and electrochemical properties of the films were studied using nanoindenter and voltammetric analyzer.

Chapter 3 describes the growth and characterization of NiTi thin films prepared by dc magnetron sputtering technique. This chapter is divided into two sections. The first section (**Section 3.1**) mainly describes the effect of grain size on structural, electrical and mechanical properties of NiTi thin films. The grain size and the crystallization extent increased with increase in substrate temperature. Electrical resistance versus temperature plots show that grain size of NiTi films plays an important role in their electrical properties. The films with grain size ~ 20 nm exhibited negative TCR value and non metallic behavior while the film with grain size ≥33 nm showed metallic behavior. An interesting martensite to austenite phase transformation was observed as crystal structure changes from monoclinic to cubic upon heating close to room temperature. Nanoindentation studies revealed relatively low surface roughness, high hardness, high reduced elastic modulus and better wear behavior for the film exhibited austenite structure at room temperature in comparison to that exhibited martensitic structure. **Section 3.2-** describes the influence of film thickness on phase transformation behavior of NiTi thin films. XRD results revealed the presence of austenitic (110) reflection from the beginning that could be due to the minimum surface energy of (110) plane in bcc structures. Reflection from austenitic

(211) plane was also observed in the films of higher thickness ($\geq$ 2.3 μm) because of strain energy minimization with increasing thickness. Ni_3Ti precipitate formation was initiated as the film thickness reached to 2.3 μm and the fraction of precipitate formation increased with increasing thickness. AFM results indicated that even with increasing the film thickness, grains follows the Gaussian distribution. Electrical resistance versus temperature curves showed that the film with thickness $\leq$ 300 nm experiences resistance force due to film and substrate inter-diffusion and small grain size, which affects the phase transformation behavior in these films. However, the films with thickness 634 nm and 1.2 μm showed the martensite $\leftrightarrow$ austenite phase transformation via R-phase, which are the suitable candidates for actuators applications. The 2.3 μm thick film displayed the phase transformation behavior with shift in transformation temperatures towards lower temperature values because of the Ni_3Ti precipitate formation and the film of 3.4 μm thickness showed suppression of shape memory behavior that could be due to the increased fraction of precipitate formation.

Chapter 4 describes the deposition of nanocrystalline TiN/NiTi thin films on silicon substrate by dc magnetron sputtering to improve the surface and mechanical properties of NiTi thin films without sacrificing the phase transformation effect. The preferential orientation of the TiN films was observed to change from (111) to (200) with change in nature of sputtering gas from 70% Ar + 30% N_2 to 100% N_2. It was observed that TiN (200)/NiTi films exhibited high hardness, high elastic modulus, and thereby better wear resistance as compared to pure NiTi and TiN (111)/NiTi films. In addition the presence of TiN (200) improves the top surface quality of NiTi films while retaining the phase transformation effect.

Chapter 5 describes the electrochemical properties of TiN/NiTi heterostructures and their applications in electrochemical sensing. In the present investigation, the prepared TiN/NiTi heterostructures have been tested for first time as working electrode for dopamine sensing. Dopamine is a catecholamine neurotransmitter generated in various parts of central and peripheral nervous system, hence, careful monitoring of dopamine concentration is considered necessary. Parkinson's disease, associated with tremor, rigidity, bradykinesia and postural

instability, is one of the most dreadful neurodegenerative disorders of central nervous system (CNS). The disease occurs when dopaminergic neurons decrease or malfunction which is accompanied by a sharp decline in dopamine level. TiN (200)/NiTi coated silicon electrode showed straight line calibration in dopamine concentration range 1-10 μM with correlation coefficient of 0.995. Further electrochemical test reveals that TiN coated NiTi film exhibited better corrosion resistance.

Chapter 6 presents the summary and conclusion of the entire work presented in the thesis and also proposes the future directions in which these studies can be extended.

ACKNOWLEDGEMENTS

LIST OF FIGURES

LIST OF TABLES

LIST OF PUBLICATIONS

Paper published in journals

1. Fabrication and nanoindentation properties of TiN/NiTi thin films and their applications in electrochemical sensing.
   Ashvani Kumar, Devendra Singh, Rajendra N. Goyal and Davinder Kaur
   Talanta, 78, 964-969 (2009).

2. Grain size effect on structural, electrical and mechanical properties of NiTi thin films deposited by magnetron co-sputtering.
   Ashvani Kumar, Devendra Singh and Davinder Kaur
   Surface and Coating Technologies, 203, 1596-1603 (2009).

3. Effect of crystallographic orientation of nanocrystalline TiN on structural, electrical and mechanical properties of TiN/NiTi thin films
   Ashvani Kumar, Devendra Singh, Ravi Kumar and Davinder Kaur
   Journal of alloys and compound, 479, 166-172 (2009).

4. Nanoindentation and corrosion studies of TiN/NiTi thin films for biomedical applications.
   Ashvani Kumar and Davinder Kaur
   Surface and Coating Technology, doi:10.1016/j.surfcoat.2009.06.002, (2009).

5. Influence of film thickness on phase transformation behavior of sputtered NiTi shape memory alloy thin films
   Ashvani Kumar, Devendra Singh and Davinder Kaur
   Applied Physics A, Communicated

6. Fabrication of α-Fe2O3 nanopowder modified glassy carbon electrode for applications in electrochemical sensing
   Rajendra N. Goyal, Ashish K. Pandey, Davinder Kaur and **Ashvani Kumar**
   Journal of Nanoscience and Nanotechnology, 9, 4692-4699 (2009).

7. Structural and optical properties of nano crystalline V_2O_5 thin films.

   Ashvani Kumar, Preetam Singh and Davinder Kaur

   Thin Solid Films, 516, 912-918 (2008).

8. ZnO nanocrystalline powder synthesized by ultrasonic mist chemical vapor deposition.

   Preetam Singh, **Ashvani Kumar**, Deepak and Davinder Kaur

   Optical Materials, 30, 1316-1322 (2008).

9. Substrate effect on texture properties of nanocrystalline TiO_2 thin films.

   Preetam Singh, **Ashvani Kumar** and Davinder Kaur,

   Physica B, 403, 3769-3773 (2008).

10. Growth and characterization of ZnO nanocrystalline thin films and nanopowder via low cost ultrasonic spray pyrolysis.

    Preetam Singh, **Ashvani Kumar** and Davinder Kaur

    Journal of Crystal Growth, 306, 303-310 (2007).

11. Substrate effect on electrical transport properties of $RNiO_3$ thin films prepared by pulsed laser deposition.

    Ashvani Kumar, Preetam Singh, Davinder Kaur, John Jesudasan and Pratap Raychaudhuri

    Journal of Physics D: Applied Physics, 39, 5310-5315 (2006).

12. Low cost synthesis of high T_c-superconducting films on metallic substrates via ultrasonic spray pyrolysis.

    Ashvani Kumar, Preetam Singh and Davinder Kaur,

    Cryogenics, 46, 749-758 (2006).

Paper published in conferences

1. Nanoindentation and corrosion studies of TiN/NiTi thin films for biomedical applications.
   Ashvani Kumar and Davinder Kaur
   International Conference on Metallurgical Coatings and Thin Films **(ICMCTF)**
   Held at San Diego, California (USA) during April 23-27, 2009.

2. Magnetron sputtered graded nanostructured TiNi shape memory thin films.
   A. Kumar, P. Singh, A.K. Chawla, R. Chandra and D. Kaur
   International Conference on Metallurgical Coatings and Thin Films **(ICMCTF)**
   Held at San Diego, California (USA) during April 23-27, 2007.

3. Structural and optical Properties of V_2O_5 nanopowder and thin films.
   A. Kumar, P. Singh and D. Kaur
   International Conference on Metallurgical Coatings and Thin Films **(ICMCTF)**
   Held at San Diego, California (USA) during April 23-27, 2007.

4. Synthesis and characterization of TiN passivation layer over NiTi shape memory thin films.
   D. Kaur, **A. Kumar,**
   International Conference on Metallurgical Coatings and Thin Films **(ICMCTF)**
   Held at San Diego, California (USA) during April 23-27, 2007.

5. Structural and optical properties of nanocrystalline V_2O_5 thin films.
   Ashvani Kumar, Preetam Singh, and Davinder Kaur
   8th International Conference on Nanostructured Materials **(NANO 2006)**
   Held at Indian Institute of Science, Bangalore, India during August 20-25, 2006.

6.   Synthesis of nanocrystalline zinc oxide films by ultrasonic spray pyrolysis.

Amit Kumar Chawla, Preetam Singh, **Ashvani Kumar**, Davinder Kaur and Ramesh Chandra

8th International Conference on Nanostructured Materials **(NANO 2006)**

Held at Indian Institute of Science, Bangalore, India during August 20-25, 2006.

7.   Synthesis of transition metal oxide nanostructures by ultrasonic spray pyrolysis.

Preetam Singh, **Ashvani Kumar** and Davinder Kaur

Theme Meeting on Self-assembly Routes for Nanotech Materials **(SARNaM-06)**

Held at Bhabha Atomic Research Centre, India during April 26-28, 2006.

CONTENTS

Chapter 1

Introduction

CHAPTER 1

INTRODUCTION

1.1 Shape memory alloys

   1.1.1   Shape memory effect

   1.1.2   Pseudoelasticity

1.2 NiTi shape memory alloy

   1.2.1   Phase transformation in NiTi shape memory alloy

1.3 Shape memory alloys thin films

   1.3.1   NiTi shape memory alloy thin films

   1.3.2   TiN/NiTi heterostructures

1.4 Potential applications of shape memory alloys

1.5 References

1.1   Shape memory alloys

Shape memory alloys (SMA) attracted much attention in recent years as intelligent and functional materials due to their unique properties i.e. shape memory effect and superelasticity, which enable them to be widely used in aerospace, micro-electromechanical systems (MEMS) and various bio-medical applications (1-3). The shape memory alloys exhibit two phases i.e. austenite and martensite as shown in **figure 1.1.** Austenite is a high temperature phase named after an English metallurgist William Chandler Austen and martensite is a low temperature phase named after German metallographer Adolf Martens (4). NiTi shape memory alloys, discovered in bulk form in the 1960s, represent a benchmark material for shape memory alloys. While many other binary and ternary shape memory systems exist, NiTi is the most studied and well characterized. One of the first publications on thin film NiTi was in the early 1990s; therefore, research activity on thin film shape memory alloys is a relatively new topic. While shape memory alloys provide unique attributes, the bulk materials bandwidth (1 Hz) limits the material's applicability in many applications. The bandwidth limitation is due to the relatively slow cooling processes related to surface area-to-volume ratios. However, thin film shape memory alloys have very large surface-to-volume ratios, allowing orders of magnitude higher bandwidths to be achieved.

The key characteristic of all shape memory alloys is the occurrence of a martensitic phase transformation, which is a phase change between two solid phases and involves rearrangement of atoms within the crystal lattice. The martensitic transformation is associated with an inelastic deformation of the crystal lattice with no diffusive process involved. The phase transformation results from a cooperative and collective motion of atoms on distances smaller than the lattice parameters. Martensite plates can grow at speeds which approach that of sound in the metal (up to 1100 m/s). Martensitic transformation can occur at low temperatures where atomic mobility may be very small, results in the absence of diffusion in the martensitic transformation within the time scale of transformation. The absence of diffusion makes the martensitic phase transformation almost instantaneous (a first-order transition). When a shape memory alloy undergoes a martensitic phase

Austenite Phase

➤ High temperature Phase
➤ Cubic crystal structure

Martensite Phase

➤ Low temperature phase
➤ Monoclinic crystal structure

Twinned Martensite

Detwinned Martensite
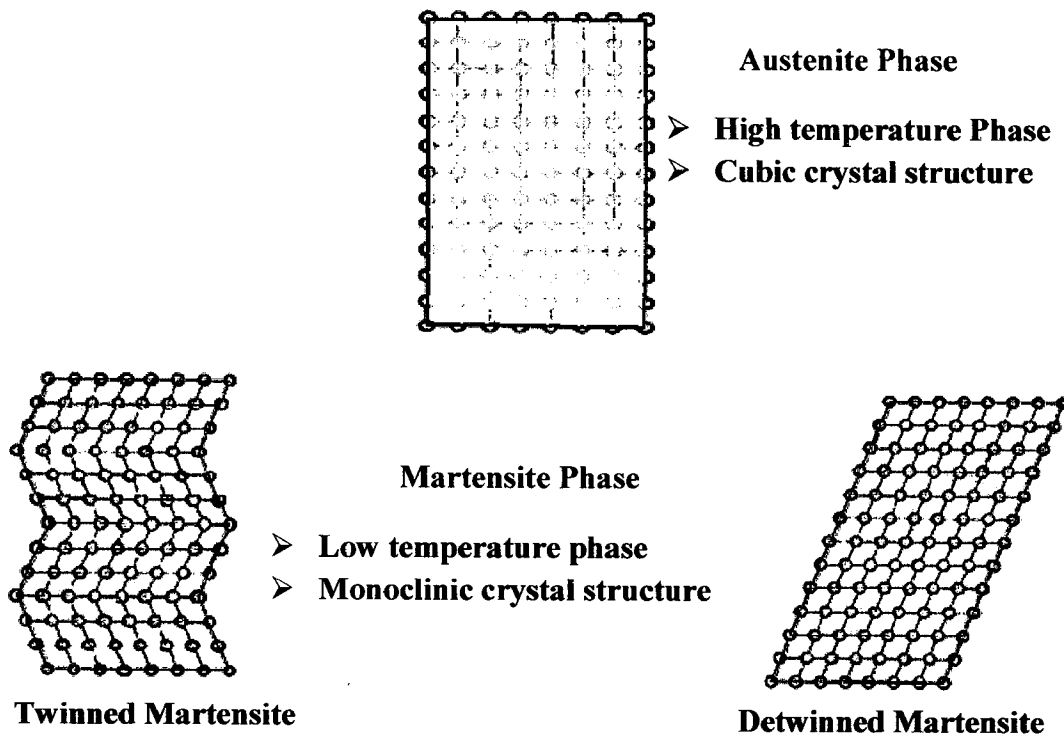
Figure 1.1   Different phases of shape memory alloys.

transformation, it transforms from its high symmetry (usually cubic) austenitic phase to a low symmetry martensitic phase (highly twinned monoclinic structure). The martensitic transformation possesses well defined characteristics that distinguish it among other solid state transformations, which are as follows:

➤   Parent and product phases coexist during the phase transformation, since it is a first order transition, and as a result there exists an invariant plane, which separates the parent and product phases. The lattice vectors of the two phases possess well defined mutual orientation relationships (the Bain correspondences), which depend on the nature of the alloy.

➤   Transformation of a unit cell element produces a volumetric and a shear strain along well-defined planes. The shear strain can be many times higher than the elastic distortion of the unit cell. This transformation is crystallographically reversible.

➤   Since the crystal lattice of the martensitic phase has lower symmetry than that of

4

the parent austenitic phase, several variants of martensite can be formed from the same parent phase crystal.

> Stress and temperature have a large influence on the martensitic transformation. Transformation takes place when the free energy difference between the two phases reaches a critical value.

1.1.1   Shape memory effect

Shape memory effect (SME) is a visually striking phenomenon whereby a material is able to recover its initial shape through subsequent heating after significant deformation in its lower temperature 'martensitic' state (figure 1.2). This phenomenon is related to thermodynamics in the materials. These materials can be subjected to deformations at relatively low temperature and stay deformed until heated, once heated, they have the ability to return to their original non-deformed shape without any significant change to their properties. The basic mechanism in this effect is that material transforms between martensite and austenite phases, referring to a low temperature phase and a high temperature phase, respectively.

Shape memory effect can be explained by schematic stress-temperature phase diagram shown in figure 1.2. The parent austenitic phase (indicated by A) in the
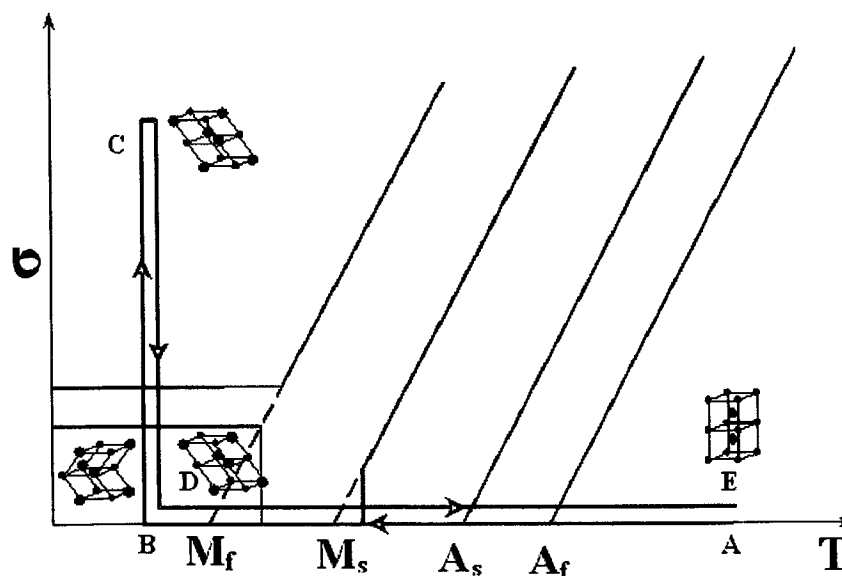
Figure 1.2   Schematic representation of the thermo-mechanical loading path demonstrating the shape memory effect in SMA.

absence of applied stress will transform upon cooling to multiple martensitic variants (up to 24 variants for the cubic-to-monoclinic transformation) in a random orientation and in a twinned configuration (indicated by **B**). As the multivariant martensitic phase is deformed, a detwinning process starts and the growth of certain favorably oriented martensitic variants take place at the expense of other variants. At the end of the deformation (indicated by **C**) and after unloading it is possible that only one martensitic variant remains (indicated by **D**). Upon heating, when temperature reaches A_s (austenite start temperature), the reverse transformation begins to take place, and it is completed at temperature A_f (austenite final temperature). The highly symmetric parent austenitic phase forms only one variant, and thus the original shape is regained (indicated by **E**). Subsequent cooling will result in multiple martensitic variants with no substantial shape change (self-accommodated martensite). Also, moving from **A** to **B** many variants will start nucleating from the parent phase, while in going from **D** to **E** there is only one variant of the parent phase that nucleates from the single remaining martensitic variant indicated by **D**.

1.1.2 Pseudoelasticity

The pseudoelasticity in SMAs is associated with stress-induced transformation, which leads to strain generation during loading and subsequent strain recovery upon unloading at temperatures above austenite final temperature. A pseudoelastic thermomechanical loading path generally starts at a sufficiently high temperature where stable austenite phase exists, then stable detwinned martensite develops under an applied load and finally returns to the austenitic phase on removal of load. Superelastic alloys can be strained several times more than ordinary metal alloys without being plastically deformed, which reflects its rubber-like behavior. However, this phenomenon is observed over a specific temperature range. Beyond this temperature range, alloy is deformed like ordinary materials by slipping. The operating temperature for shape memory devices must not move significantly away from the transformation range, or else the shape memory characteristics may be altered.
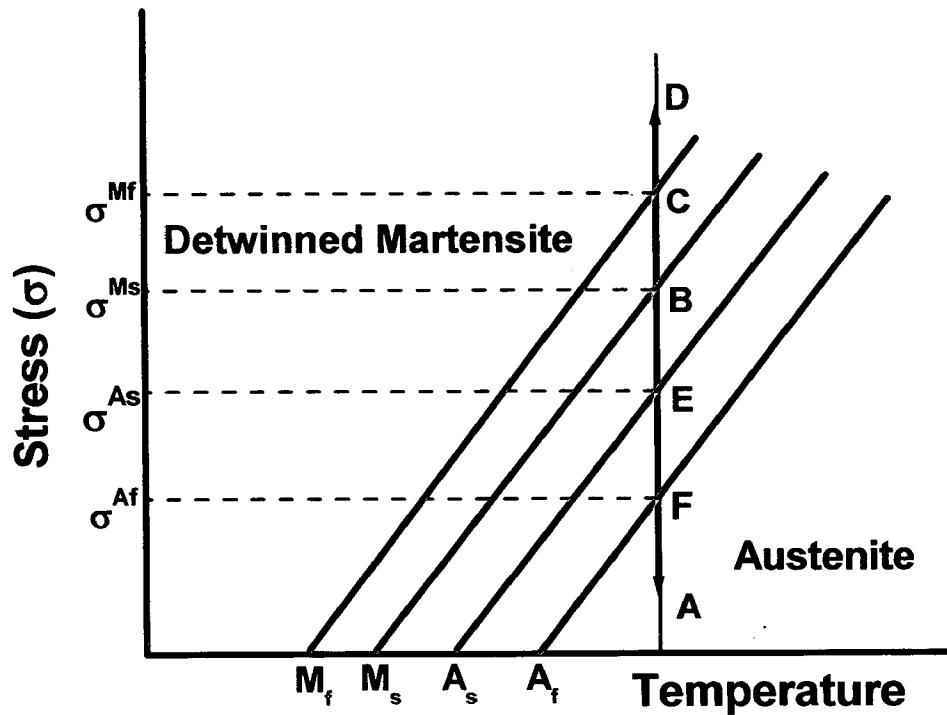
Figure 1.3   Schematic of pseudoelastic loading-unloading paths

Pseudoelastic behavior can be explained by loading and unloading path (A → B → C → D → E → F → A) as shown in **figure 1.3**, which starts at zero stress at a temperature above austenite final temperature (A_f). When a mechanical load is applied, the parent austenite phase undergoes elastic loading (A → B). At a specific load level, the loading path intersects the surface for initiation of martensitic transformation on the phase diagram. This marks the stress level (σ^{Ms}) for the onset of transformation into martensite. The stress induced transformation from austenite to martensite is accompanied by the generation of large inelastic strains. The transformation proceeds (B → C) to the stress level (σ^{Mf}), where the loading path intersects the martensite final (M_f) transformation surface, indicating the end of the transformation. A subsequent increase in the stress causes no further transformation and only the elastic deformation of detwinned martensite occurs (C → D). When the stress is released gradually by unloading, the martensite elastically unloads along the path (D → E). At point E, the unloading path intersects the austenitic start surface (at σ^{As}), which causes the martensite to revert to austenite. The process is accompanied by the recovery of the strain due to phase transformation at the end of unloading.

1.2   NiTi shape memory alloy

The breakthrough for engineering applications occurred with the discovery of NiTi alloy by Buehler and coworkers while investigating materials useful for heat shielding (5, 6). It was observed that in addition to its good mechanical properties as compared to some common engineering metals, equiatomic NiTi also possessed a shape recovery capability. The term "NiTiNOL" was coined for this NiTi material in honor of its discovery at the Naval Ordnance Laboratory (NOL), United States. The discovery of Nitinol developed active research interest into shape memory alloys. The NiTi alloy system has been studied most extensively and is used in the greatest number of commercial applications due to their excellent shape memory performance, good processibility and mechanical properties. During the 1970s, several uses of NiTi in biomedical applications appeared but NiTi stents made their commercial breakthrough in 1990s.The various properties of NiTi shape memory alloy are summarized in **table 1.1**.

Table 1.1   Various properties of NiTi shape memory alloy.

Melting Point	1300°C
Transformation Range	-200 to 110°C
Transformation Hysteresis	30-50°C
Density	6.45 gm/cm^3
Thermal Conductivity	10 W/m-K
Specific Heat	322 J/Kg-K
Latent Heat	24,200 J/Kg
Ultimate Tensile Strength	750-960 MPa
Shape Memory Strain (Max.)	8.5 %
Yield Strength (Austenite)	560 MPa
Young's Modulus (Austenite)	75-83 GPa
Yield Strength (Martensite)	100 MPa
Young Modulus (Martensite)	26-48 GPa

1.2.1   Phase transformation in NiTi shape memory alloy

Phase transformation characteristics in NiTi shape memory alloys are very sensitive to factors like Ni and Ti content, thermo-mechanical treatment, aging and addition of alloy element. In equiatomic NiTi alloy, the shape memory effect occurs in association with the thermoelastic martensitic transformation from the parent phase (austenite phase) with a cubic B2 structure (CsCl type structure, **figure 1.4 (a)**) to the martensite phase with a monoclinic B19' structure **(figure 1.4 (b))**. Sometimes the phase transformation from austenite to martensite and vice versa takes place via self accommodated intermediate phase i.e. rhombohedral or R-phase, which is related to the alloy composition, heat treatment and small grain size. Miyazaki et al. showed that shape memory effect associated with both the R-phase (rhombohedral phase) and martensitic transformations in NiTi thin films **(8)**. Crystal structures of the austenite, martensitic and R phases were determined to be cubic, monoclinic and rhombohedral, respectively, by X-ray diffractometry.

NiTi alloy is inter-metallic compound based on the equiatomic composition. **Figure 1.5** shows the phase diagram of NiTi alloy, which is based on Massalski's diagram **(9)**. Equiatomic NiTi region is known to be very narrow at temperature below 923 K, which is easily distributed by other precipitates of second inter-metallic phases like Ti-rich phases (Ti$_2$Ni) or Ni-rich phases (Ni$_3$Ti). The triangular region designated "TiNi" near the equiatomic composition exhibit bcc structure at

<div align="center">(a)   (b)</div>
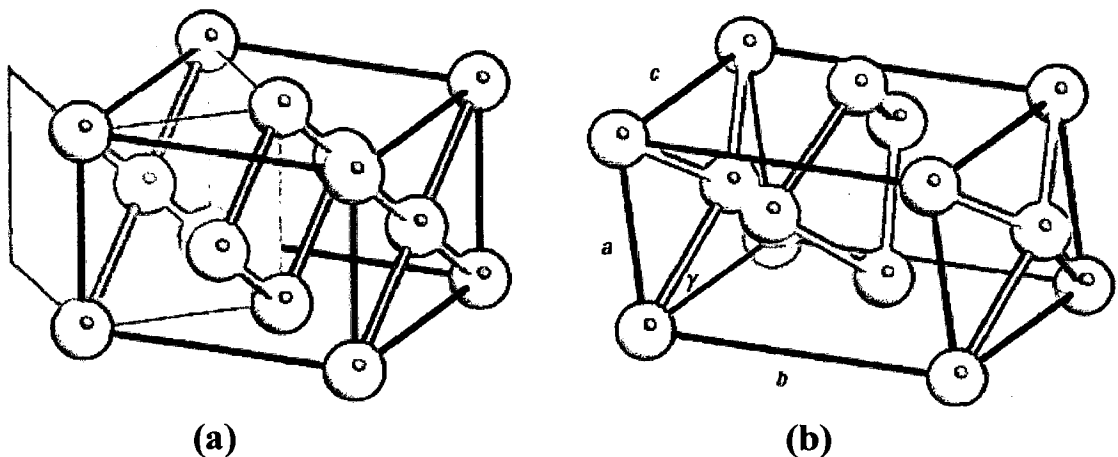
Figure 1.4   (a) The cubic B2 cell (shaded box) and (b) B19' structure of NiTi (7).
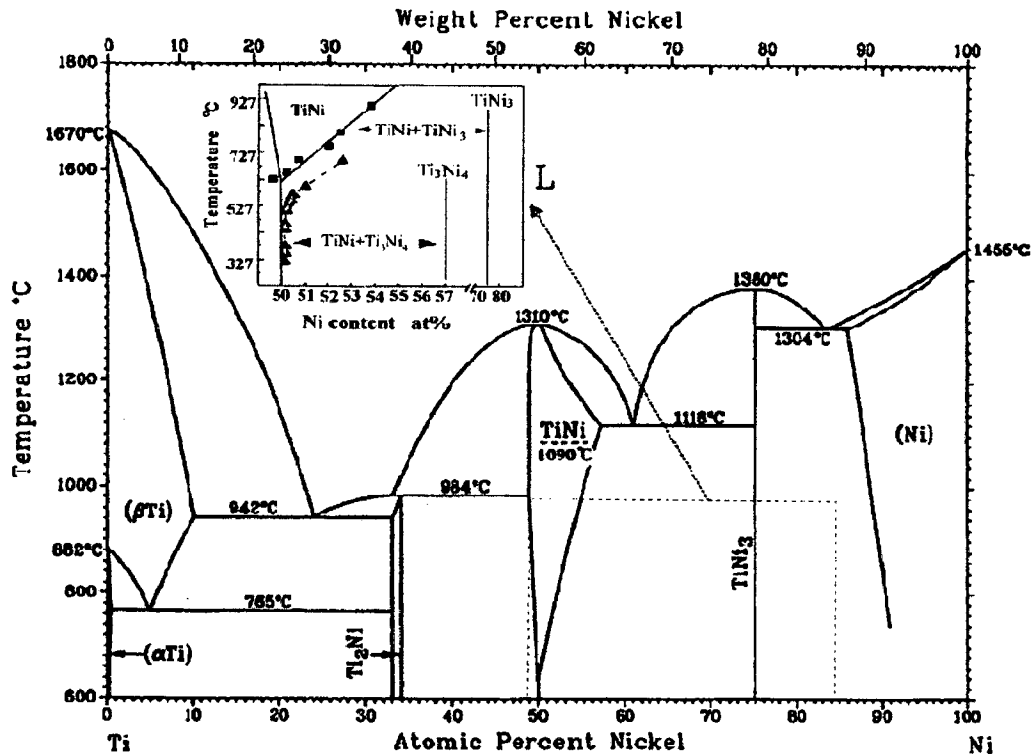
Figure 1.5   Phase diagram of NiTi shape memory alloy.

temperatures above 1090 °C (dotted line) and B2 (cubic) ordered structure below that temperature. If the alloy is quenched from the B2 region, a martensitic transformation occurs from B2 to B19' phase below the respective martensite start temperature. The solubility in NiTi changes with temperature on the Ni-rich side. This means that precipitation hardening may be used on the Ni-rich side. On this side, the stable precipitate phase i.e. Ni_3Ti and other metastable phases like Ti_3Ni_4 and Ti_2Ni_3 exist **(10-12)**. Ti_3Ni_4 phase appears at shorter aging times and at lower aging temperatures **(13)**. This Ti_3Ni_4 phase is especially important for improving shape-memory characteristics and strength, since it precipitates on a very fine scale.

1.3   Shape memory alloy thin films

At the end of 1980's, SMA thin films received more attention as new functional materials. This new research area is motivated by the progress of micro-electro-mechanical systems (MEMS) made at the same era. The shape memory materials have been considered to be a very attractive material for microactuators because it

posses great advantages such as relatively large deformation and recovery force over other kinds of performance materials.

1.3.1 NiTi shape memory alloy thin films

More recently, NiTi shape memory alloy thin films are recognized as potential candidate for microfabrication and integration in micro-miniature systems composed of mechanical elements, actuators, sensors and electronics made on single chip **(14-16)**. Higher power density, large displacement, actuation force, low voltage requirements and compatibility with batch processing technologies of silicon micromachining make these films a better option for micro-electro-mechanical systems (MEMS) and Bio-MEMS such as micropumps, microgrippers, microvalves and micropositioner etc **(16-19)**. Thin films exhibit small thermal mass to heat or cool as compared to NiTi bulk, which results reduction in response time and increased operation speed. Higher surface to volume ratio of thin films result in faster natural air cooling that enhanced the operating frequency range. Also, the large actuation stresses and strains of NiTi SMA can be retained in the thin film.

Many techniques have been employed to fabricate NiTi thin films like laser ablation, ion beam deposition, arc plasma ion plating, plasma spray and flash evaporation but these techniques have some intrinsic problems, such as non-uniformity in film thickness and composition, low deposition rate, or non-batch processing, incompatibility with MEMS process, etc. In comparison to above mentioned techniques, magnetron sputtering showed the way to deposit the films with good adhesion, high hardness, reproducibility and flexibility and it also enables the fabrication of large scale uniform coatings with a low/high density. In addition, magnetron sputtering is of particular advance to deposit multi-component films as binary, ternary. Busch et al. first fabricated NiTi thin film using sputter deposition technique in 1990 **(20)**. As the phase transformation in SMA thin film is accompanied by significant changes in the mechanical, physical, chemical, electrical and optical properties, such as yield stress, elastic modulus, hardness, shape recovery, electrical resistivity, thermal conductivity, thermal expansion coefficient, surface roughness, etc. These changes can be fully made use of the design and fabrication of microsensors and micro-actuators. However, there are still some

important issues remain unresolved like optimization of deposition parameters in order to get good quality films, effect of nano grain or nanocrystalline structure on shape memory behavior, film thickness effect (since a minimum thickness is required for the optimized shape memory effect), surface chemistry, surface adsorption and biocompatibility of NiTi films with small grain size. Therefore, full understanding of these issues will make these films more promising for application in MEMS technology.

1.3.2   TiN/NiTi heterostructures

Good wear resistance of a material is an important property required for some MEMS and biomedical applications. Austenite phase of NiTi alloy exhibits good wear resistance (21), while martensite phase exhibit poor wear resistance and high coefficient of friction. In the case of SMA films, interfacial adhesion, large coefficient of friction and potential stress are other major concerns for their tribological application (22, 23). Also, the releasing of nickel in to the environment is a major problem for their wide use in biomedical applications. Some surface modification methods, such as irradiation of NiTi films by electrons, ions (Ar, N, He, Ni or O ions), laser beams, neutrals were used (i) to modify the surface, physical, mechanical, wear, corrosion and biological properties for application in hostile and wear environment; (ii) to cause lattice damage and/or alter the phase transformation behaviors along thickness of film, forming novel two- way shape memory actuation (24-26). The problems of these surface treatments are high cost, possible surface or ion induced damage, amorphous phase formation, or degradation of shape memory effects (24). Surface oxidation of NiTi bulk materials have often been reported to prevent the Ni ion release and improve its biocompatibility (27, 28). However, this oxidation layer is too thin, fragile and easy to be removed (29). Therefore, there is a need to search for stable, corrosion resistant and biocompatible protective coating for biomedical and MEMS applications of NiTi based SMA thin films. Alumina (30) and TiN coatings are promising materials of choice for value added applications in the biomedical implant and surgical industries. In the present study, alumina coatings are not chosen in order to prevent the oxidation of NiTi that can degrade the shape memory behavior.

TiN is a well known material for its superior mechanical properties, excellent corrosion, wear resistance and good biocompatibility. It exhibits rocksalt structure (FCC bravais lattice) or NaCl-type crystal structure with a roughly 1:1 stoichiometry; however TiN_x compounds with x ranging from 0.6 to 1.2 are thermodynamically stable. The lattice parameter of TiN is equal to 4.24 Å. It oxidizes at 600°C in normal atmosphere but more resistant in an inert atmosphere and has a melting point of 2930 °C. TiN coatings are being used in a wide range of applications such as wear resistant coatings to protect cutting tools, dies, tools, sliding surfaces of bearings and gears from aggressive environments due to its good wear resistance and inertness to steels. They are also used in microelectronics devices, solar cells, decorative purposes on tableware, clocks etc. or as a non-toxic exterior for human implants (31-34). TiN shows intrinsic biocompatibility and hemocompatibility and therefore used as surface layers and electrical interconnects in orthopaedic prostheses, cardiac valves and other biomedical devices (35, 36). Also, the adhesion of TiN film to the substrate is very good as it forms a metallurgical bond to the substrate that will not flake, blister, chip or peel. Therefore, in the present study, titanium nitride (TiN) was chosen to deposit over NiTi as a passivation layer to prevent surface layer degradation and nickel releasing into the environment.

1.4   Potential applications of shape memory alloys

Practical applications of SMAs appeared within 10 years or so after the discovery of shape-memory effect in NiTi alloys. The first successful application was made by Raychem Corp. for fasteners and tube couplings. In this application, a coupling made of NiTi is expanded in diameter in martensitic state, then the tubes are inserted in the coupling and heated above the austenite final temperature. The coupling shrinks, owing to the shape memory effect, and the joint is thus secured. NiTi couplings were used for the hydraulic systems of F-14 jet fighters. The application of SMAs to heat engines became very popular. However, the application was not successful, since its theoretical (Carnot) efficiency was only 4–5%. Various thermal actuators then came into existence as a part of electric appliances and automobile engineering: flaps in air conditioners, which change the direction of airflow depending upon the temperature

of the air; coffee makers; rice cookers; drain systems for steam heaters in trains; outer vent control systems to avoid fuel evaporation in automobiles and devices to open parallel hydraulic channels in automatic transmissions. Among these, the application of SMAs to air-conditioner flaps was the most successful, replacing the ordinary sensor/integrated-circuit/relay/motor system with a simple combination of a NiTi spring and a bias spring. Also, SMA can be used in the aerospace industry, especially those related to vibration control of slender structures and solar panels, and non explosive release devices. Micromanipulators and robotic actuators have been employed in order to mimic the smooth movement of human muscles. SMAs are commonly used as external actuators or as SMA fibers embedded in a composite matrix so that they can alter the mechanical properties of slender structures for the control of buckling and vibration.

Biomedical applications of SMA have been extremely successful because of the functional properties of these alloys, increasing both the possibility and the performance of invasive surgeries. The biocompatibility of these alloys is one of the important point related to their biomedical applications as orthopaedic implants, cardiovascular devices and surgical instruments as well as orthodontic devices.

NiTi thin film is considered as a core technology for actuation of some MEMS devices, where large force and stroke are essential. NiTi films can provide large forces for actuation and large displacement, therefore, most applications of these films in MEMS are focused on micro-actuators such as:

Micropumps and microvalves
MEMS based micropumps and micrpvalves are attractive for many applications such as implantable drug delivery, chemical analysis and analytical instruments, etc. NiTi thin films are suitable for building microvalves and pumps. There are different designs for NiTi film based micropumps or microvalves, and most of them use NiTi membrane for actuation.

Microgrippers
Grasping and manipulating small or micro-objects with high accuracy is required for a wide range of important applications, such as the assembly in microsystems,

endoscopes for microsurgery, and drug injection micromanipulators for cells. There are some basic requirements for microgrippers like, large gripping force, sufficient opening distance for assembling works, etc. NiTi films are promising in these applications. The popular design of microgrippers is out-of-plane bending mode, mostly with two integrated NiTi/Si cantilever (or other substrate, such SU-8 or polyimide, etc.) with opposite actuation directions.

Microsensors, microswitches and microrelays

NiTi thin films are sensitive to environmental changes, hence ideal candidate for microsensor applications. NiTi film was reported as a gate of metal-on-silicon (MOS) capacity sensor, for detecting the increase in capacitance of NiTi films during heating and cooling. Other potential applications as switches or microrelays include on-chip circuit breakers against overheating caused by short circuit or overload, probe tips for automatic test equipment, fiber optics switching, automotive fuel injectors, micro-lens positioner, etc. The reflection coefficient of the austenite phase is higher than that of the martensite phase by more than 45%, thus it is possible to use these films as a light valve or on-off optical switch for spatial light modulators.

1.5   References

(1) Otsuka K. and Ren X., "Recent development in research of shape memory alloys", Intermetallics, 7, 511-528 (1999).

(2) Otsuks K. and Wayman C. M., "Shape Memory Materials", Cambridge university press (1998).

(3) Yin L. and Anantasuresh G. K., "A novel topology design scheme for the multi-physics problems of electro-thermally actuated complaints micromechanisms", Sensors and actuators A, 97-98, 599-609 (2002).

(4) Srinivasan A. V. and McFarland M. D., "Smart structures analysis and design", Cambridge university press, p. 26-69 (2001).

(5) Buehler W. J., Gilfrich J. V. and Wiley R. C., "Effects of low-temperature phase changes on the mechanical properties of alloys near composition TiNi", Journal of Applied Physics, 34, 1475-1481 (1963).

(6) Buehler W. J. and Wiley R. C., "Nickel-base alloys", U.S. Patent 3, 174, 851 (1965).

(7) Huang X., Ackland G. J. and Rabe K. M., "Crystal structures and shape–memory behaviour of NiTi", Nature Materials, 2, 307-311 (2003)

(8) Miyazaki S., Ishida A. and Takei A., "Proceedings of the International Symposium on Measurement and Control in Robotics (ISMCR-92)", Tsukuba 495 (1992).

(9) Massalski T. B., Okamoto H., Subramanian P. R. and Kacprzak L., "Binary Alloy Phase Diagrams", , ASM International, Materials Park, OH, Volume 3, 2nd edition, p. 2874 (1990).

(10) Tadaki T., Nakata Y., Shimizu K., and Otsuka K., "Crystal structure, composition and morphology of a precipitate in an aged Ti-51 at. %Ni shape memory alloy", Transactions of the Japan Institute of Metals, 27, 731-740 (1986).

(11) Saburi T., Nenno S., and Fukuda T., "Crystal structure and morphology of the metastable phase in shape memory Ti-Ni alloys", Journal of the Less- Common Metals, 125, 157-166 (1986).

(12) Hara T., Ohba T., Otsuka K. and Nishida M., "Phase transformation and crystal structures of Ti_2Ni_3 precipitates in Ti-Ni alloys", Materials Transactions JIM, **38**, 277-284 (1997).

(13) Nishida M., Wayman C. M. and Honma T., "Precipitation Processes in Near-Equiatomic TiNi Shape Memory Alloys", Metallurgical and Materials Transaction A, **17A**, 1505-1515 (1986).

(14) Wolf R. H. and Heuer A. H., "TiNi (shape memory) films on silicon for MEMS applications", Journal of Microelectromechanical Systems, **4**, 206-212 (1995).

(15) Kahn H., Huff M. A. and Heuer A. H., "The TiNi shape memory alloy and its applications for MEMS", Journal of Micromechanics and Microengineering, **8** (3), 213-221 (1998).

(16) Krulevitch P., Lee A. P., Ramsey P. B., Trevino J. C., Hamilton J. and Northrup M. A., "Thin film shape memory alloy microactuators", Journal of Microelectromechanical Systems, **5**, 270-282 (1996).

(17) Gill J. J., Chang D. T., Momoda L. A. and Carman G. P., "Manufacturing issues of thin film NiTi microwrapper", Sensors and Actuators, A: Physical, **93**, 148-156 (2001).

(18) Humbeeck J. V., "Shape memory alloys: A material and a technology", Advanced Engineering Materials, **3**, 837-850 (2001).

(19) Fu Y., Du H., Huang W., Zhang S. and Hu M., "TiNi-based thin films in MEMS applications: A review", Sensors and Actuators, A: Physical, **112**, 395-408 (2004).

(20) Busch J. D. and Johnson A. D., "Shape-memory alloy micro-actuator", US Patent No. 5061914, (1991).

(21) Li D. Y., "A new type of wear-resistant material: pseudo-elastic TiNi alloy", Wear, **221**, 116-123 (1998).

(22) Girardeau T., Bouslykhane K., Mimault J., Villain J. P. and Chartier P., "Wear improvement and local structure in nickel–titanium coatings produced by reactive ion sputtering", Thin Solid Films, **283**, 67-74 (1996).

(23) He J. L., Won K. W., Chang C. T., Chen K. C. and Lin H. C., "Cavitation resistant of TiNi films deposited by using cathodic are plasma ion plating", Wear, **233-235**, 104-110 (1999).

(24) Goldberg F. and Knystautas E. J., "The effects of ion irradiation on NiTi shape-memory alloy thin films", Thin Solid Films, **342**, 67-73 (1999).

(25) Grummon D. S. and Gotthardt R., "Latent strain in titanium–nickel thin films modified by irradiation of the plastically-deformed martensite phase with 5MeV Ni^{2+}", Acta Materialia, **48**, 635–646 (2000).

(26) Lagrange T. B. and Gotthard R., "Microstructrual evolution and thermo-mechanical response of Ni ion irradiated TiNi SMA thin films", Journal of Optoelectronics and Advanced Materials, **5**, 313-318 (2003).

(27) Firstov G. S., Vitchev R. G., Kumar H., Blanpain B. and Humbeeck J. V., "Surface oxidation of NiTi shape-memory alloy", Biomaterials, **23**, 4863-4871 (2002).

(28) Tan L. and Crone W. C., "Surface characterization of NiTi modified by plasma source ion implantation", Acta Materialia, **50**, 4449-4460 (2002).

(29) Wu S. K., Chu C. L. and Lin H. C., "Ion nitriding of TiNi shape memory alloys I. Nitriding parameters and microstructure characterization", Surface and Coating Technology, **92**, 197-205 (1997).

(30) Cloud A. N., Kumar S., Kavdia M., Abu-Safe H. H. and Gordon M. H., "Protein adsorption on low temperature alpha alumina films for surgical instruments", Surface and Coatings Technology, **203**, 913–917 (2008).

(31) Tao M., Udeshi D., Agarwal S., Maldonado E. and Kirk W.P., "Negative schottky barrier between titanium and n-type Si (001) for low resistance ohmic contacts", Solid State Electronics, **48**, 335-338 (2004).

(32) Vaz F., Cerqueira P., Rebouta L., Nascimento S. M. C., Alves E., Goudeau P., Riviere J. P., Pischow K. and Rijk J. D., "Structural, optical and mechanical properties of coloured TiN_xO_y thin films", Thin Solid Films, **447-448**, 449-454 (2004).

(33) Srivastav S., Jain A. and Kanjilal D., "Improvement of adhesion of TiN coatings on stainless steel substrates by high energy heavy ion irradiation", Nuclear Instruments and Methods in Physics Research B, **101**, 400-405 (1995).

(34) Jeyachandran Y. L., Narayandass S. K., Mangalaraj D., Areva S. and Mielczarski J. A., "Properties of titanium nitride films prepared by direct current magnetron sputtering", Materials Science and Engineering A, **445-446**, 223-236 (2007).

(35) Chung K. H., Liu G. T., Duh J. G. and Wang J. H., "Biocompatibility of a titanium-aluminum nitride film coating on a dental alloy", Surface and Coatings Technology, **188-189**, 745-749 (2004).

(36) Franks W., Schenker I., Schmutz P., and Hierlemann A., "Impedance characterization and modeling of electrodes for biomedical applications", IEEE Transactions on Biomedical Engineering, **52**, 1295-1302 (2005).

Chapter 2

Synthesis and Characterization Techniques

CHAPTER 2

SYNTHESIS AND CHARACTERIZATION TECHNIQUES

2.1 Fabrication of shape memory alloy thin films

2.2 Magnetron sputtering

    2.2.1   Background

    2.2.2   Basic principle of magnetron sputtering

    2.2.3   Experimental setup and procedure

2.3 Basic structural characterization techniques

    2.3.1   X-ray diffraction

    2.3.2   Specimen beam interaction

    2.3.3   Field emission scanning electron microscopy

    2.3.4   Transmission electron microscopy

    2.3.5   Atomic force microscopy

2.4 Measurement of electrical, mechanical and electrochemical properties

    2.4.1   Electrical transport measurement

    2.4.2   Nanoindentation

    2.4.3   Voltammetry

2.5 References

2.1   Fabrication of shape memory alloy thin films

A wide variety of techniques have been used to synthesis SMA thin films including thermal evaporation, pulse laser deposition, rapid solidification, etc., only magnetron sputtering is widely used so far. The reasons for using magnetron sputtering deposition method are as follows:

> ➢ Control of film composition and thickness
> ➢ Large area uniformity
> ➢ Deposition of films with properties close to bulk material
> ➢ Good adhesion to substrate
> ➢ High deposition rate
> ➢ Compatibility with MEMS processing

Although, there are some intrinsic problems associated with sputtering of NiTi films including the difference in sputtering yield of nickel and titanium at a given sputtering power density, geometrical composition non-uniformity over substrate and along cross-section thickness of the coating, as well as wear, erosion and roughening of targets during sputtering **(1, 2)**. To combat these problems, following precaution have been taken: (a) separate element target of Ni and Ti were used **(1, 3)**; (b) substrate was kept on axial rotation during deposition; (c) good configuration of target and substrate position and (d) precise control of sputtering conditions etc. Contamination is also one of the major problem, therefore, it is important to limit the impurities (like oxygen and carbon) to prevent the brittleness, degradation of mechanical properties and shape memory effect. For this reason, the purity of Ar gas and targets is essential, and the base vacuum of the main chamber should be as high as possible. Pre-sputtering of targets before deposition effectively removes the surface oxides layer, thus constitutes one of the important steps in ensuring film purity.

2.2   Magnetron sputtering

2.2.1   Background

In a sputtering process, plasma is generated when secondary electrons, produced by the collision of positive ions with the target atoms, collide and ionize the inert gas

atoms. The initial positive ions needed to trigger the generation of secondary electrons are thought to be either the stray ions always present in the atmosphere or the ions produced by field ionization of the inert gas atoms. When an inert gas cation hits a target atom, the latter gains part of the momentum and transfer it to other atoms through further collisions, leading to a cascade which result in some of the target atoms to 'sputter' out of the target. The rate of atoms ejected from the target depends on the number of bombarding ions. It is therefore desired to increase the plasma density in front of the sputtering source. Basic sputtering, without any plasma confinement, has the disadvantages of low deposition rates and low ionization efficiencies of the plasma. These limitations have lead to the development of magnetron sputtering. The magnetron was first introduced in the early 70s (4, 5) and it has become the best choice for the deposition of a wide range of industrial coatings. The driving force behind the development of magnetron sputtering were the increasing demand of high quality functional thin films in widespread application areas including hard, wear-resistant coatings, decorative coatings, and coatings with specific optical, electrical or mechanical characteristics.

2.2.2   Basic principle of magnetron sputtering

Magnetron sputtering makes use of the fact that a magnetic field configured parallel to the target surface can constrain the motion of secondary electrons ejected by the bombarding ions to a close vicinity of the target surface. An array of permanent magnets is placed behind the sputtering source. The magnets are placed in such a way that one pole is positioned at the central axis of the target, and the second pole is placed in a ring around the outer edge of the target as shown in **figure 2.1(a)**. A plate of a highly permeable material (such as iron) located behind the magnets, which prevent the magnetic flux from spreading in to regions other than in front of the target surface.

This configuration creates crossed electric (E) and magnetic (B) fields, where electrons drift perpendicular to both E and B. Due to radial magnetic field, the secondary electrons get confined in an annular region close to the target surface with a boundary corresponding to the location of the magnetic poles, where electric (E)
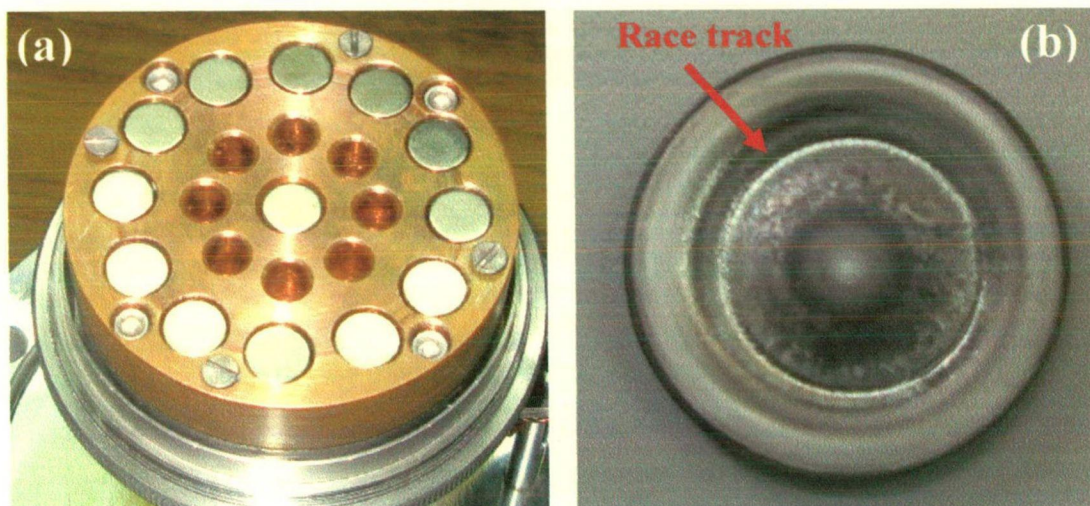
Figure 2.1   **(a)** Arrangement of magnets in magnetron sputtering gun and **(b)** Race track created in target after sputtering.

and magnetic (B) fields become parallel. The impression of the sputter eroded target, also called race track, is shown in **figure 2.1 (b)**. The confinement of secondary electrons leads to an increase in the probability of ionizing the inert gas atoms, making the plasma more intense and sustainable at lower pressures and voltages as compared to basic sputtering. The sputtered atoms get deposited on all the surfaces, with maximum deposition taking place on the substrate, which is the nearest surface to the target and subtends the maximum area perpendicular to the momentum of ejected target atoms and clusters. Ions are also subjected to the same electromagnetic field, but due to their heavy mass, the larmor radius often exceeds the dimensions of the plasma.

2.2.3   Experimental setup and procedure

Figure 2.2 (a) shows the turbo based magnetron sputtering system assembled in our laboratory (Functional Nanomaterials Research Laboratory, Department of Physics). Sputtering system was specially designed and developed for co-sputtering and shown in **figure 2.2 (b)**. The marked positions i.e. 1, 2 and 3 exhibit the positions for the mounting of sputtering guns. All the sputtering guns were positioned in such a way so that the plasma from all the guns can be concentric to get good quality films. The pumps and gauges fitted in to the chamber are from Pfeiffer Vacuum. For DC

Figure 2.2   **(a)** Magnetron sputtering system, **(b)** Back view of sputtering system exhibit position of sputtering guns and **(c)** Substrate heater (Range: RT-850 °C).

sputtering, Aplab high voltage DC power supply (50-1000 V, 0-1 A) was used. Circular discs of diameter 2 inch and thickness 3-5 mm of pure material were used as target material, which were mounted on the magnetron guns for sputtering. The substrate was fixed on a substrate heater (Range: Room temperature - 850 °C,

Figure 2.2 (c)) with the help of clips and silver paste for the fabrication of thin films. The temperature of the substrate was controlled via the temperature controller linked with the substrate heater. After mounting the substrates, the chamber was evacuated using a turbo molecular pump, backed by rotary pump up to high vacuum ($>2 \times 10^{-6}$ Torr). After evacuation, an inert gas like Argon (99.999% purity) was fed into the chamber via gas inlet valve. Simultaneously, the gate valve was brought into almost closed state (throttling) to match the gas influx and pumping-out rate. With proper throttling, the inert gas pressure and flow rate inside the chamber can be made very stable. Then the negative potential was applied to the target and the sputtering process starts.

2.3 Basic structural characterization techniques

2.3.1 X-ray diffraction

X-ray diffraction is the non-destructive and most powerful technique for determining the crystal structure, preferred orientation, crystallite size, lattice constants, crystal defects, stress, layer thickness, phase analysis, etc. of solid matter. When a monochromatic beam of x-rays is incident upon a regular crystalline material then the beam will be scattered from the material at definite angles. This is produced by an interference effect called diffraction between the x-rays from different atomic layers within the crystal. These atomic layers are separated by distance in the order of angstroms and are comparable to the wavelength of x-rays. If the x-rays of a known frequency interacts with a crystalline solid then under particular circumstances of layer separation and angle of incidence to layer, the scattering from the different layers will constructively interfere at some angles and destructively interfere at most of the angles. This effect is characterized by the Bragg's equation ($2d \sin\theta = n\lambda$, λ = wavelength of incident radiation and d = interplanar distance between the lattice planes), which is the base of x-ray crystallography.

In the present study, Bruker D8 Advance x-ray diffractometer (**Figure 2.3**) was used to study the crystallinity, crystallite size and strain of the grown thin films. The radiation (Cu Kα) emanating from the X-ray tube is diffracted at the specimen

and recorded by a detector. Bruker D8 Advance diffractometer uses NaI scintillation counter as a detector. It can detect the diffracted radiations in the wavelength ranging from 0.5 to 3 Å. Monochromators are used to suppress the undesired portions of radiation. To restrict the irradiated specimen area, aperture diaphragm is arranged between the tube and the specimen as shown in **figure 2.3**. The second aperture diaphragm shields the strong scattered radiation of the first aperture diaphragm. The scattered radiation diaphragm is used to suppress undesired scattered radiation. The resolution depends upon the detector diaphragm.

The crystallographic information is obtained by evaluating 'd' values and indexing of reflections. The characteristics diffraction pattern of a given substance can always be obtained whether the substance is present in pure state or as one constituent in a mixture of several substances. X-ray diffraction pattern is characterized by a set of line positions (2θ) and a set of relative intensities (I). The angular position of lines depends on the wavelength of the incident ray and spacing 'd' of the lattice planes.

The technique can be used for quantitative analysis in which the concentration of phases are calculated by determining the area of the peak, since the intensity of diffraction lines due to one constituent of a sample depend upon the concentration of that constituent in the specimen. The qualitative analysis for a
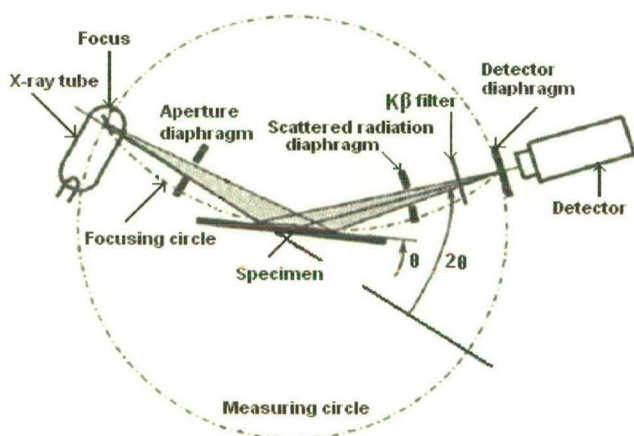
Figure 2.3 Schematic diagram of beam path.   Photograph of Bruker D8
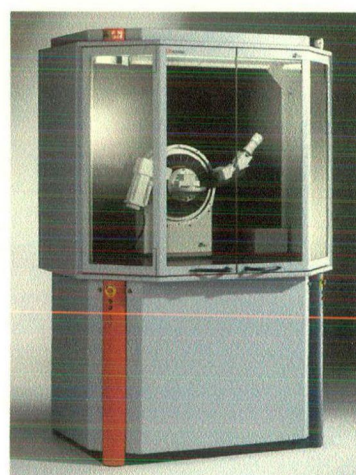
Advance X-ray Diffractometer

particular substance is accomplished by identification of the pattern of that .
substance. The crystallite size is an important parameter, which can be determined
using Scherrer's formula (6):

$$l = \frac{0.9\,\lambda}{B \cos \theta_b}$$ (2.1)

where l is the length of the crystal in the direction perpendicular to the reflecting
planes, B is the full width at half maximum (FWHM) of the Bragg reflection in the
radians on the 2θ scale and θ_b is the Bragg reflection angle. To make sure of
absolute values of the 2θ diffraction angles, the diffractometer was calibrated with
respect to the peak position of an Si calibration standard. A polycrystalline powder
was used for instrumental correction. It is important to subtract the background and
instrumental line width from the observed line width to get a correct estimate of
broadening due to small particle size.

2.3.2   Specimen beam interaction

When an incident electron beam strikes the specimen composed of a crystalline and
amorphous structure, it undergoes a series of complex interactions with the nuclei
and electrons of the atoms of the sample (figure 2.4). The interactions produce a
variety of secondary products, such as:

Secondary electrons: When the specimen is struck by the primary beam, electrons
are freed from the specimen. The electrons released from the surface are mostly low
energy secondary electrons between 0 and 50 electron volts. They will mainly give
information of morphology and topology of the specimen.

Backscattered electrons: When the specimen is struck by the primary beam,
electrons are elastically and non-elastically scattered back. Elastically means the
primary electrons did not lose any of their primary energy. Back-scattered electrons
release information on the composition of a material, the so-called Z contrast or
atomic number contrast.

Photons: Photons or light quanta are freed when the primary beam strikes a material
like some minerals. These light quanta can be detected using a cathode luminescence
detector. The light detected can vary from infrared to ultraviolet.
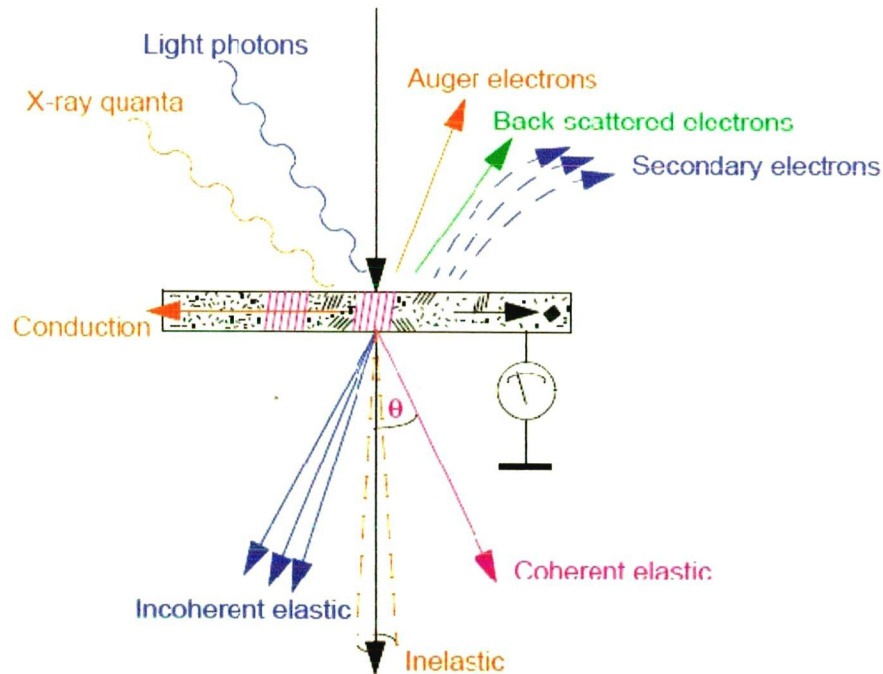
Figure 2.4   Specimen beam interaction.

Auger electrons: Due to collisions with the primary beam, auger electrons are freed. These electrons are element specific and their energy can be detected using an auger mass spectrometer. This technique is applied for detection of light elements and gives information on the top atomic layers of the specimen.

X-ray quanta: X-ray radiation takes place when an electron has received extra energy, e.g. due to a collision with an electron of the primary beam. As this is an unstable situation, the electron will fall back into its original orbit, the extra energy is released in the form of an X-ray quantum.

Conduction: Electrons that are stopped in the specimen must leave the specimen, therefore all specimens that are not conductive are made conductive by an extra layer of gold or carbon. If the specimen was non-conductive it would start to become charged and thus an unwanted electrostatic lens would be made, which increases the inherent astigmatism.

Heat: The energy of the electrons stopped in the specimen is transferred to kinetic energy. The local temperature of the specimen can rise to temperature higher than 100 $^{\circ}$C. The temperature depends on the acceleration voltage, the number of electrons (emission) and size (spot size) of the primary beam. If the temperature is

30

too high for the type of specimen under investigation, the specimen will be damaged either in the form of contamination, evaporation, or complete tearing of the film layer.

Elastic scattering: Elastic scattering takes place when the negative charged electrons are scattered due to interaction with the positively charged atomic nucleus. Because the mass of the nucleus is much higher than the mass of the electrons, therefore a negligible energy transfer takes place. This means that the speed and thus the associated wavelength of the electron do not change. There are two types of elastic scattering:

(a) **Incoherent elastic scattering:** This is the case when the specimen has an amorphous structure. The deflected electron waves have no phase relation to the specimen.

(b) **Coherent elastic scattering:** This is the case when the specimen has a crystalline structure. There is now a phase relation between the specimen and waves are deflected under defined angles.

Inelastic scattering: Inelastic scattering takes place when the negative charged electrons are scattered due to interaction with the negative charged electrons. Now energy transfer takes place, this means that the speed and thus the associated wavelength of the electron changes.

2.3.3 Field emission scanning electron microscopy

The scanning electron microscope (SEM) has a large depth of field, which allows a large amount of the sample to be in focus at one time. The SEM also produces images of high resolution, which means that closely spaced features can be examined at a high magnification.

In the present study, field emission scanning electron microscope (FEI Quanta 200F model) with resolution of 2 nm and magnification 500000X was used to study the surface morphology of these thin films. **Figure 2.5** shows a schematic diagram of the field emission scanning electron microscope (FESEM). FESEM uses field emission electron gun, which provides improved resolution of 2 nm i.e. 3 to 6 times better than conventional SEM and minimized sample charging and damage. In conventional SEM, electrons are thermionically emitted from a tungsten or
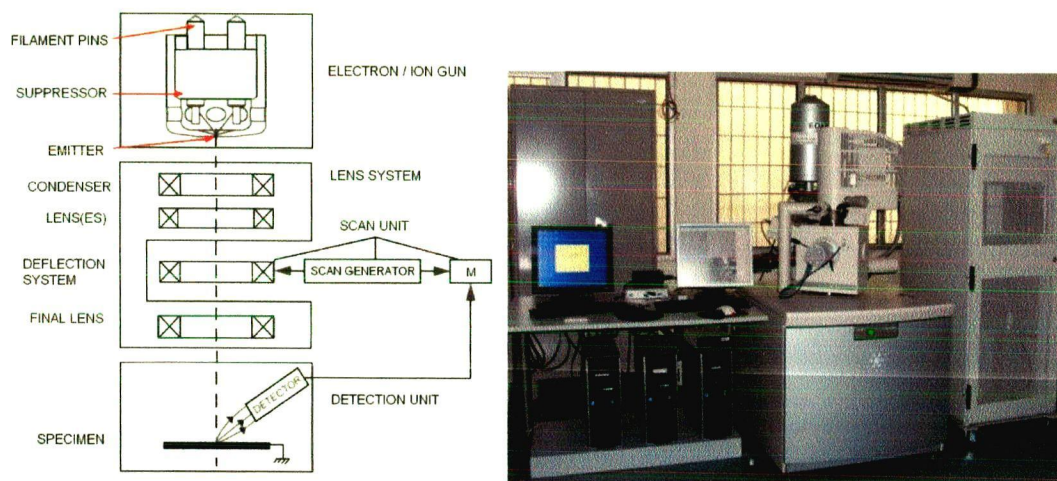
Figure 2.5 Schematic diagram of   Photograph of FESEM

                     FESEM   (FEI Quanta 200F)

lanthanum hexaboride (LaB_6) cathode and are accelerated towards an anode, alternatively electrons can be emitted via field emission (FE). Tungsten is used as a filament because it has the highest melting point and lower work function, thereby allowing it to be heated for electron emission. The basic mechanism of field emission is that a high voltage applied between a pointed cathode and a plate anode caused a current to flow. The field emission tip is generally made of a single crystal tungsten wire sharpened by electrolytic etching. A tip diameter of 100 to 1000 Å is used. The field emission process itself depends on the work function of the metal, which can be affected by adsorbed gases.

     The electron beam, which typically has an energy ranging from a few hundred eV to 50 keV, is focused by two condenser lenses into a beam with a very fine focal spot size. The first condenser lens that works in conjunction with the condenser aperture helps to narrow the beam and also limit its current. The second condenser lens then forms the electrons into a very thin, coherent beam. The high-energy beam of electrons scans the sample surface in a raster pattern using a set of scanning coils to obtain image. The objective lens does the final focusing of the beam onto the sample. At each point the numbers of secondary and back-scattered electrons reaching the detector are counted to be used for determining the relative intensity of the pixel representing that point in the final image.

Using the energy dispersive x-ray analysis (EDAX) attachment with the FE-SEM, elemental composition analysis was done. An EDAX spectrum normally displays peaks corresponding to the energy levels for which the most X-rays had been received. Each of these peaks is unique to an atom, and therefore corresponds to a single element. Higher the peak intensity, higher is the element concentration in the specimen.

Insulator samples would be difficult to image using an SEM because of the fact that they would develop a negative charge (due to build-up of electrons), which would cause the image to become defocused due to deflection of the exciting electron beam, abnormal contrast in the image due to the uneven distribution of the negative charge on the sample and breaks or splitting of the image due to high negative charge on the sample which deflects the beam of electrons. Therefore, in order to enhance the number of secondary electrons from an insulating sample, the sample is often coated with a thin layer of gold-palladium or another electron-rich conducting material that produces abundant secondary electrons when struck by a focused electron beam. A thin metal coating will not mask surface features or the overall topology of the underlying sample. The conducting coating also conducts electrons away, so that the sample does not develop a significant charge when it loses secondary electrons and other types of electrons. This type of coating is essential for samples, which do not conduct charged particles.

2.3.4 Transmission electron microscopy

Transmission electron microscopy (TEM) is an imaging technique whereby a beam of electrons is focused onto a specimen causing an enlarged version to appear on a fluorescent screen or to be detected by a CCD camera. It produces a transmitted electron image of a thin specimen magnified from 100 to1000000X with a resolution of 2 Å.

In the present study, high resolution transmission electron microscope (HRTEM); Model: FEI Tecnai-20, was used. The schematic diagram is shown in **figure 2.6**. The system consists of an electron source (Filament: LaB_6). The accelerating voltage is variable between 20-200 kV. Adding a condenser lens provides a means of varying the illumination of the specimen by changing the

33
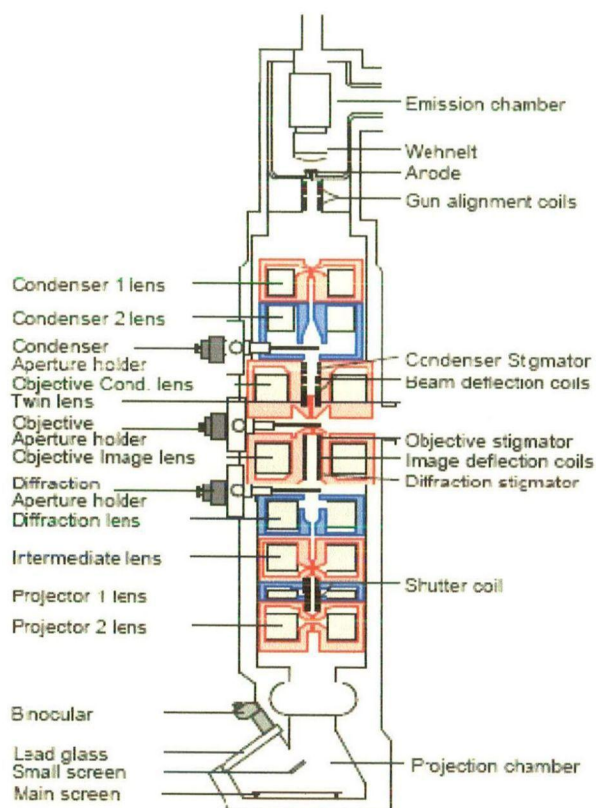
Figure 2.6 Schematic diagram of HRTEM   Photograph of HRTEM (FEI Tecnai-20)
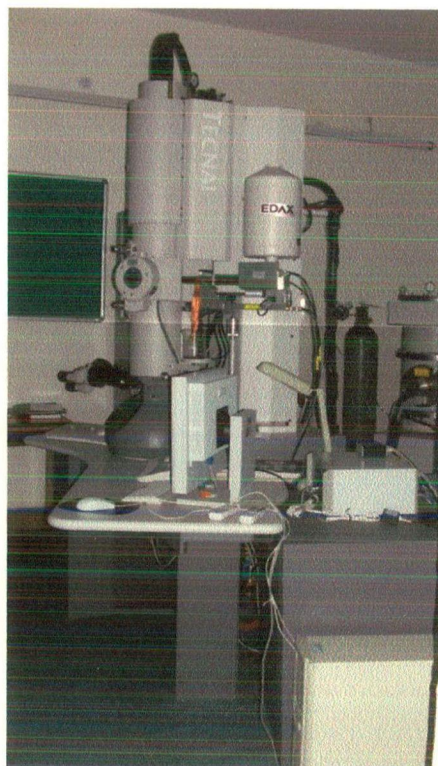
excitation of the lens. Modern TEMs have two condenser lenses. The first condenser lens (C1) is a strong lens, to demagnify the gun. Different currents through (C1) give different spot sizes. Second condenser (week lens) lens is now used to bring the first condenser lens cross-over down to the specimen. The maximum size of the second condenser lens (C2) aperture is determined by the spherical aberration of C2. Sometimes smaller apertures are selected to obtain better coherent illumination. In practice, spot sizes down to approximately 100 nm can be obtained by using this double condenser system. The condenser lenses are fitted with apertures, which are usually small platinum disks with holes of various sizes. Condenser lens apertures protect specimen from too many stray electrons, which can contribute to excessive heat and limit x-ray production farther down the column. The objective lens forms the so-called first intermediate image of the object, which will be enlarged by a lens lower in the column. Because defects of the objective lens are magnified by the total magnification factor, lens is the most critical lens in the microscope. In general,

smaller the focal length (1 to 5 mm) and the lens aberration constants, better will be the resolving power of the microscope. The objective aperture is positioned in the back focal plane of the objective lens for two main reasons:

> Limiting the angular aperture to reduce spherical and chromatic errors, which otherwise would blur the image and reduce the resolving power.

> Intercepting unwanted strongly scattered electrons from the specimen to prevent them from contributing to the image which would otherwise reduce the contrast of the final image.

Final image magnification in a TEM is the product of the magnifications of each magnifying lens: the objective lens, the diffraction lens, the intermediate lens and the projector lens. The objective lens, the first magnifying lens in the TEM, is a high power lens. The diffraction lens, below the objective lens, is a very low power lens. The intermediate lens is a weak lens but with variable power. The current of this lens is adjusted to control the final magnification of the image. The last lens is the projector lens, which is a high power lens that projects the final magnified image on to the viewing screen.

TEM has following modes of operation:

1. **Image Mode:** Imaging mode allows the imaging of the crystallographic structure of a specimen at an atomic scale. Because of its high resolution, it is an invaluable tool to study nanoscale properties of crystalline material. In image mode, image contrast comes from the scattering of the incident electron beam by the specimen. Phase contrast is very sensitive to many factors such as small change in thickness, orientation and variations in the focus of the objective lens. This sensitivity is also the reason that phase contrast can be used to image the atomic structure of thin specimens. By using electrons accelerated to high voltages, atomic planes of the crystal can be resolved (7). In this mode, intermediate aperture is removed and only objective aperture is used. Intermediate lens is focused on the image plane of the objective lens and in image mode, two imaging systems are used:

    (a) **Bright field mode:** When an incident electron beam strikes a sample, some of the electrons pass directly through while others may undergo slight

inelastic scattering from the transmitted beam. Contrast in an image appeared by differences in scattering. By inserting an aperture in the back focal plane, an image can be produced with these transmitted electrons. The resulting image is known as a bright field image. Bright field images are commonly used to examine microstructural related features.

(b) Dark field mode: If a sample is crystalline, many of the electrons will undergo elastic scattering from the various planes. This scattering produces many diffracted beams. If any one of these diffracted beams is allowed to pass through the objective aperture, an image can be obtained. This image is known as a dark field image. Dark field images are particularly useful in examining microstructural detail in a single crystalline phase.

2. Diffraction mode: The diffraction pattern that is always present in the back focal plane of the objective is brought into focus by the objective lens. Individual spots are seen when the specimen is a single crystal, while for polycrystalline material concentric rings are observed.

2.3.5 Atomic force microscopy

The atomic force microscope (AFM) can be compared to traditional microscopes such as the optical or scanning electron microscopes for measuring dimensions in the horizontal axis. However, it can also be compared to profilers for making measurements in the vertical axis to a surface. One of the great advantages of the AFM is the ability to magnify in the X, Y and Z axes.

Unlike traditional microscopes, the AFM does not rely on electromagnetic radiation such as photon or electron beams to create an image. An AFM is a mechanical imaging instrument that measures the two/three dimensional topography with a sharpened probe. In the present study, atomic force microscope from NT-MDT: NTEGRA were used and the photograph is shown in **figure 2.7**. The sharpened probe attached to the lower side of a reflective cantilever, which is positioned close enough to the surface such that it can interact with the force fields associated with the surface. During imaging, light from a diode laser is focused on the cantilever and is reflected on to a four segmented photodiode. As the sample is scanned below the tip, the cantilever moves up and down which changes the ratio of light falling on the
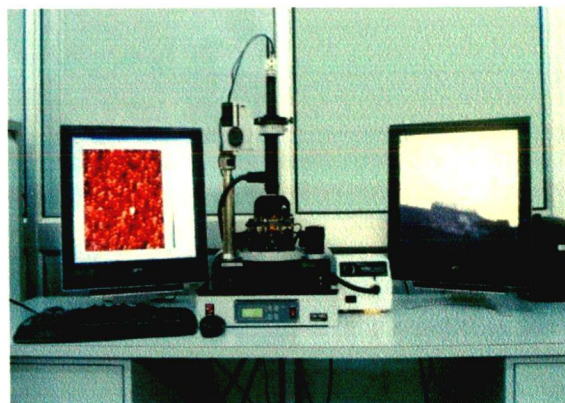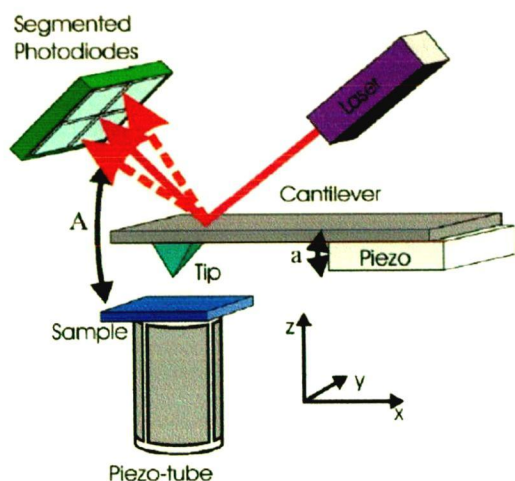
Figure 2.7 Schematic diagram of AFM   Photograph of AFM (NT-MDT: NTEGRA)

four elements of the photodiode. The difference in the intensity falling on the four segments is converted into a proportional voltage by the photodiode. This voltage serves as a feedback signal enabling the tip to maintain either a constant force or a constant height above the sample. An image of the surface is then reconstructed by monitoring the precise motion of the probe as it is scanned over the surface.

For most applications the instrument is operated in one of the following three modes:

(i) Contact mode: Contact mode is typically used for scanning hard samples and when a resolution of greater than 50 nanometers is required. In this mode, as the tip scans the sample in close contact with the surface, a repulsive force on the tip is set by pushing the cantilever against the sample surface with a piezoelectric positioning element. During Scanning, the deflection of the cantilever is sensed and compared in a dc feedback amplifier to some desired value of deflection. If the measured deflection is different from the desired value then the feedback amplifier applies a voltage to the piezo to raise or lower the sample relative to the cantilever to restore the desired value of deflection. The voltage applied by the feedback amplifier to the piezo, is a measure of the height of features on the sample surface. The typical problem with the contact mode is that the tip may scratch the surface and change its intrinsic features.

37

(ii) **Non-contact mode:** In this mode the tip is held at 50 - 150 Å above the sample surface. Attractive Vander Waals forces acting between the tip and the sample are detected, and topographic images are constructed by scanning the tip above the surface. Since the attractive forces from the sample are substantially weaker than the forces used by contact mode therefore the tip is given a small oscillation so that AC detection methods can be used to detect the small forces between the tip and the sample by measuring the change in amplitude, phase, or frequency of the oscillating cantilever. For highest resolution, it is necessary to measure force gradients from Vander Waals forces which may extend only a nanometer from the sample surface.

(iii) **Semi-contact mode:** Semi-contact mode was developed as a method to achieve high resolution without including destructive frictional forces. In this mode, the cantilever is made to oscillate at its natural frequency by using a piezo-electric crystal. The change in oscillation amplitude during the tapping period is used as a feedback to maintain constant height or force between the tip and the sample. The feedback voltage serves as a measure of the surface features. The advantages of the semi-contact mode are that as the tip is not dragged over the sample there is no damage caused to the sample and also the tip is prevented from sticking to the sample surface due to adhesion.

2.4 Measurement of electrical, mechanical and electrochemical properties

2.4.1 Electrical transport measurement

The temperature dependence of the sample resistance was determined by standard four probe technique. This technique is used to eliminate both the lead resistance and the contact resistance. The sample resistance is determined by measuring the low voltage drop between two points of the film, generated by passing a constant current in the range of $1\mu A$-10 mA. Transport measurements of the sample resistance can be determined using the following two methods.

(i) AC measurement technique

(ii) DC measurement technique

In the AC measurement technique, low frequency AC signal is used to measure the sample resistance. Thermal voltages are DC hence they are nullified using an AC measurement method. The problem with using AC signals is the errors due to stray inductance and capacitance in the system. These stray effects are significant unless very low frequency signals are used. In the DC measurement technique the voltage V_1 measured with forward test current, the current is then reversed and corresponding voltage $-V_2$ is measured. If both measurements are taken before thermal gradient the thermal voltages cancel in the final calculation.

$$V_1 (measured) = IR + V_{th} \tag{2.2}$$

$$-V_2 (measured) = -IR + V_{th} \tag{2.3}$$

$$R = V_1 + V_2/2I \tag{2.4}$$

The equation (2.4) is valid only if there is no thermal gradient during the measurement of two voltages (V_1 and V_2).

In the present study, four probe DC resistance measurement technique was used to measure the temperature dependence of sample resistance. The schematic diagram is shown in **figure 2.8**. Silver paste was used for making contacts over the sample. The outer two contacts were used for passing current in the sample and the corresponding voltage drop is measured across two inner contacts. A 100Ω platinum resistance thermometer (Lake Shore Cryotronics, USA) was used as temperature sensors. A heater of Lake Shore Cryotronics, USA was mounted below the sample holder and used to heat the sample up to 450 K. The whole assembly was then dipped in liquid N_2 dewar and the temperature was controlled by temperature controller (Lake Shore Cryotronics, USA). The constant current was fed to the sample through a programmable current source (Keithley, USA 2400) and the voltage drop was measured by a digital nanovoltmeter (Keithley, USA 2182A). The automatic recording of data was done using computer software.
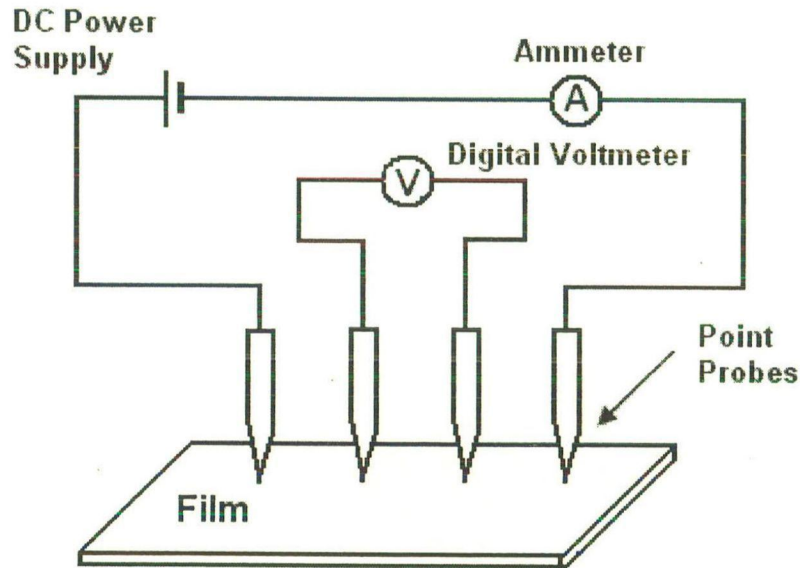
Figure 2.8   Schematic diagram of four probe resistivity measurement set up.

2.4.2 Nanoindentation

Nanoindentation is a powerful tool for investigating hardness, elastic modulus and other mechanical properties of materials in small dimensions **(8, 9)**. Nanoindentation test involves indenting a specimen by a very small load using a high precision instrument, which records the load and displacement simultaneously. The mechanical properties of thin films and substrates can be derived from the load-displacement loading/unloading curve through appropriate data analysis. In nanoindentation, a prescribed load is applied to a pyramidal or spherical indenter probe or other shapes in contact with the specimen surface. Indenter probe is driven into the sample and then withdrawn by decreasing the applied force. The applied load (P) and depth of penetration (h) into the sample are continuously monitored and a load versus displacement curve is obtained. **Figure 2.9** depicts an example of a load versus depth curve in which the load is increased at a constant rate to some peak value (loading), held at that value for a set amount of time, and then decreased to zero (unloading). The sample hardness (H) and reduced elastic modulus (E_r) can then be calculated from the load-displacement curve as shown in **figure 2.9**.

In the present study, Hysitron Triboindenter was used to perform nanoindentation tests on these films to determine the hardness, reduced modulus and
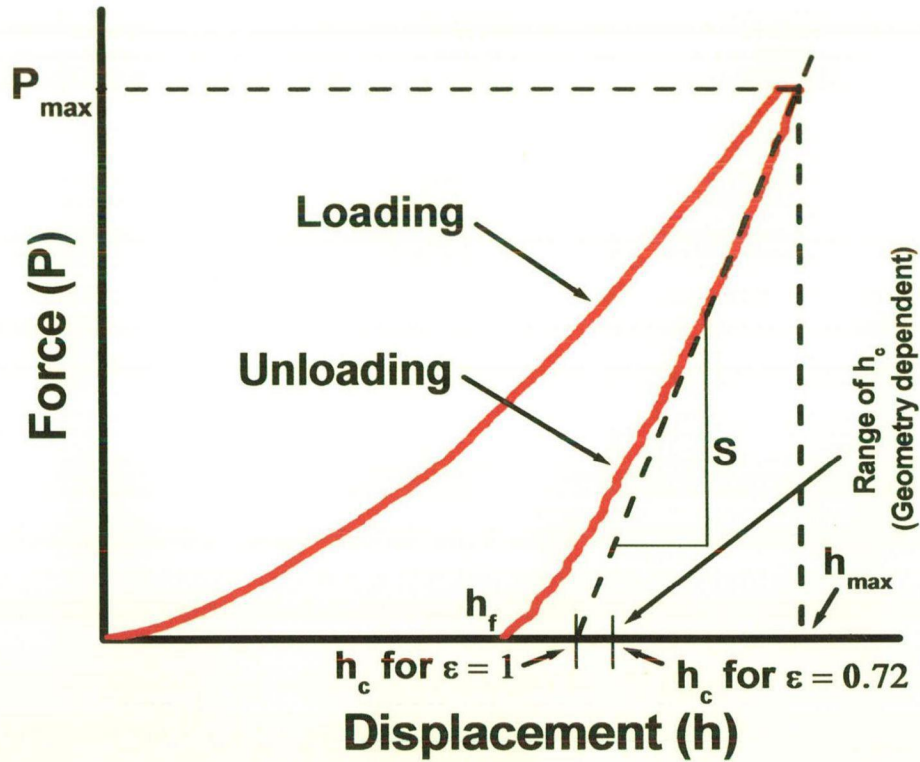
Figure 2.9   Load versus displacement curve.

other mechanical properties. The desired parameters were calculated by using following relations:

The reduced modulus is defined by the equation:

$$E_r = \frac{S\sqrt{\pi}}{2\sqrt{A}}$$

(2.5)

where S (unloading stiffness) = $\frac{dP}{dh}$ and A is the projected contact area.

The reduced modulus is related to the modulus of elasticity (E) through the equation:

$$\frac{1}{E_r} = \frac{\left(1 - v_i^2\right)}{E_i} + \frac{\left(1 - v_s^2\right)}{E_s}$$

(2.6)

where the subscript i corresponds to the indenter material, the subscript s refers to the indented sample material, and v is Poisson's ratio. For a diamond indenter probe, E_i

41

is 1140 GPa and v_i is 0.07 **(10)**.

The unloading stiffness (S) is calculated by fitting the unloading curve to the power law relation:

$$P = A(h - h_f)^n$$

(2.7)

where A, h_f, and m are arbitrary fitting parameters. The stiffness can be calculated from the derivative of the equation given below:

$$S = \frac{dP}{dh}(h_{max}) = mA(h_{max} - h_f)^{m-1}$$

(2.8)

The hardness (H) is defined by the ratio of the maximum load (P_{max}) to the projected contact area (A),

$$H = \frac{P_{max}}{A}$$

(2.9)

The contact area is determined from a probe calibration function A (h_c), where h_c, the contact depth, is found by using the equation:

$$h_c = h_{max} - \varepsilon \frac{P_{max}}{S}$$

(2.10)

To account for edge effects, the deflection of the surface at the contact perimeter is estimated by taking the geometric constant ε as 0.75.

2.4.3 Voltammetry

Electrochemical experiments were performed in differential pulse voltammetry (DPV) mode using BAS (Bioanalytical Systems, West Lafayette, IN, USA) CV-50W Voltammetric analyzer **(figure 2.10)**. Differential pulse voltammetry can be considered as a derivative of linear sweep voltammetry or staircase voltammetry, with a series of regular voltage pulses superimposed on the potential linear sweep or stair steps **(figure 2.10)**. The current is measured immediately before each potential change, and the current difference is plotted as a function of potential. Resultant differential pulse Voltammograms are peak shaped and their height is directly proportional to the concentration of the corresponding analytes. The basis of the
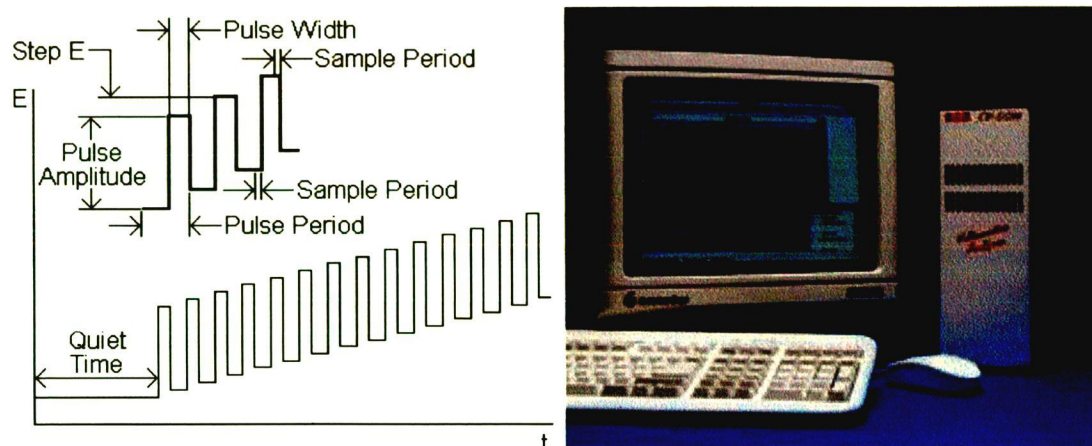
Figure 2.10   Series of regular voltage pulses superimposed on the potential linear sweep and photograph of BAS, CV-50W Voltammetric analyzer.

technique is the difference in the rate of the decay of the charging and the faradic currents after pulse application. The rate of decay of the charging current is much faster in comparison to faradic current. Hence, by measuring the current at the end of the pulse allows recording of the faradic current because charging current becomes negligible at this stage. Suppression of charging current helps in achieving lower detection limits **(12)**. Differential pulse voltammetry gives better detection limit in comparison to linear sweep voltammetry and cyclic voltammetry. Due to its peak shaped nature, DPV offers another advantage of well resolved peaks of closely spaced electrode processes. It makes possible to simultaneously monitor more than one electroactive species present in solution at one time.

Electrochemical cell set-up

A typical electrochemical cell consists of the sample dissolved in a solvent, an ionic electrolyte, and three (or sometimes two) electrodes. In most cases the reference electrode should be as close as possible to the working electrode; in some cases, to avoid contamination, it may be necessary to place the reference electrode in a separate compartment.

Reference electrode: The most commonly used reference electrodes for aqueous solutions are the calomel electrode, with potential determined by the reaction $Hg_2Cl_2(s) + 2e^- = 2Hg(l) + 2Cl^-$ and the silver/silver chloride electrode (Ag/AgCl),

with potential determined by the reaction $AgCl(s) + e^- = Ag(s) + Cl^-$. In the present study, silver/silver chloride electrode (Ag/AgCl) was used to perform electrochemical studies.

Counter electrodes: The Counter electrode's potential is opposite in sign to that of the working electrode, but its current and potential are not measured. Rather, it is used to ensure that current does not run through the reference electrode, which would disturb the reference electrode's potential. The auxiliary electrode often has a surface area much larger than that of the working electrode to ensure that the reactions occurring on the working electrode are not surface area limited by the auxiliary electrode. Most often the counter electrode consists of a thin Pt/Au wire and sometimes graphite can be used. In the present study Pt wire was used as counter electrode.

Working electrodes: In the present study, the nanocrystalline thin films deposited on silicon (100) substrate were used as working electrodes.

2.7   References

(1) Shih C. L., Lai B. K., Kahn H., Philips S. M. and Heuer A. H., "A robust Co-sputtering fabrication procedure for TiNi shape-memory alloys for MEMS", Journal of Microelectromechanical systems, 10, 69-79 (2001).

(2) Anders A., "Plasma and ion sources in large area coating: A review", Surface & Coatings Technology, 200, 1893-1906 (2005).

(3) Krulevitch P., Lee A. P., Ramsey P. B., Trevino J. C., Hamilton J. and Northrup M. A., "Thin film shape memory alloy microactuators", Journal of Microelectromechanical systems, 5, 270-282 (1991).

(4) McLeod P. S. and Hartsough L. D., "High-Rate Sputtering of Aluminum for Metalization of Integrated Circuits", Journal of Vacuum Science and Technology, 14, 263-270 (1977).

(5) Waits R. K., "Planer Magnetron sputtering", Journal of Vacuum Science and Technology, 15, 179-187 (1978).

(6) Cullity B. D. and Stock S. R., "Elements of X-Ray Diffraction", 3rd Ed., Prentice Hall, New Jersey (2001).

(7) Fleger S. L., Heckman J. W., Karen J. and Klomparens L., "Scanning and Transmission Electron Microscopy: An Introduction", Oxford University Press, New York (1993).

(9) Li D., Chung Y. W., Wong M. S. and Sprout W. D., "Nano-indentation studies of ultrahigh strength carbon nitride thin films", Journal of Applied Physics, 74(1), 219-223 (1993).

(10) Dhara S., Das C. R., Hsu H. C., Raj B., Bhaduri A. K, Chen L. C., Chen K. H., Albert S. K., and Ray A., "Recrystallization of epitaxial GaN under indentation", Applied Physics Letters, 92, 143114 (2008).

(11) Oliver W. C. and Pharr G. M., "An improved technique for determining hardness and elastic modulus using load and displacement sensing indentation experiments", Journal of Materials Research, 7, 1564-1583 (1992).

(12) Bard A. J. and Faulkner L. R., Electrochemical Methods Fundamentals and Applications, Wiley, NY, USA, p. 275 (2001).

Chapter 3

Grain Size & Film Thickness Effect in NiTi Thin Films

CHAPTER 3

GRAIN SIZE AND FILM THICKNESS EFFECT IN NiTi THIN FILMS

3.1 Grain size effect on structural, electrical and mechanical properties of NiTi thin films

    3.1.1   Introduction

    3.1.2   Experimental details

    3.1.3   Results and discussion

            3.1.3 (a)   Structural properties

            3.1.3 (b)   Electrical properties

            3.1.3 (c)   Mechanical properties

    3.1.4   Conclusions

3.2 Influence of film thickness on phase transformation behavior of sputtered NiTi thin films

    3.2.1   Introduction

    3.2.2   Experimental details

    3.2.3   Results and discussion

            3.2.3.1   Structural properties

            3.2.3.2   Electrical properties

    3.2.4   Conclusion

3.3 References

3.1 Grain size effect on structural, electrical and mechanical properties of NiTi thin films

3.1.1 Introduction

Significant efforts have been devoted to explore the shape memory effect and pseudoelastic behaviour of NiTi bulk. The effect of grain refinement over martensitic transformation in NiTi bulk has been reported by several research groups (1, 2). In spite of that the knowledge of such phenomenon in NiTi thin films is sparse. As a candidate material for microactuation, NiTi shape memory films have attracted renewed interest because of their fast response, competitively large transition forces, and a strain recovery rate comparable to these of the bulk material (3, 4). Recent advances in semiconductors processing techniques and MEMS systems have turned the research attention to SMA thin films. Consequently, the systematic study is required to understand the associated phase transformation mechanism of NiTi thin films for scientific and industrial importance.

In the present study, NiTi thin films were deposited by dc magnetron co-sputtering on Si (100) substrate at various substrate temperatures ranging from room temperature to 923 K. There are reports on composition effect, crystallization behavior, shape memory and pseudo elastic behavior, of dc sputtered NiTi thin films (5-14). The aim of present study was to examine the effect of grain size on the crystallinity, surface morphology and phase transformation behaviour of NiTi thin films. Substrate temperature was varied during deposition in order to achieve different grain size. It was observed that the martensitic transformation behavior of these films depend critically on its microstructure and its dimensional constraint. The NiTi film deposited at substrate temperature (T_S) of $\leq$ 623 K exhibited negative thermal coefficient of resistance (TCR) value and non-metallic behavior, while the film deposited at T_S of $\geq$ 723 K showed metallic behaviour.

3.1.2 Experimental details

Silicon substrates were initially cleaned thoroughly in an ultrasonic bath with a mixture of distilled water and trichloroethylene in 4:1 ratio and then washed with boiled acetone. High purity (99.99%) titanium and nickel metal targets of 50 mm

diameter and 3 mm thickness were used. Before every sputtering run, the targets have been pre-sputtered for 5 min in order to ascertain the same state of the targets in every run. Suitable powers were applied to each target to give similar deposition rates of Ni and Ti. Substrate holder was rotated axially at 20 rpm to achieve a uniform film composition. Deposition parameters are listed in **table 3.1**. Both magnetron guns were tilted at an angle of 45° so that the plasma from both the targets can be concentric. The Ti/Ni ratio was determined from energy dispersive x-ray analysis (EDAX). The film thickness was measured using a surface profilometer and cross sectional FESEM and was found to vary from 2.2 to 2.5 μm with increase in substrate temperature from 623 to 923 K. Post annealing was not performed after deposition.

The orientation and crystallinity of the films were studied using x-ray diffractrometer of CuKα (1.54Å) radiations in θ-2θ geometry at a scan speed of 1°/min. To make sure of absolute values of the 2θ diffraction angles, the diffractrometer was calibrated with respect to the peak position of a Si calibration standard. A polycrystalline powder was used for instrumental correction. The coherently diffracting domain size (d_{XRD}) was calculated from the integral width of the diffraction lines using the Scherrer's equation **(15)**, after background subtraction

Table 3.1   Sputtering parameters for NiTi thin film.

Target	Ti, Ni
Base pressure	$\leq 2 \times 10^{-6}$ Torr
Gas Used	Ar
Sputtering pressure	10 mTorr
Deposition time	30 min
Sputtering power for Ti target	120 W
Sputtering power for Ni target	40 W
Substrate	Silicon(100)
Substrate Temperature	RT-923K
Substrate to Target Distance	5 cm

and correction of instrumental broadening. The surface topography and microstructure were studied using field emission scanning electron microscope and atomic force microscope. The microstructure was also investigated using high resolution transmission electron microscopy. The resistivity of the films was measured by four probe resistivity method using a liquid nitrogen cryocooler and Keithley instruments over a temperature range from 100 to 400 K. The contacts over the samples were made by silver paint.

A Hysitron Triboindenter was used to perform nanoindentation tests. Sixteen nanoindentation tests were performed on each sample using a diamond Berkovich indenter probe to determine the hardness and reduced modulus. Each test consisted of a five-second linear loading segment to a peak load, followed by a two-second holding segment at the peak load, and finally a five-second linear unloading segment. The maximum load was set at 3.5 mN in order to minimize the substrate influence on the indentation response of the films.

3.1.3   Results and discussion

3.1.3.1   Structural properties

The martensite transformation and superplasticity of NiTi films are sensitive to the deposition temperature, post-annealing temperature and duration (16, 17). The films deposited at room temperature were usually amorphous in nature. Therefore high temperature deposition or post annealing was required to make them crystalline. It is suggested that postannealing should be done at lowest possible annealing temperature for minimum annealing duration to minimize the reaction between film and substrate otherwise it could lead to dramatic changes in the film microstructure, mechanical properties and shape memory effects (16). An alternative method to avoid high temperature treatment is to grow the NiTi thin films on heated substrates during deposition. The films deposited at relatively higher substrate temperature ($\geq$ 723 K) do not require post annealing and these are insitu crystallized (18). In order to see the impact of grain size on microstructural and phase transformation behaviour of NiTi films, various films were prepared at different substrate temperature to vary the grain size and no post annealing was performed on these films.
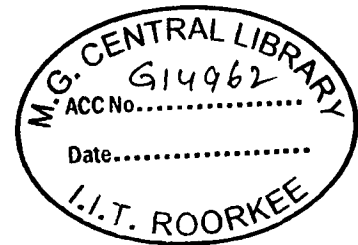
Figure 3.1 shows the XRD pattern of NiTi films deposited at substrate temperatures of 623, 723, 823 and 923 K. The NiTi film deposited at substrate temperature (T_s) of 623 K was amorphous in nature while the film deposited at T_s of 723 and 823 K exhibited the reflection from (110) plane of the austenite parent phase. This showed that crystallization starts in NiTi films grown onto Si (100) substrate at the deposition temperature as low as 723 K. XRD pattern confirmed that the dominant phase at room temperature was austenite in the film deposited at T_S of ≤ 823 K while the film deposited at T_s of 923 K showed sharp peak of (-111) reflection at $2\theta = 41.7°$ and other less intensity peaks of (002) and (110) reflections correspond to monoclinic martensitic structure **(Figure 3.1)**. Increase in substrate temperature from 623 to 823 K enhanced activity of absorbed atoms on the substrate and accelerates the migration of the atoms to the favorable energy positions that favors to the formation of closed packed structure to reduce the surface energy of the grown film, which lead to development of the strong (110) plane texture. Moreover, the rapid crystallization of sputtered atoms would confine the crystallized grains within a very small size. Further increase in substrate temperature, above eutectoid temperature of NiTi compound ($T_e = 903$ K) **(19)**, would facilitate small grains to be aggregated and grow, which could be responsible for the dominance of martensitic phase at room temperature in the NiTi film deposited at T_s of 923 K. The mean crystallographic domain size or particle size was estimated from the true broadening of the XRD lines, using the Sherrer's formula **(15)**. Estimated average crystallite size of the films deposited at 723, 823 and 923 K was found to be 17.2, 26.7 and 53.4 nm, respectively corresponding to the (110) peak broadening of austenitic phase.

The surface morphology of these films was analyzed using atomic force microscopy and is shown in **figure 3.2**. AFM micrographs revealed that the NiTi film deposited at 723 and 823 K shows non facets grains **(figure 3.2 (b) and (c))** with average surface roughness of 6.75 and 8.12 nm, respectively while facets with preferential in-plane orientation of martensitic phase (martensitic plates) **(figure 3.2 (d))** was observed for the film deposited at 923 K. It was observed that the grain size increases with increase in substrate temperature, which was in agreement with the
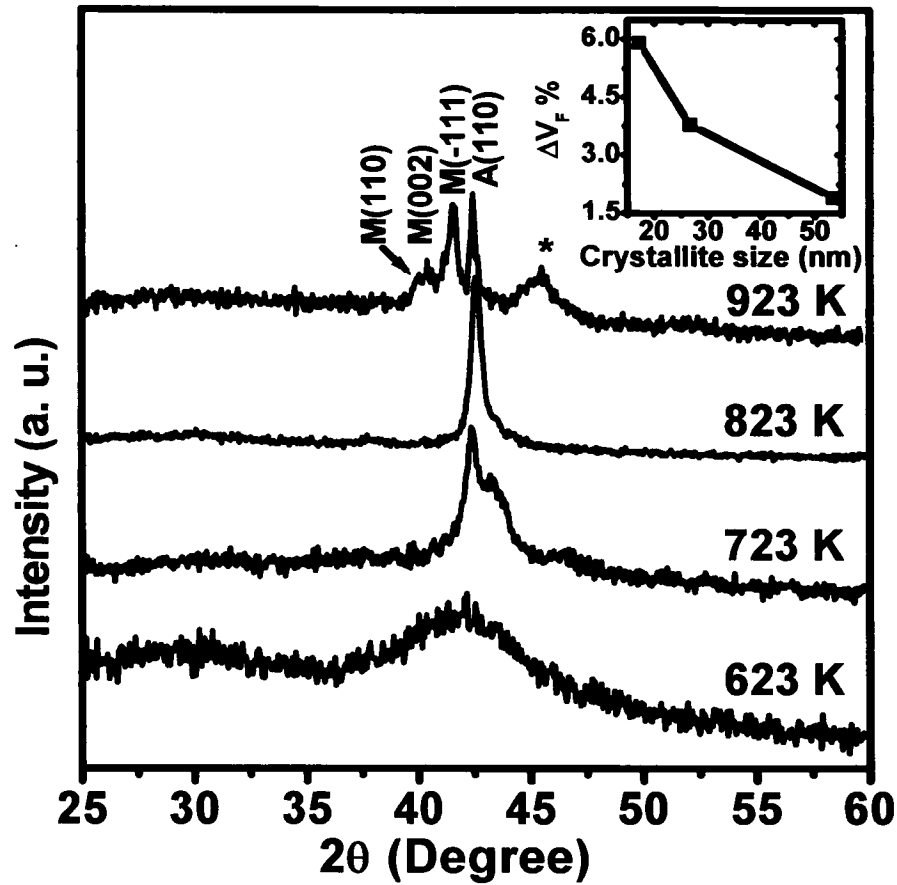
Figure 3.1   XRD pattern of NiTi films deposited at T_s of 623, 723, 823 and 923 K.

Table 3.2   Various parameters of NiTi films deposited at T_s of 623, 723, 823 and 923 K.

S. No	Substrate Temperature (K)	Grain Size (nm)				Avg. Roughness (nm)	EDAX At. wt. % Ti : Ni
		XRD along (110) Peak	FESEM	TEM	AFM		
1.	623 K	--	21.7	20.1	22.2	3.87	49.7 : 50.3
2.	723 K	17.2	38.3	33.6	39.6	6.75	49.9 : 50.1
3.	823 K	26.7	77.7	67.0	80.0	8.12	50.2 : 49.8
4.	923 K	53.4	108.2	98.2	112.5	23.4	50.6 : 49.4
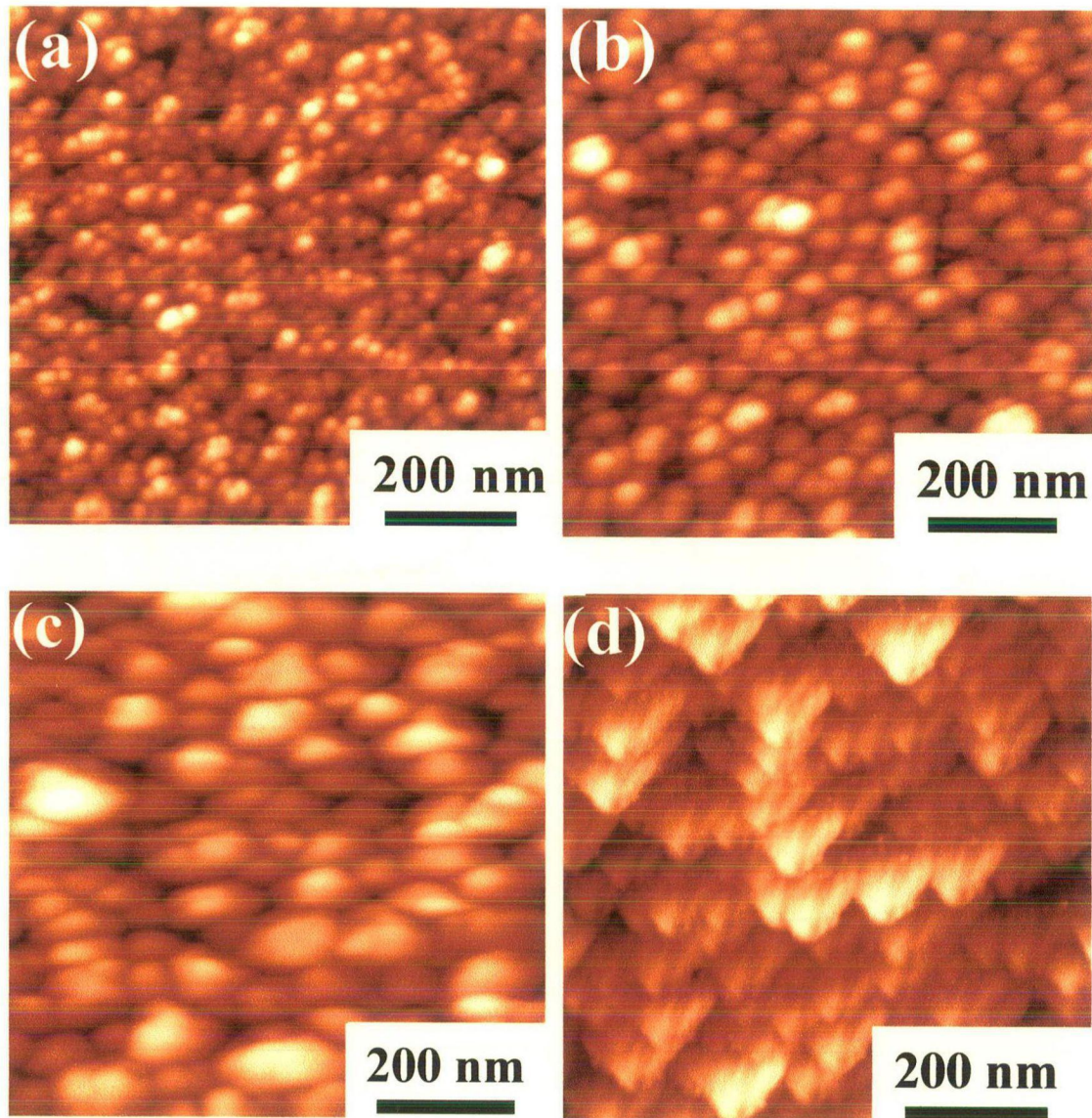
Figure 3.2   AFM images of NiTi films deposited at T_s of **(a)** 623 K, **(b)** 723 K, **(c)** 823 K and **(d)** 923 K.

XRD results as reported in **table 3.2**. It has been proposed that the grain boundaries impose constraints on the growth of the martensite and confine the transformed volume fraction in the nanocrystalline structure. A martensite plate nucleated within a grain will be stopped at the grain boundaries acting as obstacles for martensite growth. To propagate the transformation, the plate has to exert stresses that are sufficient to stimulate nucleation and growth of favourable martensite variants in the adjacent grains **(20)**. In order to estimate the density of grain boundaries, the excess
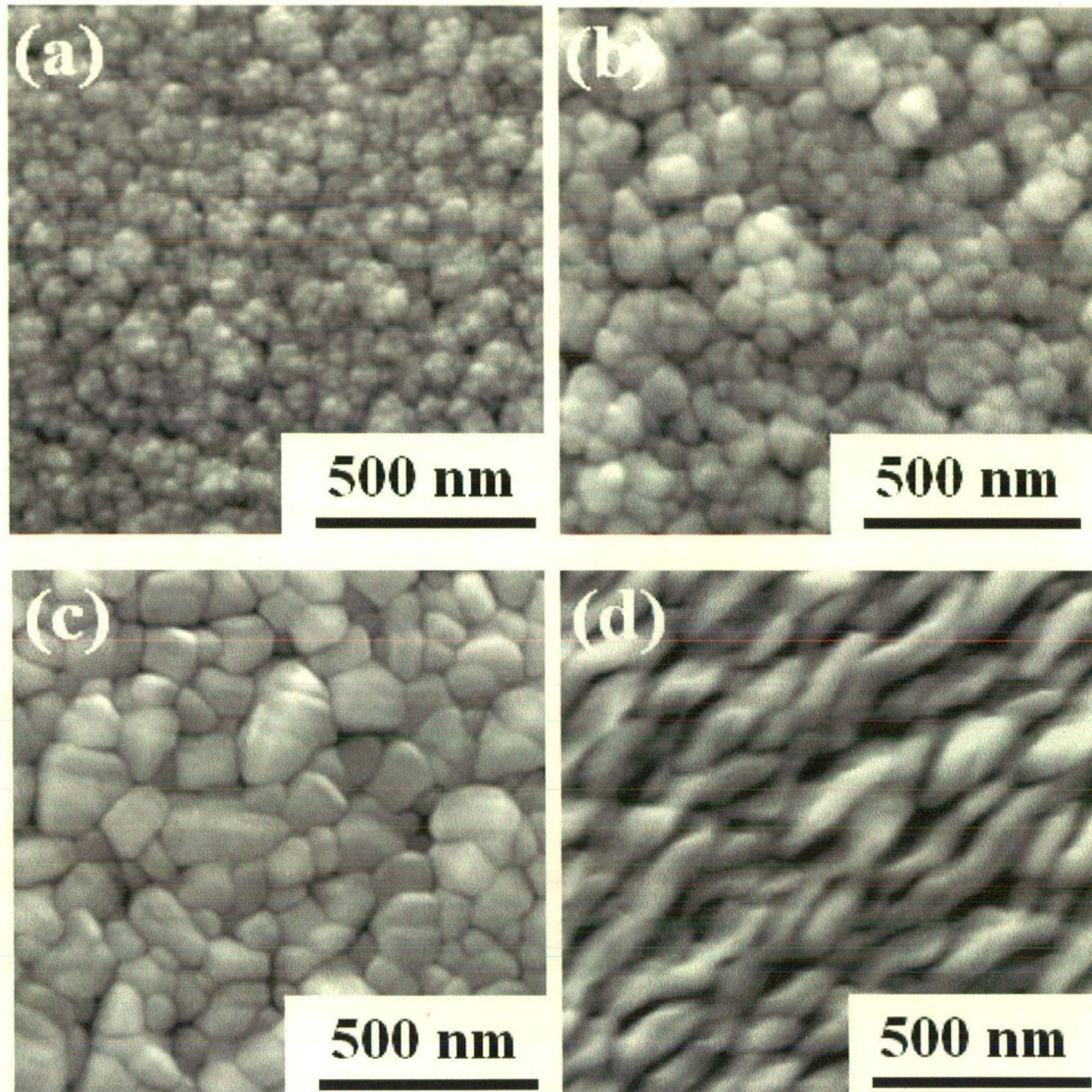
Figure 3.3   FESEM images of NiTi films deposited at T_s of **(a)** 623 K, **(b)** 723 K,
(c) 823 K and **(d)** 923 K.

free volume associated (ΔV_F) with the grain boundaries were calculated using the following expression **(21)**:

$$\Delta V_F = \frac{(L + d/2)^2 - L^2}{L^2} \qquad (3.1)$$

Where, L is the crystallite size and d is the mean width of the grain boundaries. In most of the prior calculations of the excess free volume, the width of the grain boundary has been assumed to be constant (d = 1 nm), independent of the grain size.
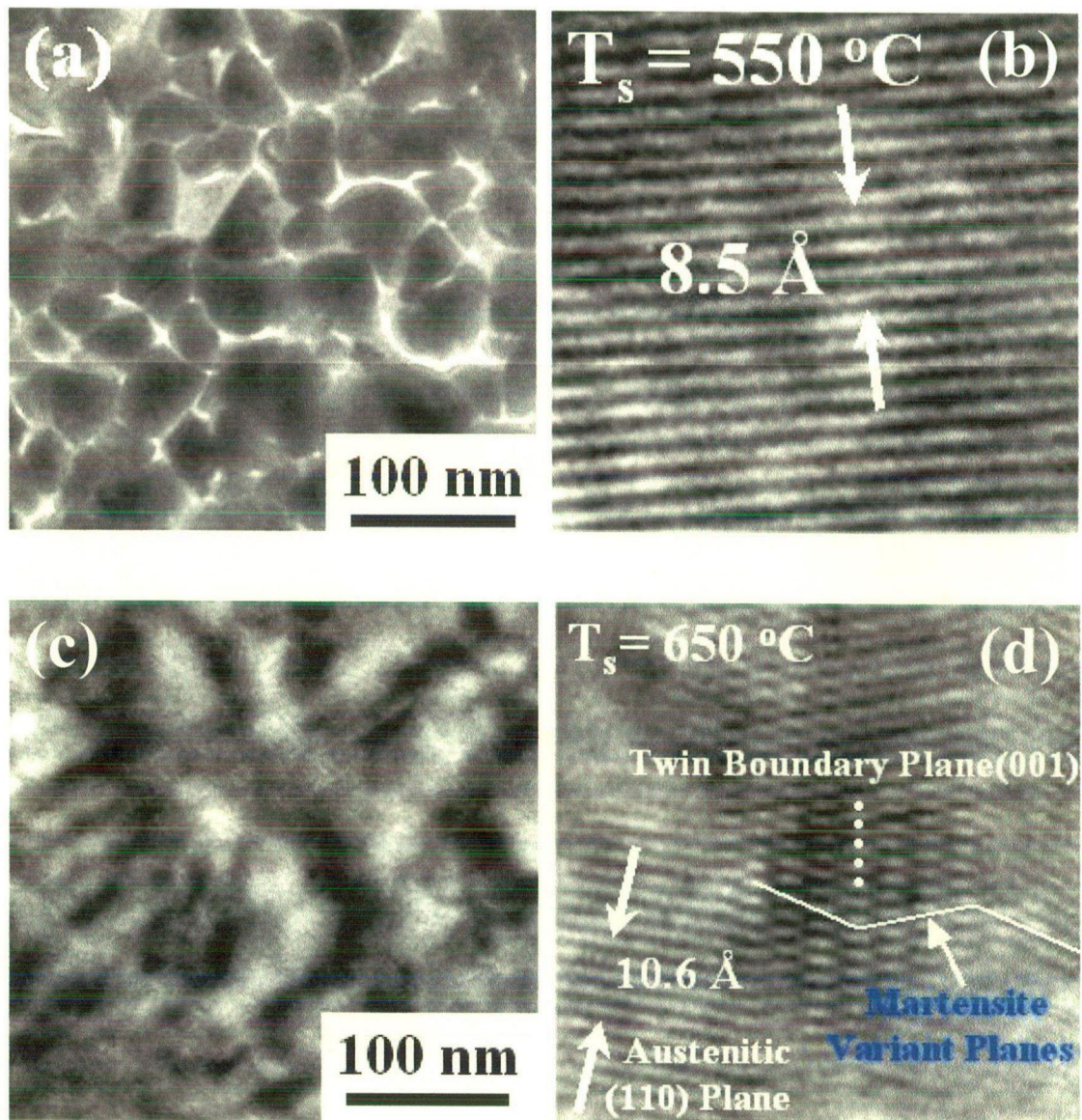
Figure 3.4   TEM micrographs of NiTi film deposited at T_s of **(a)** 823 K and **(c)** 923 K; High resolution lattice images of NiTi film deposited at T_s of **(b)** 823 K and **(d)** 923 K.

The variation of excess free volume with crystallite size has been shown in the inset of **figure 3.1**. It was observed that the grain boundary free volume increases with decrease in crystallite size, hence, grain boundaries increases with decrease in crystallite size. Also, with the decrease in grain size, the number of grain boundaries per unit area and the number of boundary interfaces increases.

Figure 3.3 (a) to **(d)** show the FESEM micrographs that clearly resolved the change of microstructure of NiTi thin films deposited at substrate temperatures of 623, 723, 823 and 923 K, respectively. The grain size of these films was estimated using FESEM micrographs, which clearly revealed the increase in grain size with increase in substrate temperature as reported in **table 3.2**. A slight change in film composition was observed with change in substrate temperature. Atomic weight percentage of Ni and Ti in these films is reported in **table 3.2**. The microstructure of these films was also investigated using high-resolution transmission electron microscopy (HRTEM) at electron beam energy of 200 KeV. **Figure 3.4 (a)** and **(c)** show the TEM micrographs of the NiTi film deposited at substrate temperature of 823 and 923 K respectively, which are in agreement with the FESEM and AFM results. High-resolution lattice images of these films are shown in **figure 3.4 (b)** and **(d)**. In case of the film deposited at the substrate temperature of 823 K, the lattice image shows a lattice spacing of 2.1 Å, which is in the agreement with the 'd' spacing of (110) plane of austenitic phase (**Figure 3.4 (b)**). **Figure 3.4 (d)** shows the lattice image of the film deposited at T_s = 923 K, which revealed the mixed phase i.e. d spacing of 2.1 Å corresponds to (110) plane of austenitic phase and the compound twins of (001) plane yielding a minimum width of four lattice planes (8.5 Å) exhibited martensitic phase.

To gain further insight, hot stage insitu atomic force microscopy was used in order to investigate the surface morphology transition between austenite and martensite phase as a function of temperature. The sample was pre-cooled by liquid nitrogen below a temperature of 250 K, and then heated back to room temperature in atmosphere. **Figure 3.5 (a)-(d)** show the two dimensional surface morphology of the NiTi film deposited at 923 K with increasing temperature i.e. 298, 328, 358 and 388 K, respectively. Each measurement was made after the temperature was stabilized. With increase in temperature the martensitic plate like structure starts to disappear and completely dissolved in to the background at the temperature of 388 K, which confirmed the phase transformation between martensite and austenite phase. The root mean square (rms) roughness quantitatively identifies the surface roughness of these films. In the subsequent heating/cooling cycle, surface roughness
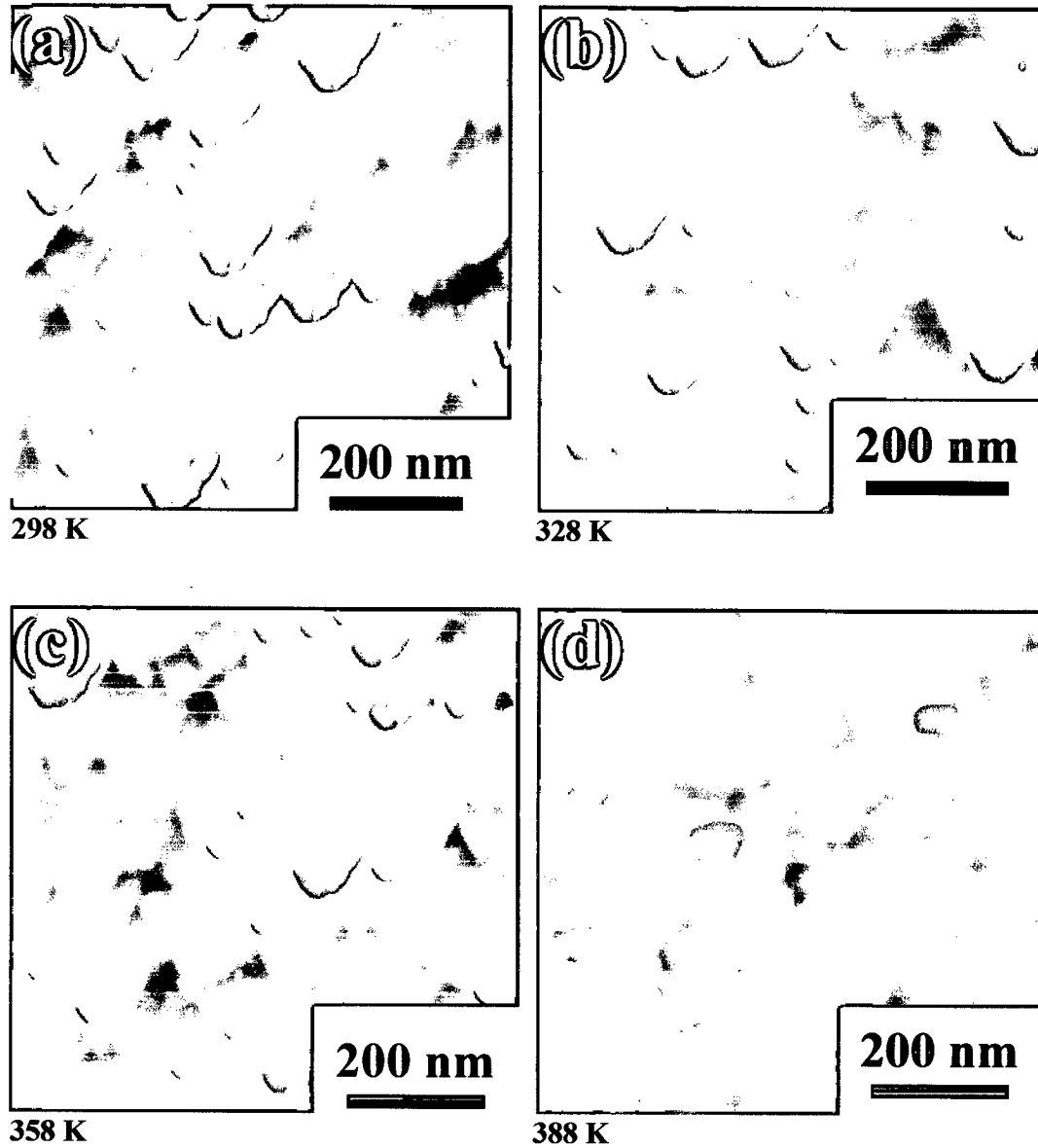
Figure 3.5 Hot stage AFM images of NiTi films deposited at T_s of 923 K at different temperatures **(a)** 298 K, **(b)** 328 K, **(c)** 358 K and **(d)** 388 K.

of the scanned area was measured in-between the temperature range from 298 to 388 K with step size of 15 K as shown in **figure 3.6**. The surface roughness of the martensite phase was found to be much higher as compared to that of austenite phase. As the temperature increases, the surface roughness decreases drastically that clearly confirm the phase transformation between martensite and austenite phases.
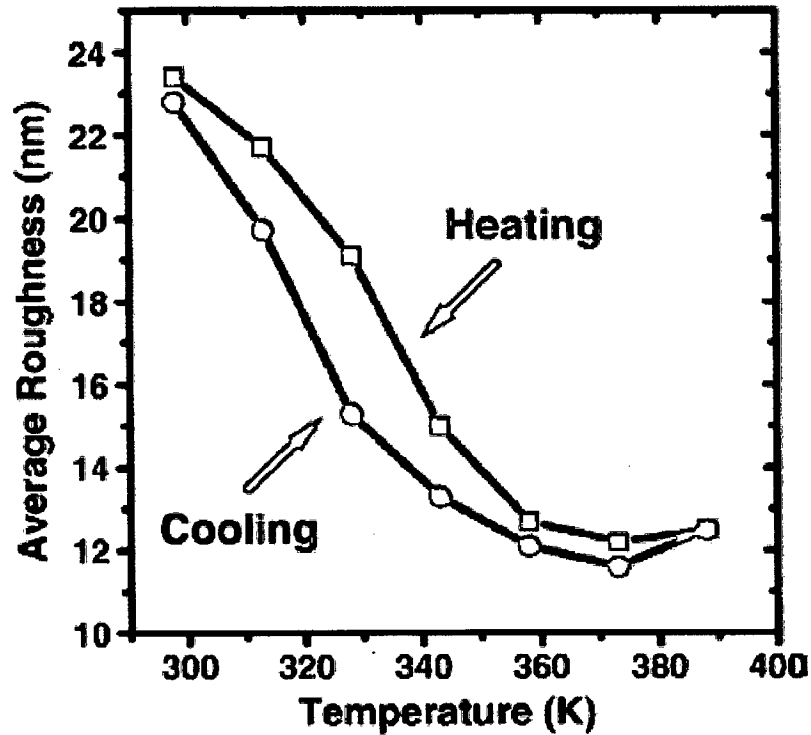
Figure 3.6 Surface roughness versus NiTi film temperature.

3.1.3.2   Electrical properties

Matthiessen's rule states that the total electrical resistance of an alloy is the sum of the resistance due to electron scattering by phonons and the resistance due to electron scattering because of lattice imperfections and impurities. Phase transformation affects the density of lattice imperfection, therefore, electrical resistance versus temperature response provides an effective means for detecting the formation of various phases in shape memory alloys.

The electrical resistance versus temperature (R-T) plots of NiTi films grown at various substrate temperatures are shown in **figure 3.7** and corresponding transformation temperatures are reported in **table 3.3**. The temperature dependence of electrical resistance was measured in the temperature range of 100-400 K during subsequent heating and cooling cycles. The R-T plot of the film deposited at T_S of 623 K **(Figure 3.7 (a))** exhibited nonmetallic behavior with negative thermal coefficient of resistance (TCR) value **(figure 3.8 (a))**. The observed behavior could be attributed to the following reasons: (a) due to the presence of intrinsic defects **(22)**; (b) Austenite $\leftrightarrow$ R – phase transition that can occur in the amorphous
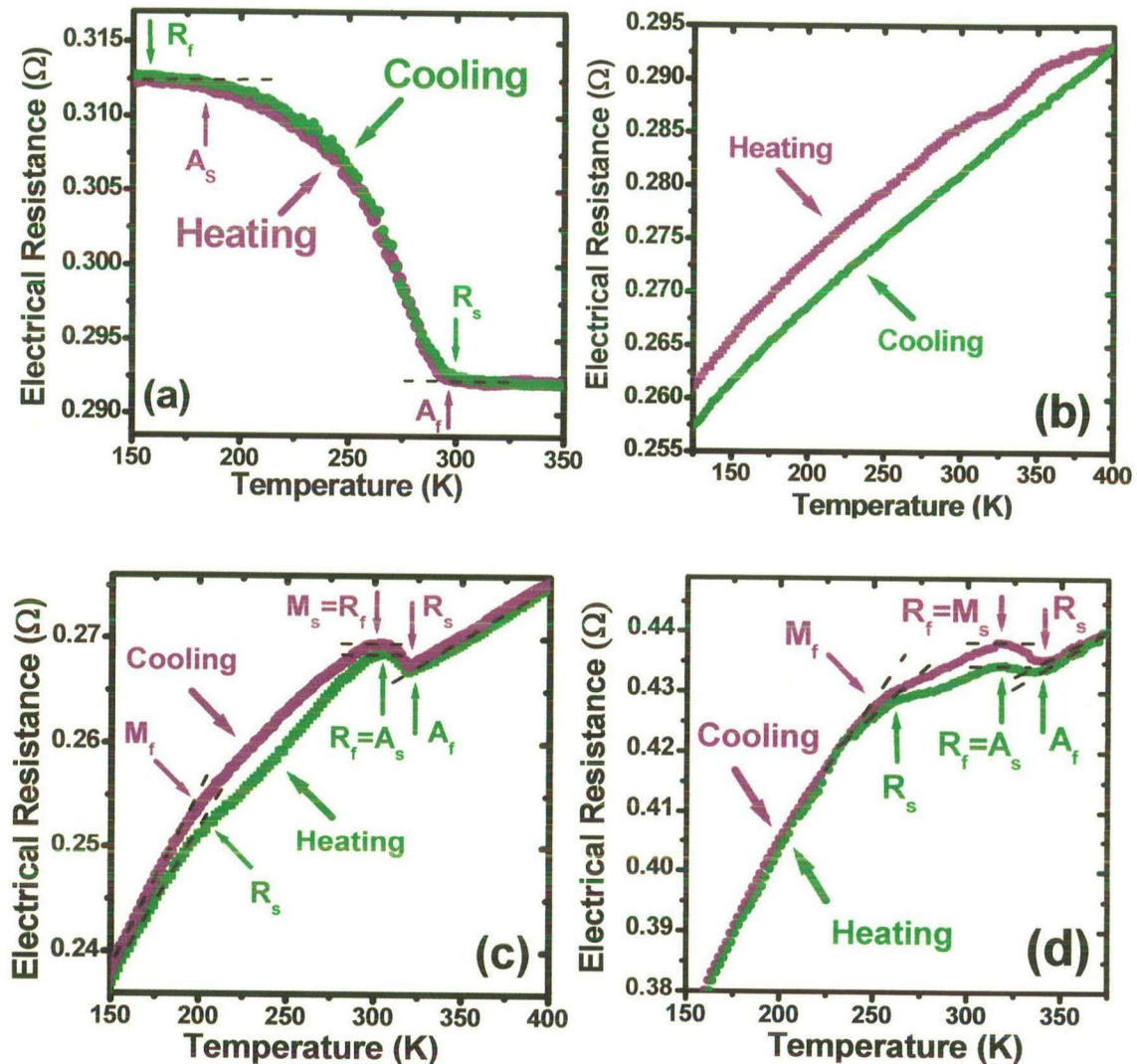
Figure 3.7   Electrical resistance versus temperature curve of NiTi films deposited at
T_s of **(a)** 623 K, **(b)** 723 K, **(c)** 823 K and **(d)** 923 K.

nanocrystalline alloys **(23)**. During cooling, self accommodation R-phase transformation commenced at temperature of 300 K and austenite parent phase began to transform to the twinned R–phase with further decrease in temperature. Cooling of the sample even up to 150 K resulted only in R-phase transformation. Both the lattice distortion and twinning are reversible process in R-phase transformation, therefore, R-T plots does not exhibit temperature hysteresis (**figure 3.7 (a)**).
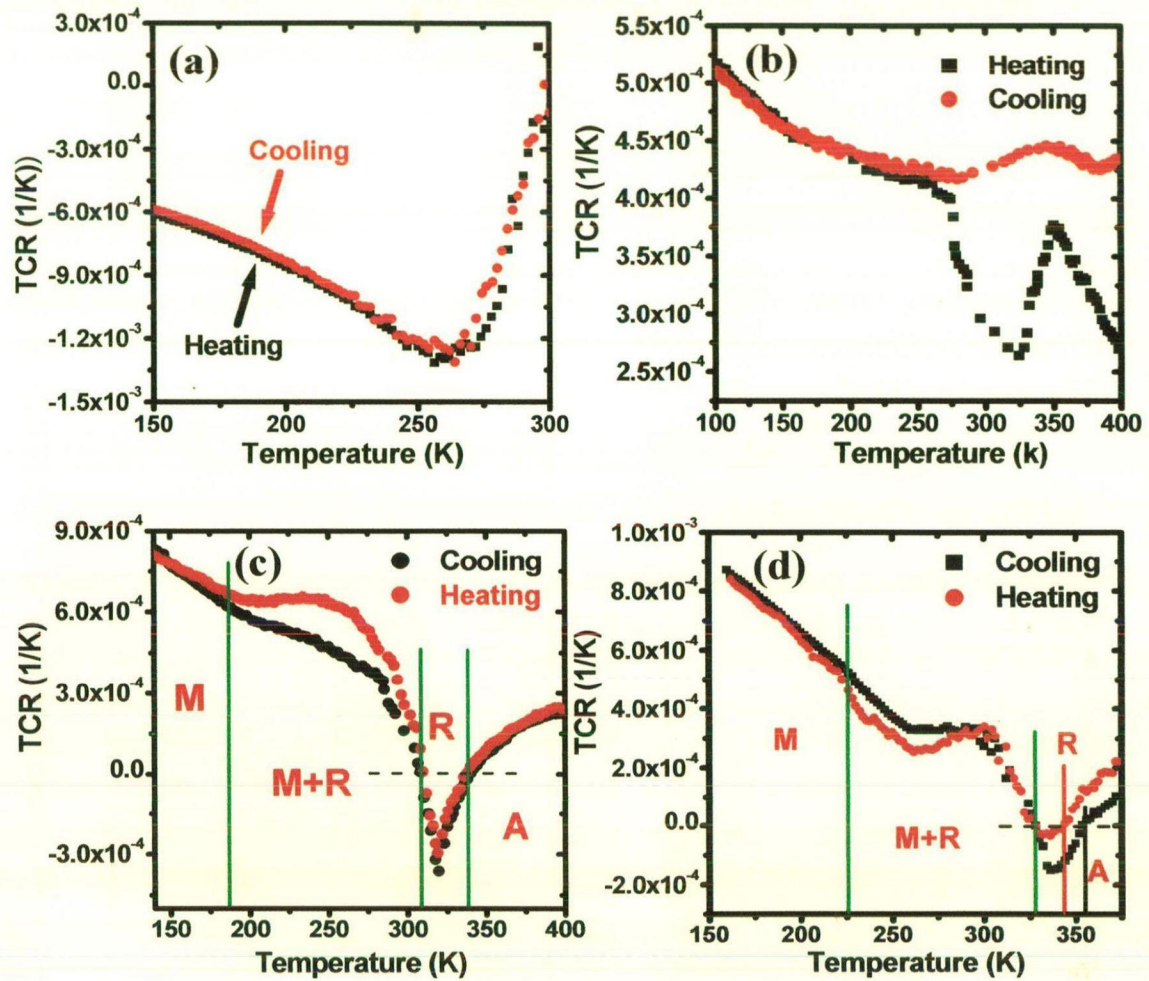
Figure 3. 8 Thermal coefficient of resistance versus temperature curve of NiTi films deposited at T_s of **(a)** 623 K, **(b)** 723 K, **(c)** 823 K and **(d)** 923 K.

Table 3.3 Details of transformation temperatures obtained from electrical resistance versus temperature curves of NiTi films deposited at T_s of 823 and 923 K.

S. No	Substrate Temperature (K)	Transformation Temperature (K)						Hysteresis Width (K)
		Heating			Cooling			
		R_s	$R_f = A_s$	A_f	R_s	$R_f = M_s$	M_f	
1.	823	208	302	320	318	304	200	18
2.	923	260	319	341	339	316	252	24

61

With increasing substrate temperature, the progressive crystallization of the samples induced an evident diminishing of the intrinsic defect, which yields the resistance versus temperature behaviour to change from nonmetallic (observed in amorphous NiTi film deposited at T_S = 623 K) to metallic regime (in case of crystalline films deposited at T_S = 723, 823 and 923 K). NiTi films deposited at 723 K exhibited metallic like behavior without any indication of phase transformation in between martensitic and austenitic phases (**Figure 3.7 (b)**). The suppression of phase transformation phenomenon could be due to the very small grain size causing higher number of grain boundary interfaces and associated excess free volume as shown in inset of **figure 3.1**. As the constraints imposed by the grain boundaries on the growth of martensite confined the transformed volume fraction in the nano grained structures and hence could lead to suppression of martensitic transformation in nanocrystalline NiTi thin films. **Figure 3.8 (b)** shows TCR versus temperature plot of the film deposited at T_s of 723 K. An abrupt behavior of TCR was observed in the temperature range from 266 to 400 K during subsequent heating and cooling cycles, which clearly shows incomplete phase transformation due to constraints imposed by grain boundaries.

Figure 3.7 (c) shows R-T plot of NiTi thin film deposited at 823 K that clearly indicates the phase transformation from martensite to austenite phase and vice versa via R-phase during subsequent heating and cooling cycles. A linear decrease in electrical resistance with temperature was observed during cooling from 400 K because of the decreasing intensity of electron-photon interactions. At temperature R_s (318 K), the austenite phase is distorted and starts to transform to R-phase. The formation of R-phase during phase transformations could be attributed to the fact that in small grains, the constraints of grain boundaries exhibited significantly small shape strain (~1 %) during transformation from austenitic to R-phase as compared to 10 % in case of austenitic to martensitic phase **(24)**. The decrease in strain by twinning plays an important role in R-phase formation because it proceeds by nucleation and growth in parent phase in a heterogeneous manner. Therefore, R-phase formation is a self accommodation process, which occurs gradually in the parent phase with the decrease of temperature. Electron scattering by

lattice imperfection become pronounced as compared to the electron scattering by phonon with decrease in temperature below 318 K. This is because of increased density of twinned structure that results in the increase of electrical resistance. The cooling of the sample below R_f (304 K) promotes R-phase to martensite transformation, which exhibit less lattice distortion with no additional twinning. The electrical resistance was observed to decrease below temperature R_f **(figure 3.7 (c))** which may be due to less electron scattering by lattice distortion. Martensite transformation gets complete below the temperature M_f. During the heating cycle, the electrical resistance almost follows the same trend as obtained during cooling. Detwinning in this film commenced as the temperature increases to austenite start temperature (A_s). R-phase to austenite transformation is completed at temperature A_f (320 K) and NiTi microstructure completely reverses to the single cubic austenite microstructure. R-T curves showed that in small grained NiTi film, transformation processes take place according to the following procedures:

Martensite ↔ R-phase ↔ austenite (during heating and cooling)

The values of M_s (martensite start temperature) and A_f (austenite finish temperature) were found to be 304 and 320 K for the film deposited at T_S of 823 K.

Figure 3.8 (c) display the thermal coefficient of resistance versus temperature plot of the film deposited at T_S of 823 K for subsequent heating and cooling cycles. During heating cycle initially, a linear decrease in TCR value was observed with increasing temperature and thereafter a sharp decrease was observed with a transition from positive to negative value at 310 K. The TCR value remained negative in the temperature range of 310–338 K with a peak at 318 K. The observed continuous and sharp changes from positive to negative value of TCR could be due to the fast growth of R-phase because the TCR is found to be negative in R-phase. With further increase in temperature above 330 K, the TCR again become positive, which indicates R-phase to austenite parent phase transformation. Similar behavior of TCR was observed during cooling cycle. Therefore the observed variation in TCR as a function of temperature confirmed martensite ↔ R-phase ↔ austenite phase transformations during heating and cooling cycles.

Figure 3.7 (d) shows the electrical resistance response of the NiTi film deposited at 923 K. The behaviour of the R-T curves were found to be similar with the observed for the film deposited at 823 K except that the martensite start temperature (316 K) and austenitic final temperature (341 K) were found to be shifted towards higher temperature range. This could be due to the dominance of martensitic phase at room temperature. TCR versus temperature curves exhibited positive to negative transition and vice versa for subsequent cooling and heating cycles as showed in **figure 3.8 (d)**. A remarkable difference was observed in the peak value of TCR i.e. -1.5 X 10^{-4} and -2.7 X 10^{-5} during cooling and heating cycles, respectively. The low peak value and slope of TCR curve during heating cycle indicated the suppression of R-phase that could be due to the presence of martensite and R-phase in the matrix at 334 K.

3.1.3.3   Mechanical properties

Figure 3.9 shows the load-displacement curve for the films deposited at 823 and 923 K. Hardness, reduced modulus, indent depth recovery ratio, dissipation energy and wear behavior of the films deposited at T_s of 823 and 923 K have been evaluated by using load-displacement curves in order to reveal the qualitative behavior for the two crystallographic states. **Figure 3.10** shows the variation of hardness with contact depth for both samples. The average hardness of NiTi films exhibited austenite phase (deposited at T_S = 823 K) and dominant martensite phase (deposited at T_S = 923 K) at room temperature was observed 7.3 ± 0.6 and 4.8 ± 0.8 respectively, beyond a contact depth of ~70 nm. The hardness value showed that the austenite phase has more hardness as compared to that of martensite phase.

The indentation induced super elasticity effect can be characterized by the depth recovery ratio from the load versus depth curves by using the following equation **(14)**:

$$Depth\ recovery\ ratio\ = \frac{h_{max} - h_r}{h_{max}} \qquad (3.2)$$

Where h_{max} is the penetration depth at the maximum load and h_r is the residual depth
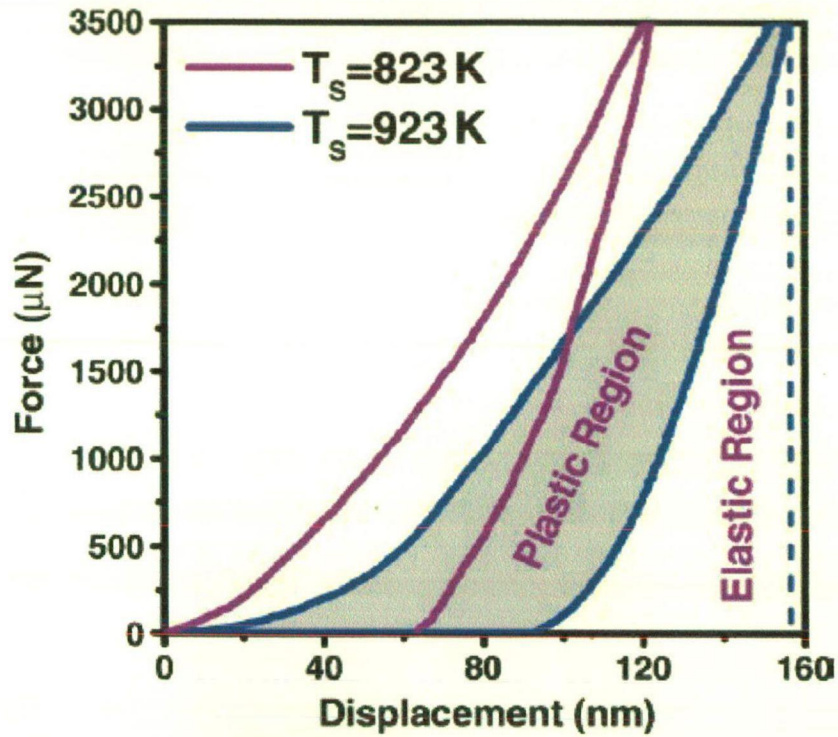
Figure 3.9 Load-displacement curve of NiTi films deposited at T_s of 823 and 923 K.
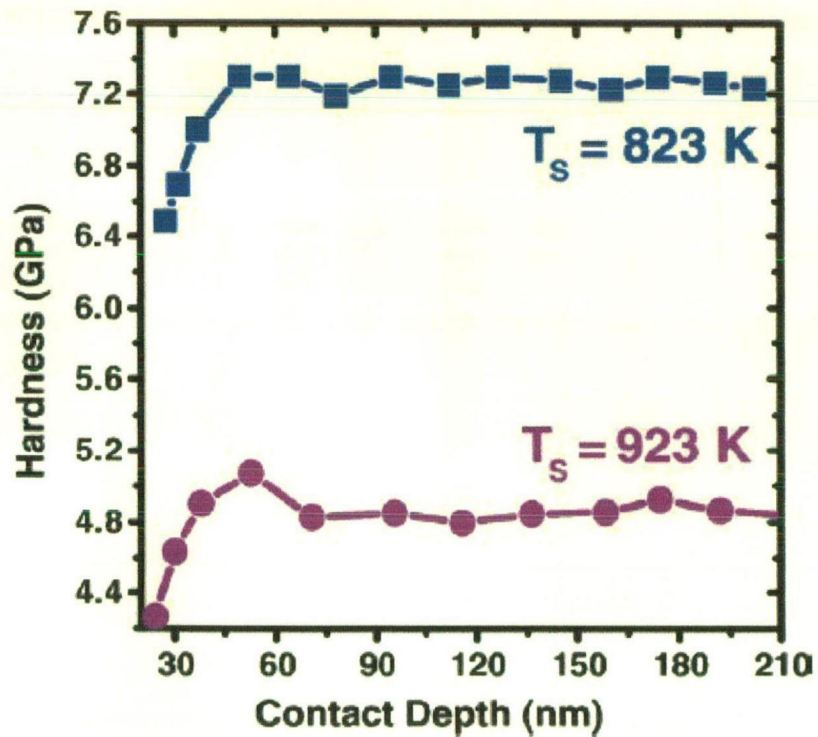
Figure 3.10   Hardness versus contact depth curves of NiTi films deposited at T_s of 823 and 923 K.

65

when the load returns to zero during unloading. The depth recovery ratio of the films deposited at T_S of 823 and 923 K was found to be 0.48 and 0.40, respectively. Lower depth recovery ratio (0.4) was observed for the film deposited at T_S of 923 K. This could be due to the dominance of martensite phase at room temperature that deformed easily by the reorientation of the martensite variants.

The dissipation energy (W_D) was evaluated from numerical integration of the area between the loading and unloading curves caused by dislocation movement, martensite transformation and martensite reorientation (25, 26). Dissipation energy of film exhibited martensite state at room temperature was found to be more as compared to the film showed austenite state that could also be due to the easy deformation of martensitic phase than that of austenite phase (figure 3.11).

The average hardness (H) and reduced elastic modulus (E_r) were calculated for both samples from indentation load versus depth curves. Hardness (H) to Young
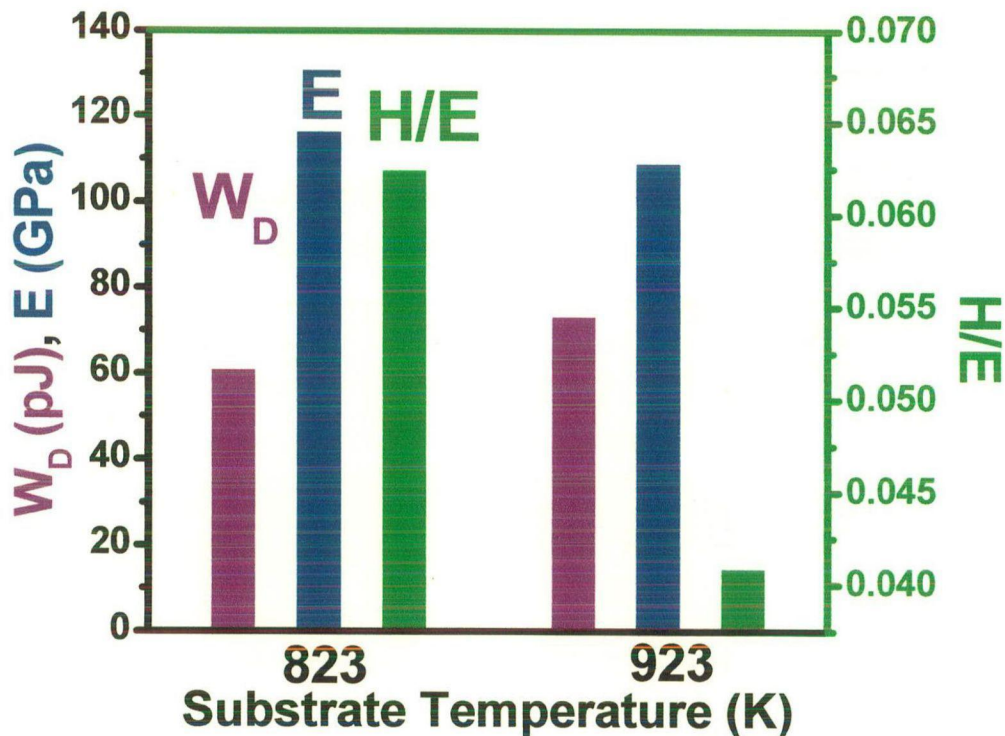
Figure 3.11   Dissipation energy (W_D), reduced modulus (E_r) and hardness to reduced modulus ratio (H/E) of NiTi films deposited at T_s of 823 and 923 K.

modulus (E) ratio has been proposed as the key factor to measure the behavior of wear resistance of the thin film coatings. It has been reported that the deformation around the indenter surface exhibit piling-up and sinking-in and the tendency of sinking-in increases with increasing H/E ratio (27). **Figure 3.11** shows the plot of H/E ratio of NiTi films deposited at 823 and 923 K. A relative low value of H/E ratio (0.04) for NiTi film exhibited martensite phase at room temperature indicated that more fraction of work is consumed in plastic deformation and large plastic strain is expected when contacting a material. Higher value of H/E ratio in case of the film exhibited austenite phase at room temperature is expected to have smaller accumulative strain and strain energy results relatively better wear resistance.

3.1.4 Conclusion

NiTi thin films were grown on Si (100) substrate by dc magnetron sputtering in the temperature range from room temperature to 923 K. Substrate temperature was found to have a great impact on surface morphology, crystallite size, mechanical properties and phase transformation behaviour of these films. XRD pattern showed that the film deposited at T_s of 623 K was amorphous in nature while the film deposited at 723 and 823 K exhibited the reflection from (110) plane of the austenite phase. With further increase in deposition temperature to 923 K, reflection from (-111), (002) and (110) planes of martensite structure was observed. Surface morphology of these films were found to change from non facet grains to facet grains with preferential in-plane orientation (martensite plates) with change in substrate temperature from 823 to 923 K. The NiTi film deposited at substrate temperature (T_S) of $\leq$ 623 K exhibited negative TCR value and non-metallic behavior while the film deposited at T_S of $\geq$ 723 K showed metallic behaviour. Electrical resistance versus temperature curves conformed that in a volume containing many small grains, the ability of phase transformation due to autocatalytic nucleation decreases with increase in grain boundary area. Nanoindentation studies revealed relatively low surface roughness, high hardness, high reduced elastic modulus and better wear behaviour for the film exhibited austenitic structure at room temperature in comparison to that exhibited martensitic structure.

3.2 Influence of film thickness on phase transformation behavior of sputtered NiTi thin films

3.2.1 Introduction

The present study elucidates the influence of film thickness on surface morphology and phase transformation behavior of NiTi thin films in order to clarify the role of special constraints introduced by substrate and film interface. It was observed that the film with small thickness (~100 nm) exhibited no austenite to martensite phase transformation and showed non metallic behavior with negative temperature coefficient of resistance (TCR) value. Also, shape memory behavior in the films with higher thickness (~3.5 μm) seems to be lost. NiTi films of thickness 300 nm-2.3 μm exhibited that austenite to martensite phase transformations involving the formation of an intermediate rhombohedral (R) phase during subsequent heating and cooling cycles. The austenite ⇔ R-phase transformation exhibits small temperature hysteresis as compared to austenite ⇔ martensite phase transformation, which is very important for actuator applications (28). The R phase presents other attractive features like stability against thermal cycling and a negligible strain-recovery fatigue, although the associated strain in austenite ⇔ R-phase is smaller (0.5%–1%) as compared to austenite ⇔ martensite phase transformation (6.5%-8.5%) (29).

3.2.2 Experimental details

NiTi films of various thickness were deposited on (100) silicon substrate by dc magnetron co-sputtering system at the substrate temperature of 823 K. The thickness of these films was controlled by varying the deposition time. Experimental procedure are given in **section 3.1.2**. Deposition parameters are listed in **table 3.4**.

The orientation and crystallinity of the films were studied using a Bruker advanced diffractrometer of CuKα (1.54Å) radiations in θ-2θ geometry at a scan speed of 1°/min. To make sure of absolute values of the 2θ diffraction angles, the diffractrometer was calibrated with respect to the peak position of Si calibration standard. A polycrystalline powder was used for instrumental correction. The surface morphology and grain size distribution were studied using atomic force microscope.

Table 3.4   Sputtering parameters for NiTi films.

Sputtering Parameters for	NiTi
Target	Ti, Ni
Base pressure	$\leq 2 \times 10^{-6}$ Torr
Gas Used	Ar
Sputtering pressure	10 mTorr
Deposition time	5-60 min
Sputtering power for Ti target	120 W
Sputtering power for Ni target	40 W
Substrate	Silicon(100)
Substrate Temperature	823 K
Substrate to Target Distance	5 cm

The resistance of the films was measured by four probe resistivity method using a liquid nitrogen cryocooler and Keithley instruments over a temperature range from 100 to 400 K. The contacts over the samples were made by silver paint.

3.2.3   Results and discussion

3.2.3.1   Structural properties

Figure 3.12 shows the XRD pattern of sputtered NiTi thin films of different thickness. XRD pattern showed the reflection from (110) plane of the austenite parent phase structure (**figure 3.12 (a)**) for all samples and additionally the reflection from the (211) plane of austenite parent phase (**figure 3.12 (b)**) for the samples with thickness $\geq$ 2.3 μm. The growth along (110) plane from the beginning could be due to the fact that most of the body centered cubic metals exhibit lowest surface energy corresponding to (110) plane, therefore, due to surface energy minimization, (110) texture should be favorable in bcc structures. The growth along the (211) plane initiated as the thickness of the sample reached up to 2.3 μm and the intensity of (211) reflection was found to increase with increase in film thickness as shown in **figure 3.13 (a)**. The possible reason could be the competition between minimum
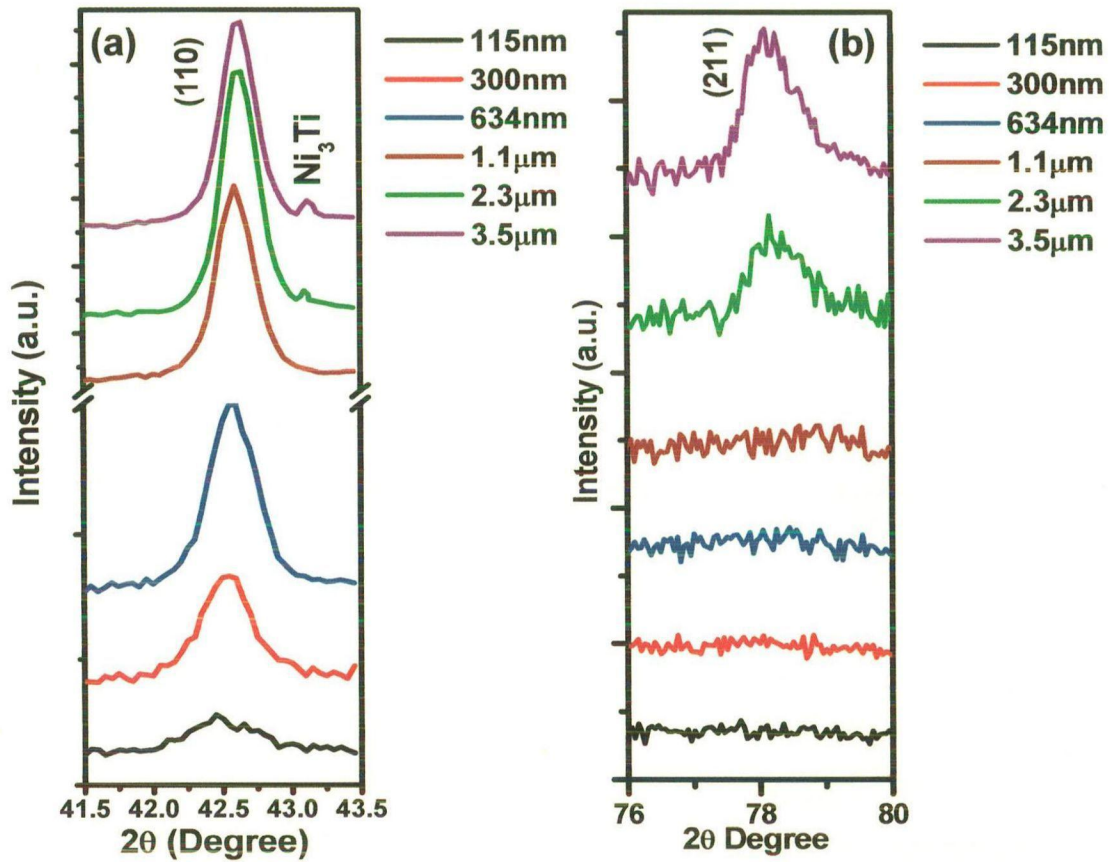
Figure 3.12   XRD pattern of NiTi films of various thickness **(a)** austenitic (110) reflection and **(b)** austenitic (211) reflection.
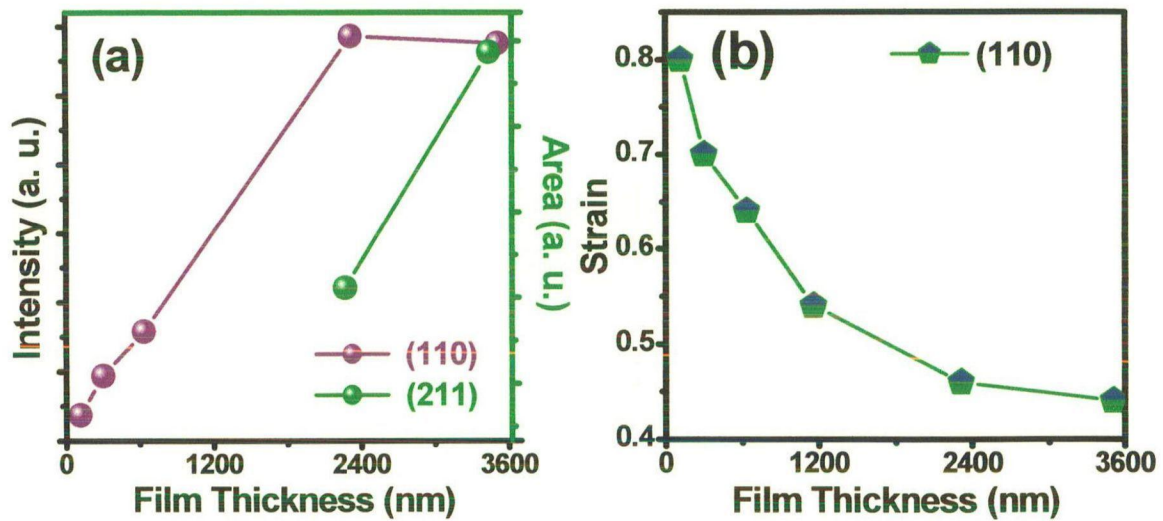
Figure 3.13   **(a)** Peak intensity of austenitic (110) and (211) reflections versus film thickness and **(b)** strain versus film thickness.

surface energy and strain energy. The growth along austenite (110) plane with minimum surface energy was observed when the surface energy is dominant driving force for structure formation and the growth along austenite (211) plane with lowest strain energy was observed when the strain energy is dominant. The strain of these film along austenite (110) peak position was calculated, which was also found to be decrease with increase in film thickness as shown in figure 3.13 (b). XRD pattern of 2.3 and 3.5 μm thick film exhibited reflection at $2\theta = 43.1°$, which suggest the formation of Ni_3Ti precipitates. The precipitate formation could be due to longer deposition time as it is reported that precipitate formation, transformation temperatures and superplasticity of NiTi films are sensitive to the deposition temperature, annealing temperature and duration (16, 17).

The lattice parameter of these films were calculated using lattice constant 'd'. Figure 3.14 shows variation of lattice parameter with thickness calculated along (110) and (211) peak positions. The decrease in lattice parameter was observed with increase in film thickness, which suggests that initially, the film experience compressive stress, which is significantly relaxed with increasing film thickness. The crystallite size of these films was calculated from the integral width of the diffraction
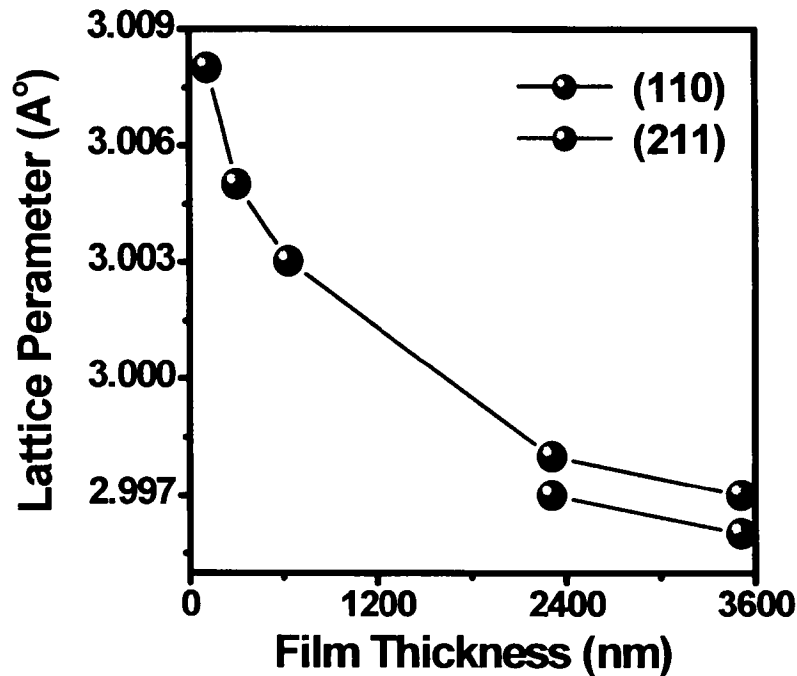
Figure 3.14   Lattice parameter versus film thickness.

Table 3.5   Various parameters of NiTi films of different thickness.

S. No	Film Thickness	Grain Size (nm)		Avg. Roughness (nm)	EDAX At. wt. % Ti : Ni
		XRD along (110) Peak	AFM		
1.	115 nm	15.7	14.7	3.41	49.9 : 50.1
2.	300 nm	24.5	29.8	5.63	50.1 : 49.9
3.	634 nm	26.2	38.1	8.82	50.2 : 49.8
4.	1.1 μm	39.2	57.2	14.74	50.1 : 49.9
5.	2.3 μm	56.1	98.5	22.83	49.1:50.9
6.	3.5 μm	63.3	150.0	30.58	48.6:51.4

lines using the Scherrer's equation **(15)** after background subtraction and correction of instrumental broadening. Estimated average crystallite size was found to be 15.7, 24.5, 26.2, 39.2, 56.1 and 63.3 nm for the film with thickness 115 nm, 300 nm, 634 nm, 1.1 μm, 2.3 μm and 3.5 μm, respectively along the peak broadening of austenite (110) plane, while 23.2 and 32.0 nm for the film with thickness 2.3 μm, and 3.5 μm, respectively along the peak broadening of austenite (211) plane and are reported in **table 3.5**. The reason for the increase in grain size with increasing deposition time (film thickness) could be due to the fact that the mobility of sputtered adatoms is increased by surface heat causing accumulation of energetic sputtered particles.

Figure 3.15 (a-f) shows the 2D AFM micrographs of the film with thickness 115 nm, 300 nm, 634 nm, 1.1 μm, 2.3 μm and 3.5 μm, respectively. **Figure 3.16 (a)** shows the line profile of scanned area that exhibited the variation in height on the surface. Several line profile scans were taken at different positions in order to measure the average value of surface roughness. The average surface roughness was calculated using the following formula **(30)**:

$$R = \sqrt{\frac{1}{l} \int_0^l f(x)^2 dx}$$

(3.3)
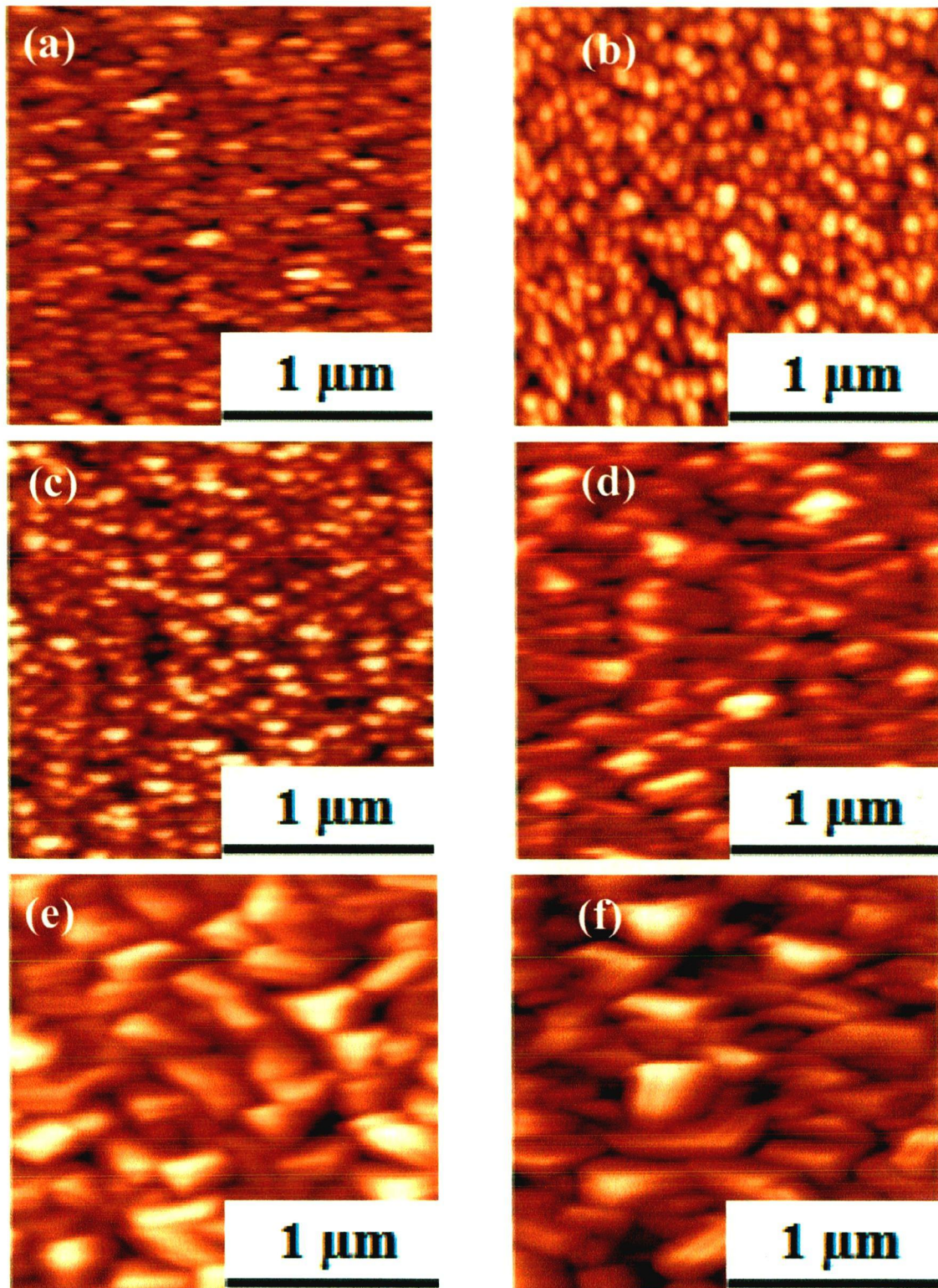
Figure 3.15   2D AFM images of NiTi films with thickness **(a)** 115 nm, **(b)** 300 nm, **(c)** 634 nm, **(d)** 1.1 μm, **(e)** 2.3 μm and **(f)** 3.5 μm.
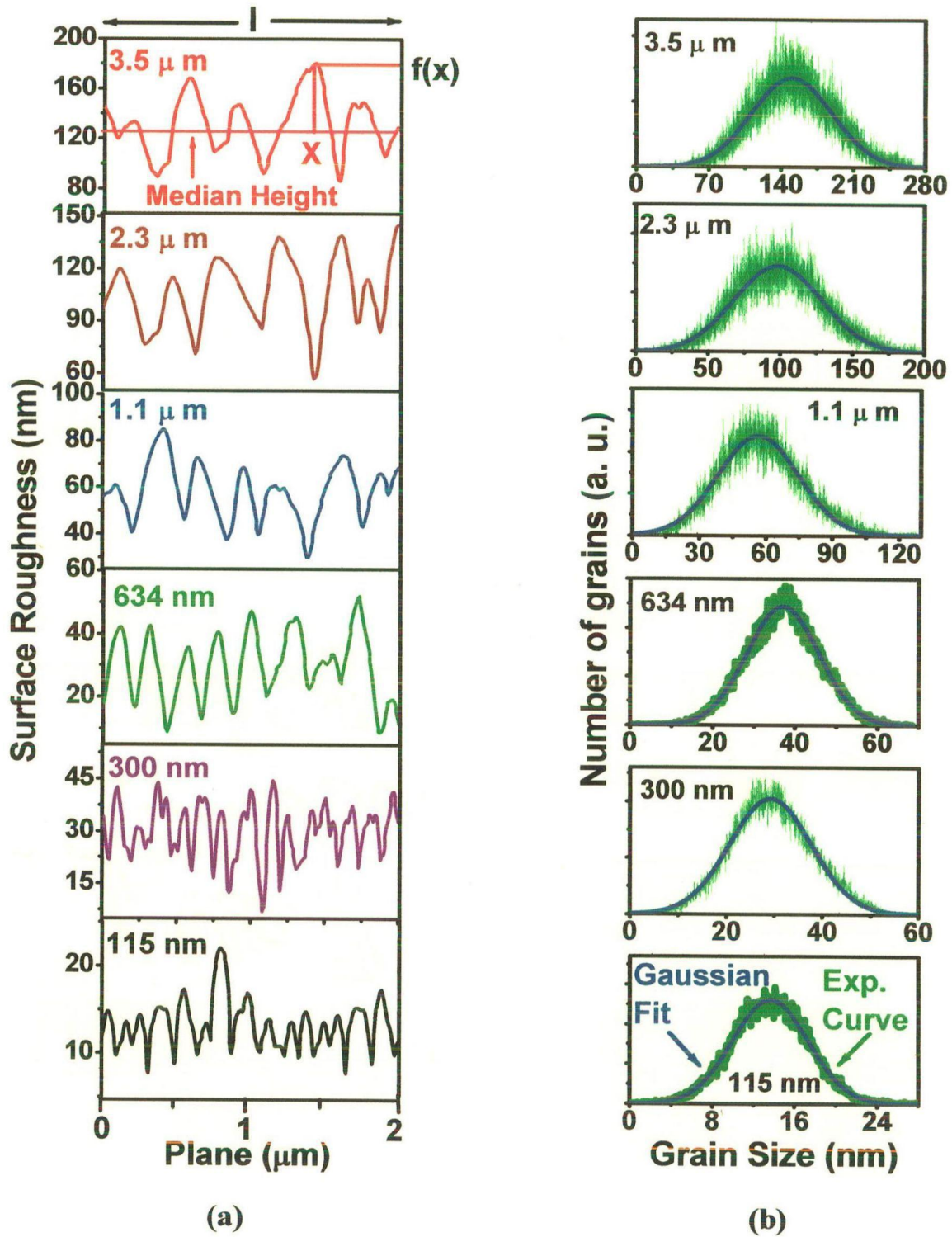
Figure 3.16 **(a)** Line profile images and **(b)** grain size distribution with Gaussian fit of NiTi films of various thicknesses.

Where R is the surface roughness in nm, l is the length of the line scan, x is the distance and $f(x)$ is the height relative to the median height. The average value of surface roughness was found to be 3.41, 5.63, 8.82, 14.74, 22.83 and 30.58 nm for the film of thickness 115 nm, 300 nm, 634 nm, 1.1 µm, 2.3 µm and 3.5 µm, respectively. Grain size distribution was determined using AFM micrographs. Several images were analyzed to ensure statistical reliability of the results. **Figure 3.16 (b)** shows the grain distribution on linear scale with the Gaussian fit, which suggests the Gaussian distribution of grains. According to the Gaussian fit the mean grain size was found to be increased with increasing film thickness, which is listed in **table 3.5**.

3.2.3.2 Electrical properties

Figure 3.17 (a) show the electrical resistance (ER) versus temperature curve of ~115 nm thick film during subsequent heating and cooling cycles. ER versus temperature curve exhibited non metallic behavior with negative temperature coefficient of resistance (TCR) value **(figure 3.17 (b))** and no R-phase to martensite transformation was observed that could be due to the higher resistance force as compared to driving force required for phase transformation. The resistance force could be generated due to the constraints imposed by the inter-diffusion of substrate and film and higher number of grains boundaries due to small grain size that hindered the autocatalytic formation of martensite phase.
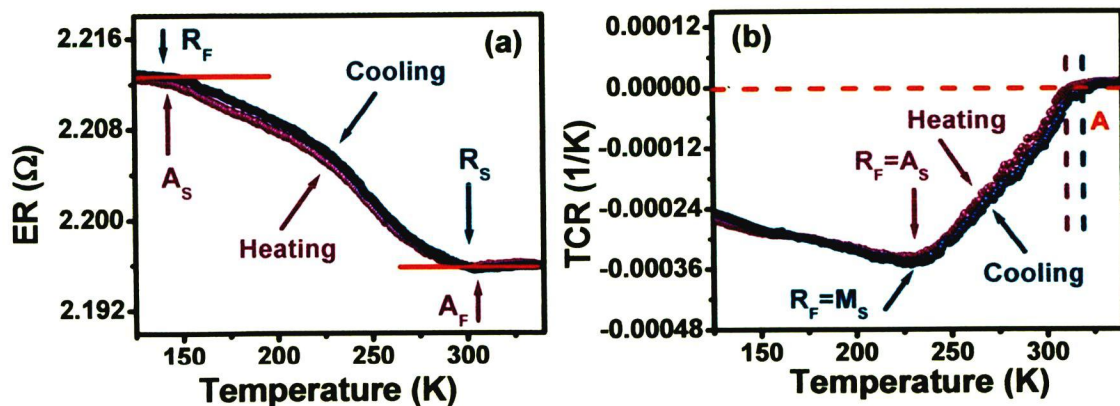
Figure 3.17 (a) Electrical resistance versus temperature curve and (b) TCR versus temperature curve of 115 nm thick NiTi film.

75

Figure 3.18 (a) shows the electrical resistance versus temperature curves for subsequent heating and cooling cycles for a ~300 nm thick film. During cooling cycle, R-phase transformation started at temperature R_s and the austenite parent phase began to transform to the twinned R-phase with the decrease in temperature below R_s. As the temperature reached to T1, R-phase transformation seized, which could be due to the resistance force (energy barriers) resulting from the constraints imposed by the inter-diffusion of film and substrate. If the driving force for R-phase transformation is less than the resistance force, the transformation process will vanish before full transformation of the austenite parent phase as shown in electrical resistance plateau produced in the temperature range T1 to T2, where T1 and T2 correspond to negative-to-zero and zero-to-negative slope changes, respectively. With further decrease in temperature from T2 to R_f, austenite to R-phase resumed again that could be due to the increase in driving force with the decrease in temperature, which overcome the resistance force. Further cooling below temperature R_f promoted R-phase to martensite phase transformation. During the heating cycle, electrical resistance was found to decrease with the increase in temperature from T3 to T4, where T3 and T4 correspond to the zero-slope points of the electrical resistance curve in this temperature range. Detwinning during heating from T3 to T4 is the reverse process of the twinning encountered during cooling from T2 to R_f. Electrical resistance exhibited a linear dependence on temperature with further increase in temperature above T4 and detwinning commenced again as the temperature reached to A_s. ER versus temperature curve exhibited sharp decrease in electrical resistance with further heating of the sample above temperature A_s, which indicated the R-phase to parent austenite phase transformation. The microstructure completely reversed to the parent austenite phase as the sample was heated above austenite final temperature (A_f).

Figure 3.18 (b) and **(c)** shows the ER versus temperature curves of martensite ⇔ R-Phase and R-phase ⇔ austenite phase transformation of 300 nm thick film. Martensite ⇔ R-phase (M⇔R) transformation did not exhibit any significant hysteresis, which suggests less lattice distortion during Martensite to R-phase transformation and vice-versa. Also, Austenite ⇔ R-phase (A ⇔ R)
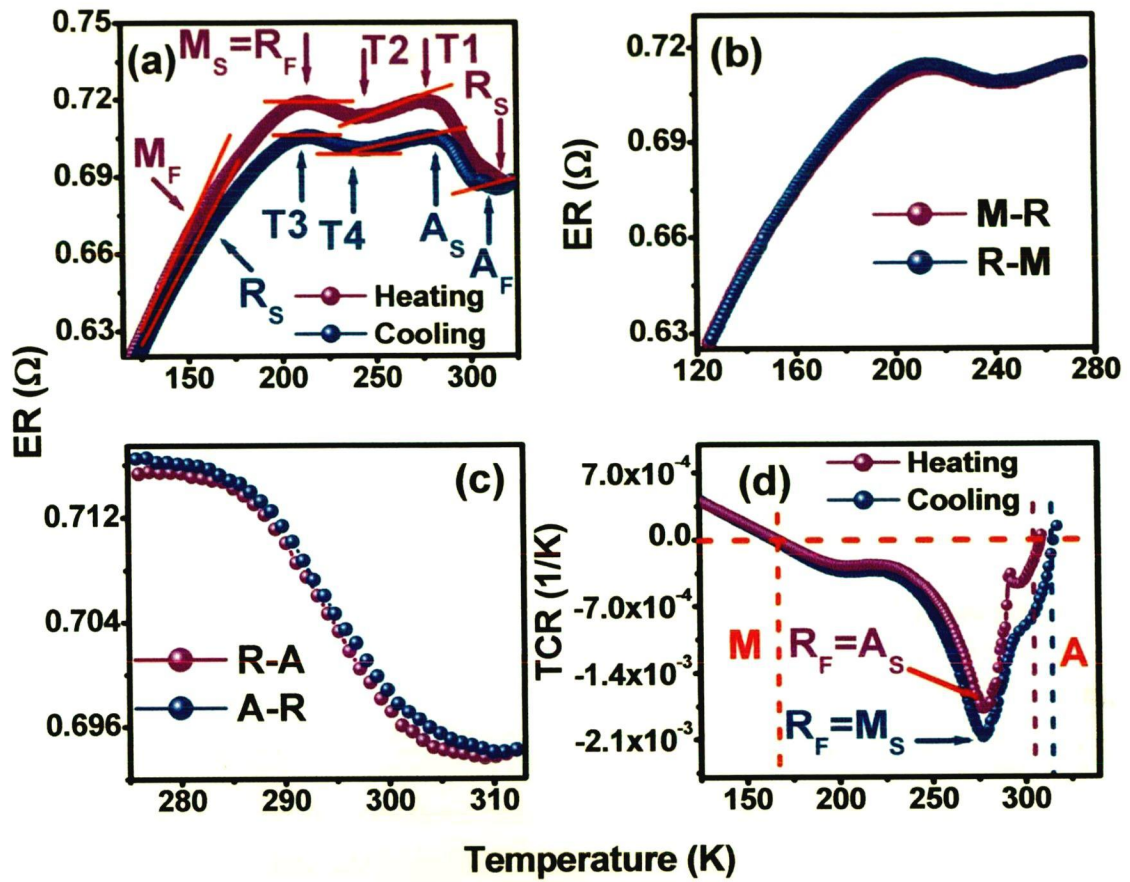
Figure 3.18 (a) ER versus temperature curve, **(b)** martensite ⇔ R-phase transformation, **(c)** Austenite ⇔ R-phase transformation, **(d)** TCR versus temperature curve of NiTi thin film with thickness of 300 nm.

Table 3.6 Details of transformation temperatures obtained from TCR versus temperature curves of NiTi films having different thickness.

S. No	Film Thickness	Transformation Temperature (K)					
		Heating			Cooling		
		R_s	$R_f = A_s$	A_f	R_s	$R_f = M_s$	M_f
1.	115 nm	--	231	312	322	230	--
2.	300 nm	167	278	308	312	276	164
3.	634 nm	238	286	318	321	286	228
4.	1.1 μm	264	296	318	314	287	223
5.	2.3 μm	256	223	178	263	221	172

transformation exhibited almost no hysteresis that could be due to the fact that R-phase is a self accommodation phase that occurs gradually in the parent phase with the decrease of the temperature also, lattice distortion and twinning are reversible process in R-phase to austenite phase transformations.

Figure 3.18 (d) shows the temperature coefficient of resistance versus temperature curve for the same film. The TCR value was found to be negative in the temperature range of 168–308 K and 168-312 K during subsequent heating and cooling cycles, respectively, which suggest the formation of R-phase because the TCR value remained negative in the R-phase. The value of the temperatures correspond to phase transformation were calculated using TCR versus temperature curves and these are listed in **table 3.6**.

Figure 3.19 (a) shows ER plot of ~634 nm thick NiTi film that clearly indicates the phase transformation from martensite to austenite phase and vice versa via R-phase during subsequent heating and cooling cycles. During the cooling cycle as the temperature lowered to R_s, the parent austenite phase begins to transform to R-phase. The phase change introduces lattice strain (~ 1%), which relaxed by the twinning. Twinning results in electron scattering that leads to the increase in electrical resistance. As the temperature reached to R_f, the R-phase transformation completed and further decrease in temperature promotes R-phase to martensite transformation. Martensite transformation ends when the temperature decreases to M_f and further cooling of sample below M_f does not involve phase change. During heating cycles, similar trend of ER curve was observed as in case of cooling cycle but the electrical resistance was found to be low that could be due to the small lattice distortion in temperature range from R_s to R_f as compared to that of M_s to M_f, which is also responsible for the hysteresis. Detwinning starts as the temperature reached to A_s and electrical resistance decreases rapidly with further increase in temperature. R-phase to austenite phase transformation completed at the temperature A_f and structure returned to the parent austenitic structure.

Martensite ⇔ R-phase and R-phase ⇔ austenite phase transformation is shown by **figure 3.19 (b)** and **(c)**, respectively during subsequent heating and cooling cycles. No significant hysteresis was observed during heating and cooling
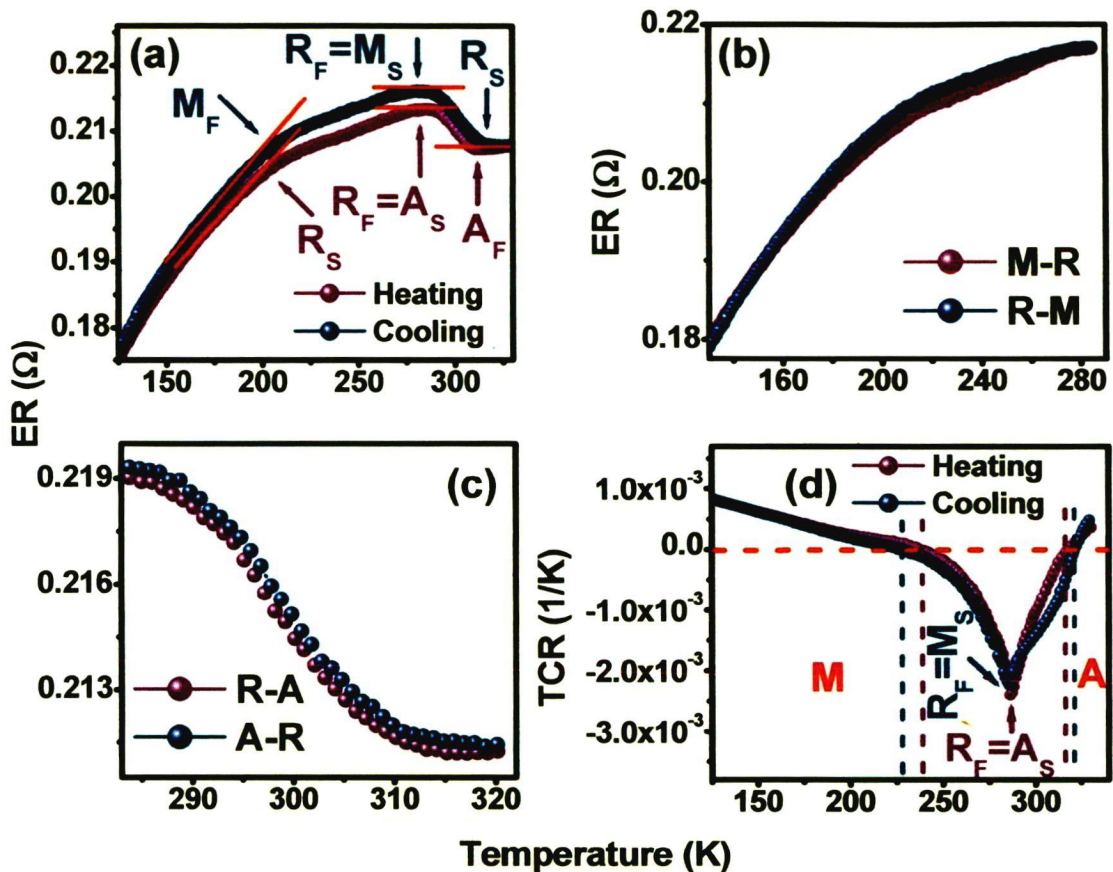
Figure 3.19 **(a)** ER versus temperature curve, **(b)** martensite ⇔ R-phase transformation, **(c)** Austenite ⇔ R-phase transformation, **(d)** TCR versus temperature curve of NiTi thin film with thickness of 634 nm.

cycles while martensite to R-phase transformation and vice versa, which suggest less lattice distortion during M⇔R phase transformation. Also, R-phase ⇔ austenitic phase transformation did not exhibit any significant hysteresis and the reason for same has been mentioned earlier. **Figure 3.19 (d)** shows TCR versus temperature curves for the same film that clearly indicates the martensite to austenite phase transformation via R-phase. During cooling cycle, transition in TCR value from positive to negative and negative to positive was observed at temperatures 318 and 238 K, respectively and it revealed austenite to R-phase and R-phase to martensite phase transformation. Similarly during heating cycle, transition from positive to negative and negative to positive was observed in TCR values at temperatures 224 and 321 K, respectively. Therefore, TCR versus temperature curves conform the R–
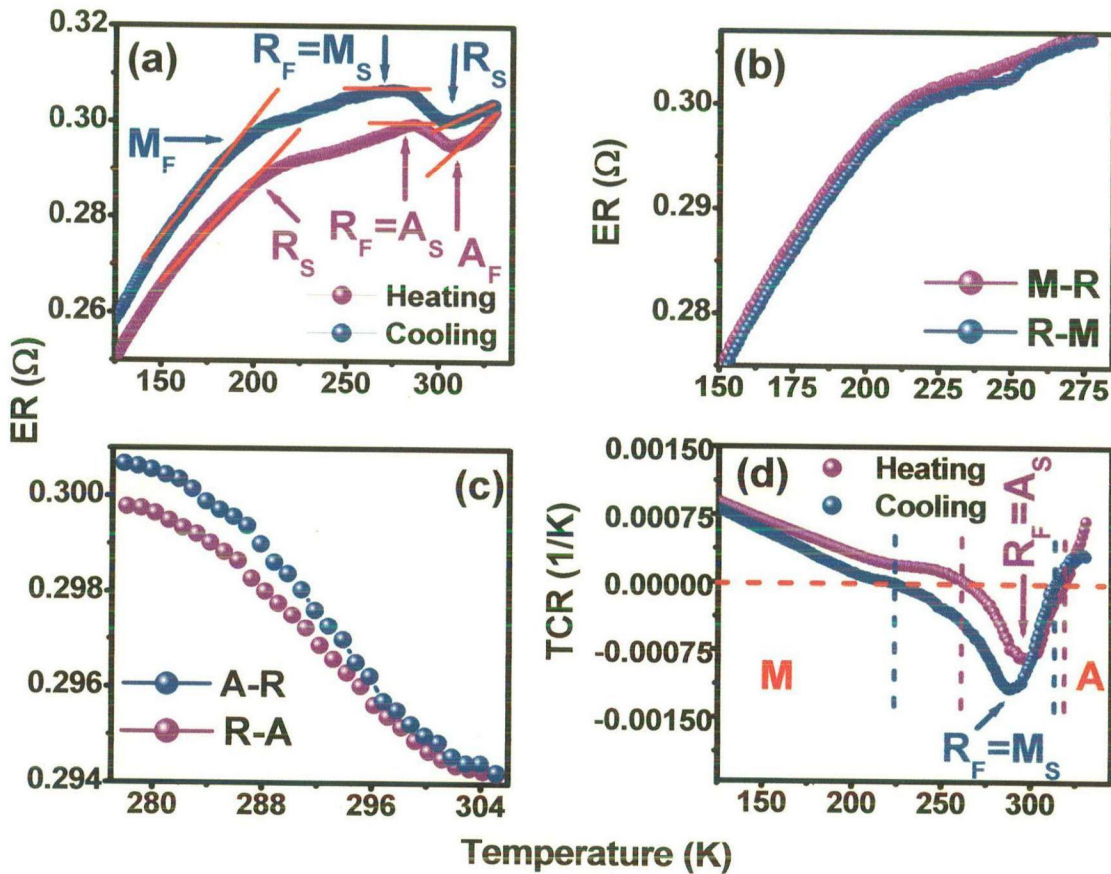
Figure 3.20 **(a)** ER versus temperature curve, **(b)** martensite $\Leftrightarrow$ R-phase transformation, **(c)** Austenite $\Leftrightarrow$ R-phase transformation, **(d)** TCR versus temperature curve of NiTi thin film with thickness of 1.1 μm.

phase formations during subsequent cooling and heating cycles. The M_s, M_f, R_s, R_f, A_s and A_f values were calculated using TCR versus temperature curve and are listed in **table 3.6**.

Figure 3.20 (a) shows the ER versus temperature curves of 1.1 μm thick film. Similar trend of electrical resistance was observed as in case of the film with thickness of 634 nm except that the hysteresis width was found to be larger for 1.1 μm thick film. A hysteresis was also observed in case of R-phase $\Leftrightarrow$ austenite phase transformation during heating and cooling cycles (**figure 3.20 (c)**) that could be due the presence of martensitic phase at temperature R_f. TCR versus temperature curve revealed the martensite to austenite phase transformation via R-phase during subsequent heating and cooling cycles as shown in **figure 3.20 (d)**.
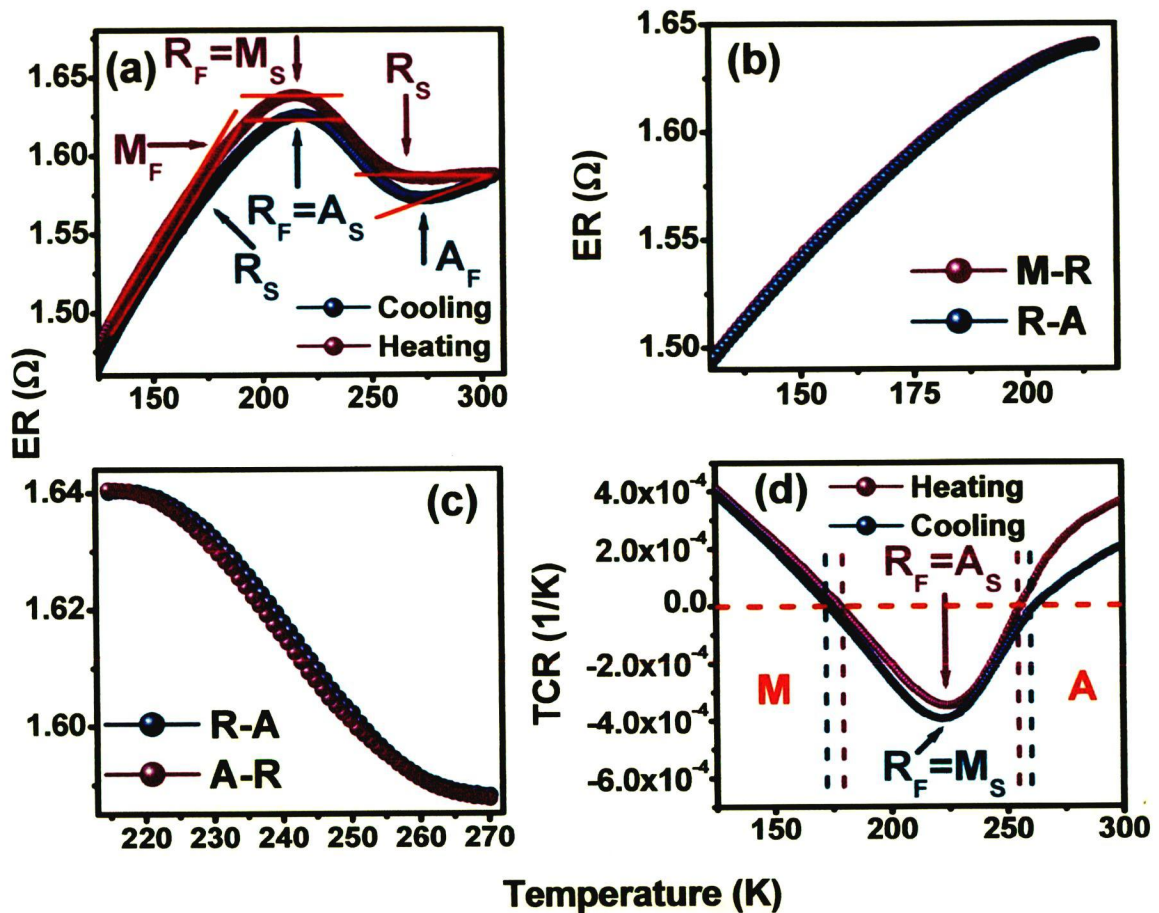
Figure 3.21   **(a)** ER versus temperature curve, **(b)** martensite ⇔ R-phase transformation, **(c)** Austenite ⇔ R-phase transformation, **(d)** TCR versus temperature curve of NiTi thin film with thickness of 2.3 µm.

Figure 3.21 (a) shows the ER versus temperature curve of 2.3 µm thick film for subsequent heating and cooling cycles. It was observed that transformation temperatures shifted towards lower temperature values that could be due the formation of Ni_3Ti precipitates. Martensite ⇔ R-phase and R-phase ⇔ austenite phase transformation did not exhibited any significant hysteresis during heating and cooling cycles as shown in **figure 3.21 (b)** and **(c)**. **Figure 3.21 (d)** shows the TCR versus temperature curve for the same film. TCR curve suggests the formation of R-phase during martensite ⇔ austenite phase transformations.
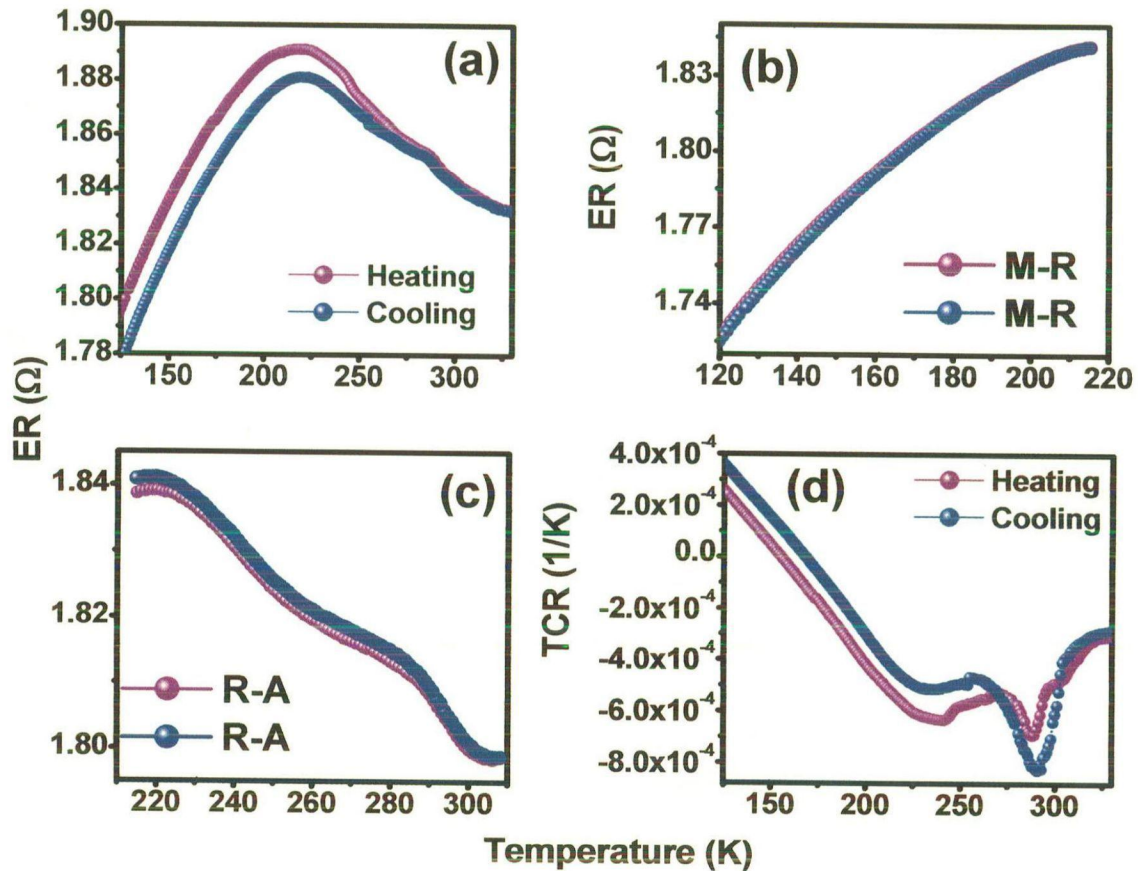
Figure 3.22 **(a)** ER versus temperature curve, **(b)** martensite ⇔ R-phase transformation, **(c)** Austenite ⇔ R-phase transformation, **(d)** TCR versus temperature curve of NiTi thin film with thickness of 3.5 μm.

Figure 3.22 (a) shows the ER versus temperature curve of 3.5 μm thick film that did not exhibit a clear behavior, only a peak was observed during heating and cooling cycles at temperature of ~ 216 K. Shape memory behavior seem to be lost in the same film that could be due to increased fraction of Ni₃Ti precipitates.

3.2.4 Conclusion

The influence of film thickness in sputtered NiTi thin films was investigated. XRD results revealed the presence of austenitic (110) reflection from the beginning that could be due to the minimum surface energy of (110) plane in bcc structures. Reflection from austenitic (211) plane was also observed in the films of higher thickness (≥ 2.3 μm) because of strain energy minimization with increasing

thickness. Ni_3Ti precipitate formation was initiated as the film thickness reached to 2.3 μm and the fraction of precipitate formation increased with increasing thickness. AFM results indicated that even with increasing the film thickness, grains follows the Gaussian distribution. Electrical resistance versus temperature curves exhibited that the film with thickness ≤ 300 nm experiences resistance force due to film and substrate inter-diffusion and small grain size, which affects the phase transformation behavior in these films. The films with thickness 634 nm and 1.1 μm showed the martensite ⇔ austenite phase transformation via R-phase, which are the suitable candidates for actuators application because austenite to R-phase transformation exhibit small hysteresis and strain than that of austenite to martensite transformation. The 2.3 μm thick films displayed the phase transformation behavior with shift in transformation temperatures towards lower temperature values because of the Ni_3Ti precipitate formation and the film of 3.5 μm thickness showed suppression of shape memory behavior that could be due to the increased fraction of precipitate formation.
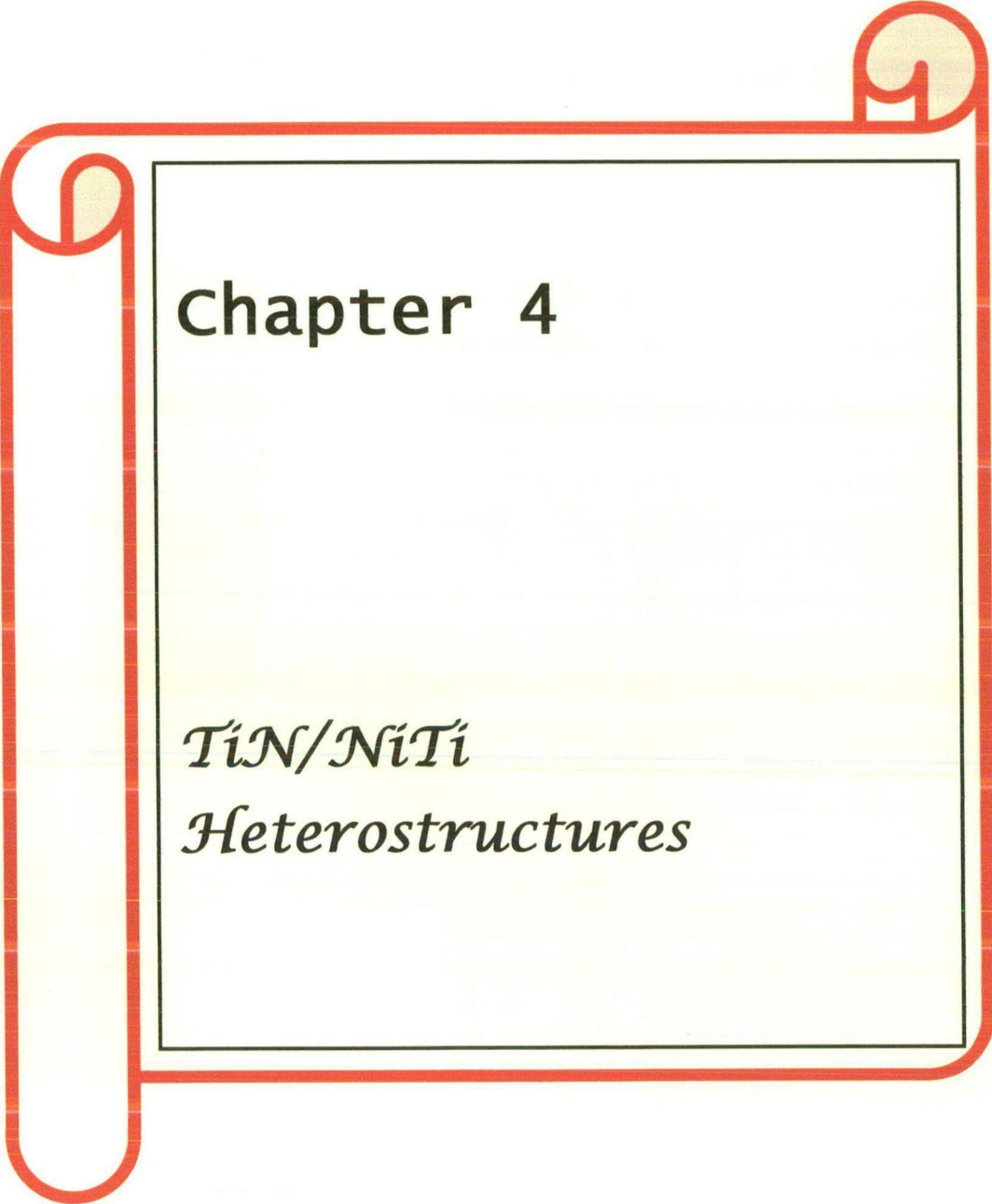
3.3 References

(1) Xu X. and Thadhani N., "Shock synthesis and characterization of ultrafine grained NiTi shape memory alloy", Scripta Materialia, 44, 2477-2483 (2001).

(2) Valiev R. Z., "The new trends in fabrication of bulk nanostructured materials by SPD processing", Journal of Materials Science, 42, 1483-1490 (2007).

(3) Gill J. J., Chang D. T., Momoda L. A. and Carman G. P., "Manufacturing issues of thin film NiTi microwrapper", Sensors and Actuators, A: Physical, 93, 148-156 (2001).

(4) Humbeeck J. V., "Shape memory alloys: A material and a technology", Advanced Engineering Materials, 3, 837-850 (2001).

(5) Gong F. F., Shen H. M. and Wang Y. N., "Fabrication and characterization of sputtered Ni-rich NiTi thin films", Materials Letters, 25, 13-16 (1995).

(6) Humbeek J. V., "Non-medical applications of shape memory alloys", Materials Science and Engineering A, 273-295, 134-148 (1999).

(7) Ishida A. and Martynov V., "Sputter-deposited shape-memory alloy thin films: Properties and applications", MRS Bulletin, 27, 111-114 (2002).

(8) Pan Q. and Cho C., "The Investigation of a Shape Memory Alloy Micro-Damper for MEMS Applications", Sensors, 7, 1887-1900 (2007).

(9) Gong F. F., Shen H. M. and Wang Y. N., "Structures and defects induced during annealing of sputtered near-equiatomic NiTi shape memory thin films", Applied Physics Letters, 69, 2656-2658 (1996).

(10) Yang Y. Q., Jia H. S., Zhang Z. F., Shen H. M., Hu A. and Wang Y. N., "Transformations in sputter-deposited thin films of NiTi shape memory alloy", Materials Letters, 22, 137-140 (1995).

(11) Busch J. D., Johnson A. D., Lee C. H. and Stevenson D. A., "Shape-memory properties in Ni-Ti sputter-deposited film", Journal of applied Physics, 68, 6224-6228 (1990).

(12) Gisser K. R. C., Busch J. D., Johnson A. D. and Ellis A. B., "Oriented nickel-titanium shape memory alloy films prepared by annealing during deposition", Applied Physics Letters, 61, 1632-1634 (1992).

(13) Wibowo E. and Kwok C. Y., "Fabrication and characterization of sputtered NiTi shape memory thin films", Journal of Micromechanics and Microengineering, 16, 101-108 (2006).

(14) Zhang Y., Cheng Y. T. and Grummon D. S., "Indentation stress dependence of the temperature range of microscopic superelastic behavior of nickel-titanium thin films", Journal of Applied Physics, 98, 1-4 (2005).

(15) B.D. Cullity, "Elements of X-ray Diffraction", Addison-Wesley, Reading, MA, 1970, p. 102.

(16) Fu Y., Du H., Huang W., Zhang S. and Hu M., "TiNi-based thin films in MEMS applications: A review", Sensors and Actuators, A: Physical, 112, 395-408 (2004).

(17) Lee H. J., Ni H., Wu D. T. and Ramirez A. G., "Experimental determination of kinetic parameters for crystallizing amorphous NiTi thin films", Applied Physics Letters, 87, 114102-114104 (2005)

(18) Fu Y. and Du H., "Effects of film composition and annealing on residual stress evolution for shape memory TiNi film", Materials Science and Engineering A, 342, 236-344 (2003).

(19) Murray J. L, "Phase Diagrams of Binary Titanium Alloys", ASM International Metals Park, (1987).

(20) Saburi T., Nenno S. and Tamura I., "Proceedings of the International Conference on Martensitic Transformations" The Japan Institute of Metals, Japan, p. 671 (1986).

(21) Banerjee R., Sperling E. A., Thompson G. B., Fraser H. L., Bose S., and Ayyub P., "Lattice expansion in nanocrystalline niobium thin films", Applied Physics Letters, 82, 4250-4252 (2003).

(22) Arranz M. A. and Riveiro J. M., "Shape memory effect in sputtered Ti-Ni thin films", Journal of Magnetism and Magnetic Materials, 290-291, 865-867 (2005).

(23) Pushin V. G. and Valiev R. Z., "The nanostructured TiNi shape-memory alloys: New properties and applications", Solid state phenomena, 94, 13-24 (2003).

(24) Waitz T., Kazykhanov V. and Karnthaler H. P., "Martensitic phase transformations in nanocrystalline NiTi studied by TEM", Acta Materialia, 52, 137-147 (2004).

(25) Komvopoulos K. and Ma X. G., "Pseudoelasticity of martensitic titanium-nickel shape-memory films studied by in situ heating nanoindentation and transmission electron microscopy", Applied Physics Letters, **87**, 1-3 (2005).

(26) Gall K., juntunen K., Maier H. J., Sehitoglu H. and Chumlyakov Y. I., "Instrumented micro-indentation of NiTi shape-memory alloys", Acta Materialia, **49**, 3205-3217 (2001).

(27) Ni W., Cheng Y. T., Lukitsch M. J., Weiner A. M., Lev L. C. and Grummon D. S., "Effects of the ratio of hardness to Young's modulus on the friction and wear behavior of bilayer coatings", Applied Physics Letters, **18**, 4028-4030 (2004).

(28) Sittner P., Landa M., Lukas P. and Novak V., "R-phase transformation phenomena in thermomechanically loaded NiTi polycrystals", Mech. Mater, **38**, 475-492 (2006).

(29) Uchil J., Mohanchandra K. P., Mahesh K. K. and Kumara K. G., "Thermal and electrical characterization of R-phase dependence on heat-treat temperature in Nitinol", Physica B, **253**, 83-89 (1998).

(30) Buenconsejo P. J. S., Ito K., Kim H. Y. and Miyazaki S., "High-strength Superelastic Ti-Ni Microtubes Fabricated by Sputter Deposition" Acta Materialia, **56**, 2063-2072 (2008).

Chapter 4

TiN/NiTi Heterostructures

CHAPTER 4

TiN/NiTi HETEROSTRUCTURES

4. Effect of crystallographic orientation of nanocrystalline TiN on TiN/NiTi heterostructures

4. Effect of crystallographic orientation of nanocrystalline TiN on TiN/NiTi heterostructures

4.1 Introduction

Nickel Titanium (NiTi) thin films have attracted much attention in recent years as intelligent and functional materials due to their unique properties i.e. superelasticity and shape memory effect, which enable them to be widely used in aerospace, micro-electromechanical systems (MEMS) and various biomedical applications (1-3). The phase transformation in SMA thin film is accompanied by significant changes in the mechanical, physical, electrical and optical properties, which could be made use in the design and fabrication of microsensors and micro-actuators. However, there are still some concerns for the wide application of SMA thin films because of their unsatisfactory mechanical and tribological performances, chemical resistance and biological reliability. High nickel content in NiTi alloys often stimulated suspicions for their medical use. The limited hardness and wear resistance of NiTi make it difficult to be used in orthodontic and MEMS applications. To apply NiTi surgical devices in the human body, the surface properties and corrosion resistance are important material characteristics. Therefore, proper passivation to prevent surface layer degradation and nickel releasing into the environment has been considered crucial for the medical applications of NiTi alloys.

Surface modification techniques such as nitrogen ion implantation (4), gas nitriding (5) have been employed to improve the surface properties of bulk NiTi alloys. The problems of these surface treatments are high cost, possible surface or ion induced damage, amorphous phase formation, or degradation of shape memory effects. Surface oxidation of NiTi bulk materials have also been reported to prevent the Ni ion release and improve its biocompatibility (6). However, this oxidation layer is too thin, fragile and easy to be removed (7). Therefore, there is a need to search for stable, corrosion resistant and biocompatible protective coating for biomedical and MEMS applications of NiTi based SMA thin films.

TiN is a well known material for its superior mechanical properties, excellent corrosion, wear resistance and good biocompatibility and TiN coatings are

often used to modify the orthopedic implant materials to extend their life span (8, 9). Thus, the present research explored the insitu deposition of hard and adherent nanocrystalline TiN protective coating of ~ 140 nm thickness on NiTi thin films by dc magnetron sputtering. The magnetron sputtering has important specific advantages such as low levels of impurities and easy control of the deposition rate, therefore, there are many reposts on deposition of nanocrystalline nitride thin films via magnetron sputtering (10, 11). The main aim of the present study is (i) to synthesize TiN/NiTi/Si thin films by dc magnetron sputtering for improvement of surface and mechanical properties of NiTi without sacrificing phase transformation and shape memory effect. Precise control of sputtering parameter was done to obtain high quality films; (ii) to study the effect of crystallographic orientation of TiN on structural, electrical and mechanical properties of TiN/NiTi heterostructure thin films. To accomplish this, TiN films were prepared under different gas environment and texture of the TiN films was found to change from (111) to (200) with change in nature of sputtering gas. The investigation revealed better surface and mechanical properties in case of TiN (200)/NiTi films as compared to NiTi and TiN (111)/NiTi films without sacrificing phase transformation effect.

4.2   Experimental details

Pure NiTi films and TiN/NiTi heterostructures were deposited on (100) silicon substrate of dimensions 1.5 x 2 cm^2 by dc magnetron sputtering system. The substrates were initially cleaned thoroughly in an ultrasonic bath with a mixture of distilled water and trichloroethylene in 4:1 ratio and then washed with boiled acetone. High purity (99.99%) titanium and nickel metal targets of 50 mm diameter and 3 mm thickness were used. Before every sputtering run, the targets were pre-sputtered for 5 min in order to ascertain the same state of the targets in every run. Suitable powers were applied to each target to give similar deposition rates of Ni and Ti. Substrate holder was rotated at 20 rpm in a horizontal plane to achieve a uniform film composition. Both magnetron guns were tilted at an angle of 45° so that the plasma from both the targets can be concentric. Before sputtering deposition, the chamber was evacuated to a base pressure of the order of 10^{-7} torr and then backfilled with argon to the desired pressure. The chamber pressure was measured

using a combination vacuum gauge (Pfeiffer Vacuum). All the NiTi films of approximately 2μm thickness were prepared at substrate temperature of 823 K in an argon (99.99% pure) atmosphere. The target to substrate distance was fixed at approximately 5 cm. No post-annealing was performed after deposition. For the deposition of TiN passivation layer, two different sputtering gas mixtures were used: 70% Ar + 30% N_2 (referred henceforth as Ar + N_2); and 100% N_2. The samples A, B and C correspond to the pure NiTi, TiN (111)/NiTi and TiN (200)/NiTi respectively. Sputtering parameters are summarized in **table 4.1**.

The orientation and crystallinity of the films were studied using a Bruker advanced diffractometer of CuKα (1.54Å) radiations in θ-2θ geometry at a scan speed of 1°/min. To obtain a profile fitting with good signal, a polycrystalline silicon powder was used for instrumental correction. The surface topography and microstructure of the films were studied using field emission scanning electron microscope (FEI Quanta 200F) and atomic force microscope in conjunction with nanoindenter. The microstructure was also investigated using high resolution transmission electron microscopy (HRTEM). The film thickness was measured using

Table 4.1   Sputtering parameters for TiN/NiTi heterostructures

Sputtering Parameters for	NiTi	TiN (111)	TiN (200)
Target	Ti, Ni	Ti	Ti
Base pressure	$\leq 2 \times 10^{-6}$ Torr	$\leq 2 \times 10^{-6}$ Torr	$\leq 2 \times 10^{-6}$ Torr
Gas Used	Ar	Ar+N_2 (70:30)	N_2
Sputtering pressure	10 mTorr	10 mTorr	10 mTorr
Deposition time	30 min	15 min	15 min
Sputtering power for Ti target	120 W	150 W	150 W
Sputtering power for Ni target	40 W	--	--
Substrate	Silicon(100)	NiTi/Si	NiTi/Si
Substrate Temperature	550 °C	550 °C	550 °C
Substrate to Target Distance	5 cm	5 cm	5 cm
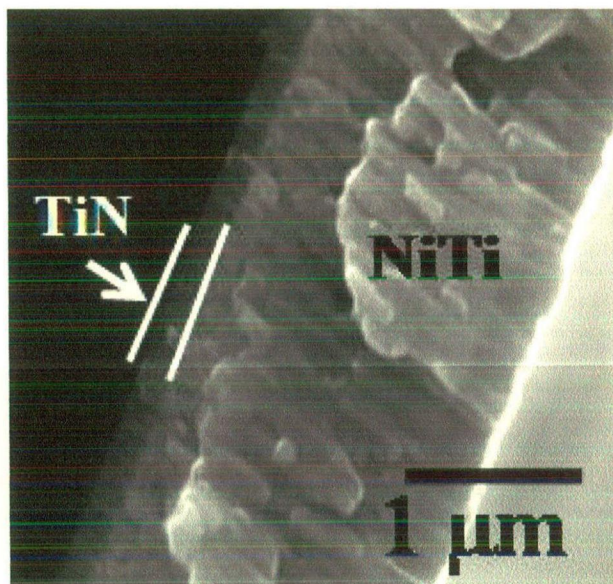
Figure 4.1   Cross sectional FESEM image of TiN/NiTi heterostructure.

a surface profilometer and cross sectional FESEM as shown in **figure 4.1**. The Ti/Ni ratio was determined as 50.8:49.2 from energy dispersive x-ray analysis (EDAX). The resistivity of the films was measured by four probe resistivity method using a liquid nitrogen cryocooler and Keithley instruments over a temperature range from 90 to 450 K. The contacts over the samples were made by silver paint.

TEM samples were prepared using ion milling method. Initially, the sample was cut into disc of 3mm diameter using ultrasonic cutter. Then the discs were manually thinned to approximately 0.085 mm from the substrate's side in a disc grinder using 40-50 μm grit papers. After the thinning process, the specimen was subjected to the dimple grinder, which is the last abrasive pre-thinning step. The dimpling procedure produces a thin central region in the disc. It was carried out until the central thickness approaches 0.015-0.02 mm. The sample must not be too thin or thick because the thin sample would be easily broken and the thick will extend the subsequent ion milling time. After dimpling procedure the sample was mounted on a specimen holder and polished using ion beam to generate an electron transparent area. Both the ion guns were tilted 5° from the top. As the perforation was observed, the voltage of the ion beams was reduced to a small level and the incident angle changed to 3° to enlarge the transparent area for TEM investigation.

A Hysitron Triboindenter was used to perform nanoindentation tests. Sixteen nanoindentation tests were performed on each sample using a diamond Berkovich indenter probe to determine the hardness and reduced modulus. Each test consisted of a five-second linear loading segment to a peak load, followed by a two-second holding segment at the peak load, and finally a five-second linear unloading segment. The testing temperatures were 298, 323 and 380 K. Topographical in-situ images were taken on the surface of each sample to determine surface roughness.

4.3   Results and discussion

4.3.1   Structural properties

Figure 4.2 shows the XRD pattern of thin film for samples A, B and C. XRD pattern of sample A exhibit dominant (110) reflection of austenite phase at $2\theta = 42.6°$. No traces of other phases like Ti_2Ni and Ni_4Ti_3 were observed in the pattern. In the case of sample B (with TiN films deposited under Ar + N_2 gas mixture), XRD curve exhibit strong (111) preferential orientation with no (200) reflection. On the other hand, XRD pattern of sample C (with TiN films deposited under 100% N_2 gas atmosphere), the most intense reflection of TiN was (200) with relatively no (111) reflection peak of TiN indicating a strong (200) texture **(Figure 4.2)**. The preferential orientation of TiN films is a TiN has lowest strain energy, while the (200) plane has the lowest surface energy **(12)**. The growing film develops a crystallographic structure with minimum total energy of the system. The nature of sputtering gas influences the rate of sputtering from the Ti target. It has been reported that Ar + N_2 gas mixture result in a metallic mode of sputtering, and use of pure N_2 as a sputtering gas is likely to result in a nitride mode of sputtering with a significant lower sputtering rate **(13)**. The achievement of a minimum surface energy configuration during film growth is largely determined by the adatom mobility on the substrate surface, which decreases with increase in sputtering rate. In case of sample B and C, the change of sputtering gas from Ar+ N_2 gas mixture to pure N_2 leads to an increase in the mobility of adatoms promoting closed packed structures in near thermodynamic equilibrium conditions. Thus, for high adatom mobility the TiN films are expected to grow along the (200) orientation corresponding to that with the
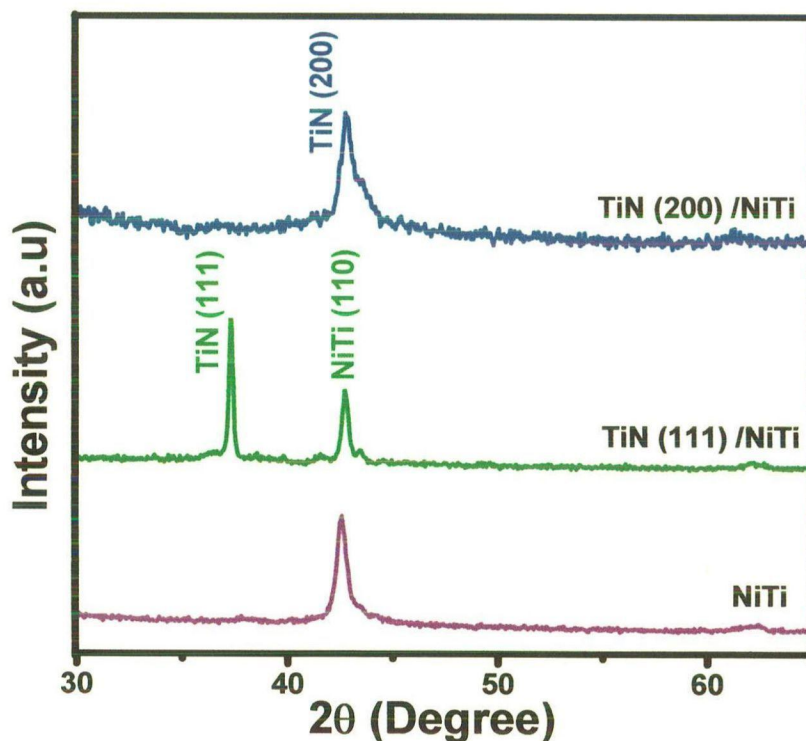
Figure 4.2   XRD pattern of NiTi film, TiN (111)/NiTi heterostructure (TiN deposited in (Ar + N₂) gas environment) and TiN (200)/NiTi heterostructure (TiN deposited in 100 % N₂ gas environment).

lowest surface free energy. On the other hand, for low adatom mobility the preferential orientation is (111) in which the highest number of atoms per unit area can be incorporated at low energy sites.

The surface morphology of pure NiTi film and TiN/NiTi films prepared in different gas environment is shown in **figure 4.3**. Pure NiTi film shows uniform, fine and homogenous microstructures with grain size of 96 nm (**Figure 4.3(a)**). The fineness of the microstructure depends on incompatibility between martensite invariant and austenite and is actually determined by a competition between the elastic energy stored in the transition layer and the interfacial energy on the twin boundaries between the variants. Small hysteresis width observed from resistivity measurement of sample A depicts the compatibility between martensite invariant and austenite, and hence confirm the fine microstructure of NiTi film. **Figure 4.3(b)** and **(c)** clearly show the change in grain morphology from strongly faceted pyramid like grains to non-faceted spherical grains in case of TiN /NiTi films, with change in
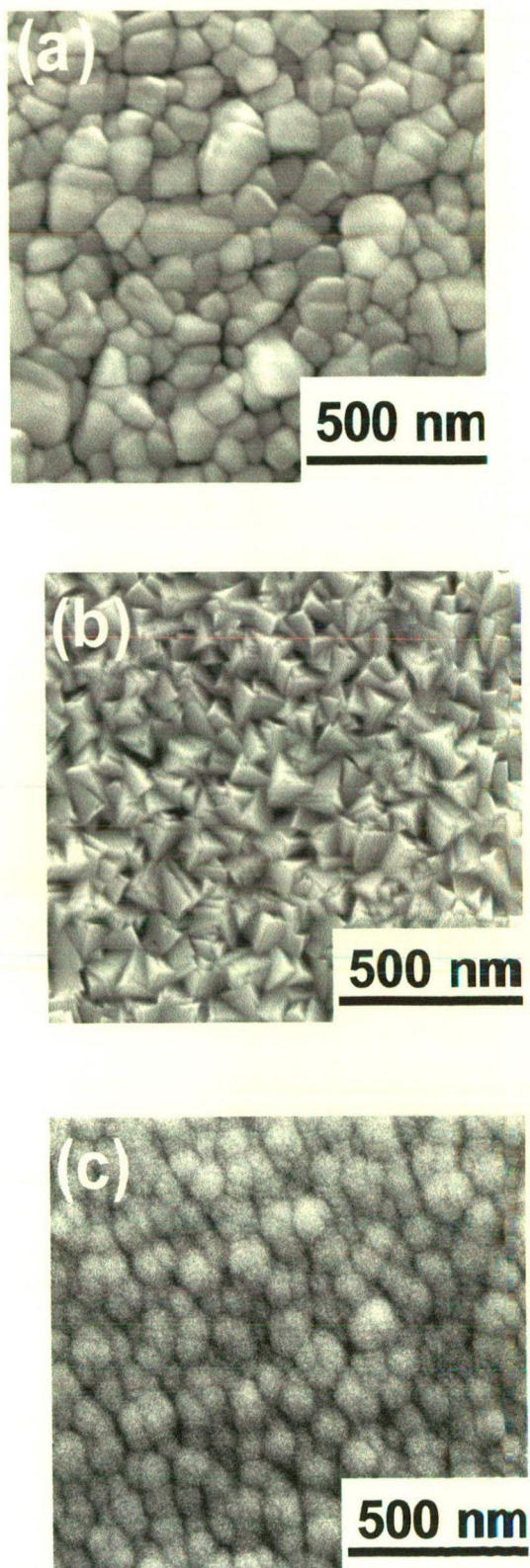
Figure 4.3   FESEM images of **(a)** NiTi film, **(b)** TiN (111)/NiTi and **(c)** TiN (200)/NiTi heterostructures.

crystallographic orientation of TiN from (111) to (200). Moreover the sample B deposited in (Ar + N_2) gas atmosphere with (111) orientation showed larger grain size of 84 nm in comparison to the sample C deposited in pure N_2 gas atmosphere with preferred (200) orientation and with estimated grain size of 56 nm. The difference in grain size under different sputtering conditions can be explained from the relationship of the mean free path, λ (cm) and molecular diameter of the sputtering gas using following expression:

$$\lambda = 2.330 X 10^{-20} \frac{T}{(P\delta_m^2)}$$

(4.1)

Where T (K) is the temperature, P (Torr) is the pressure and δ_m (cm) is the molecular diameter **(14)**. According to the above equation, the grain size must be large in the case of argon–nitrogen gas mixture as atomic diameter of argon is larger of 1.76 Å. Thus, the sputtered atoms undergo large number of collisions in case of (Ar + N_2) gas atmosphere, which inturn decreases the film deposition rate as compared to pure N_2 gas atmosphere.

The microstructure of TiN/NiTi films was further investigated using high-resolution transmission electron microscopy (HRTEM) at electron beam energy of 200 keV. High resolution lattice images of the samples A, B and C are shown in **Figure 4.4**. It clearly reveals the lattice planes of different orientations for different films. In case of sample A, the lattice image shows a spacing of 2.1 Å, which is in agreement with the value of d spacing of (110) planes, i.e., d_{110} of NiTi. The lattice imaging of the sample B i.e. TiN(111)/NiTi film, reveals the lattice spacing of 2.4 Å **(Figure 4.4(b))**, which corresponds to d_{111} of TiN and sample C i.e. TiN(002)/NiTi film shows lattice spacing of 2.1 Å **(Figure 4.4(c))**, which corresponds to d spacing of (200) planes of TiN. The microstructure of sample B clearly shows the faceted pyramid structure. The estimated average grain size of each sample from TEM images was in agreement with the FESEM results and is reported in **table 4.2**.

To gain further insight, the lattice mismatch between TiN and NiTi was calculated for sample B (TiN (111)/NiTi) and sample C (TiN (200)/NiTi) using
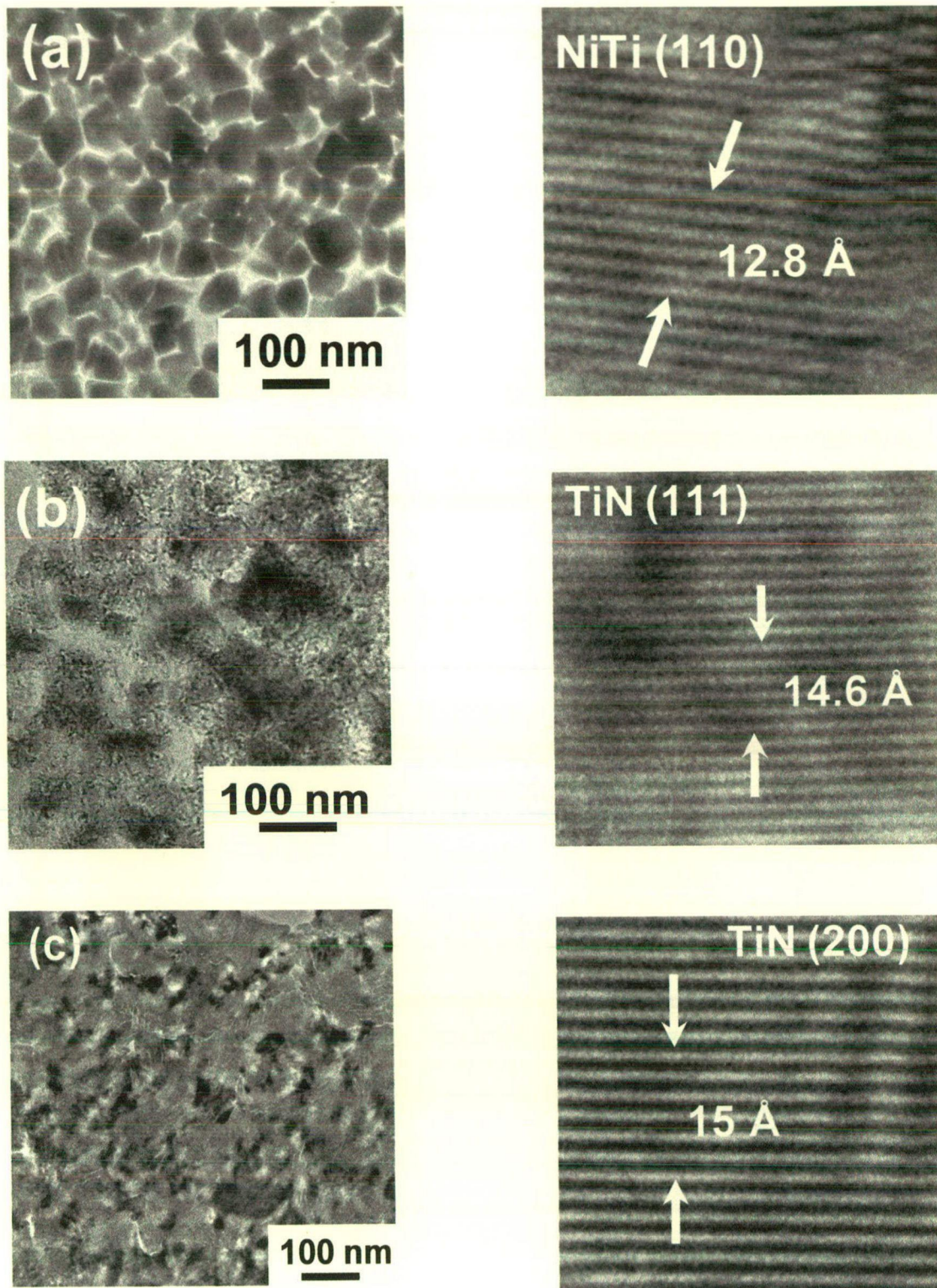
Figure 4.4   High resolution lattice images of **(a)** NiTi film, **(b)** TiN (111)/NiTi and **(c)** TiN (200)/NiTi heterostructures.

Table 4.2   Various parameters of NiTi, TiN (111)/NiTi, TiN (200)/NiTi thin films.

Sample Name	Grain size (nm)		Misfit	Average
	FESEM	TEM	(%)	Roughness AFM (nm)
NiTi	96	82	--	8.12
TiN (111)/NiTi	84	71	0.5	6.45
TiN (200)/NiTi	56	47	0.2	3.74

XRD patterns. The value of lattice mismatch was found to be 0.5% for sample B and 0.2% for sample C. The lattice mismatch and thermal expansion coefficient mismatch between NiTi and TiN layer could give rise to additional strain in the TiN/NiTi films. The reported value of thermal expansion coefficient for martensite NiTi, austenite NiTi and TiN is 7×10^{-6}, 11×10^{-6} and 9.4×10^{-6}/K respectively (**15, 16**), which elucidate that thermal expansion coefficient mismatch between austenite NiTi and TiN is even less as compared to austenite NiTi and martensite NiTi. This reflects that strain arises due to lattice mismatch and thermal expansion coefficient mismatch in NiTi films due to top TiN layer is not detrimental to the adherence of TiN over NiTi and TiN is a good candidate for surface passivation of NiTi films. Further to examine the effect of TiN protective coatings on phase transformation behavior and mechanical properties of NiTi films, a comparative studies of electrical resistance and nanoindentation measurements were carried out systematically on NiTi films, TiN (111)/NiTi and TiN (200)/NiTi heterostructures.

4.3.2   Electrical properties

Figure 4.5 (a) shows the electrical resistance versus temperature (R-T) plot of the pure NiTi thin film (Sample A) deposited at $T_s = 823$ K. Hysteresis behavior of the electrical resistance during heating and cooling of SMA could possibly be due to following reasons: (a) volume change during phase transformation; (b) incompatibility between martensite variants and austenite. These transformation processes take place according to the following procedures:
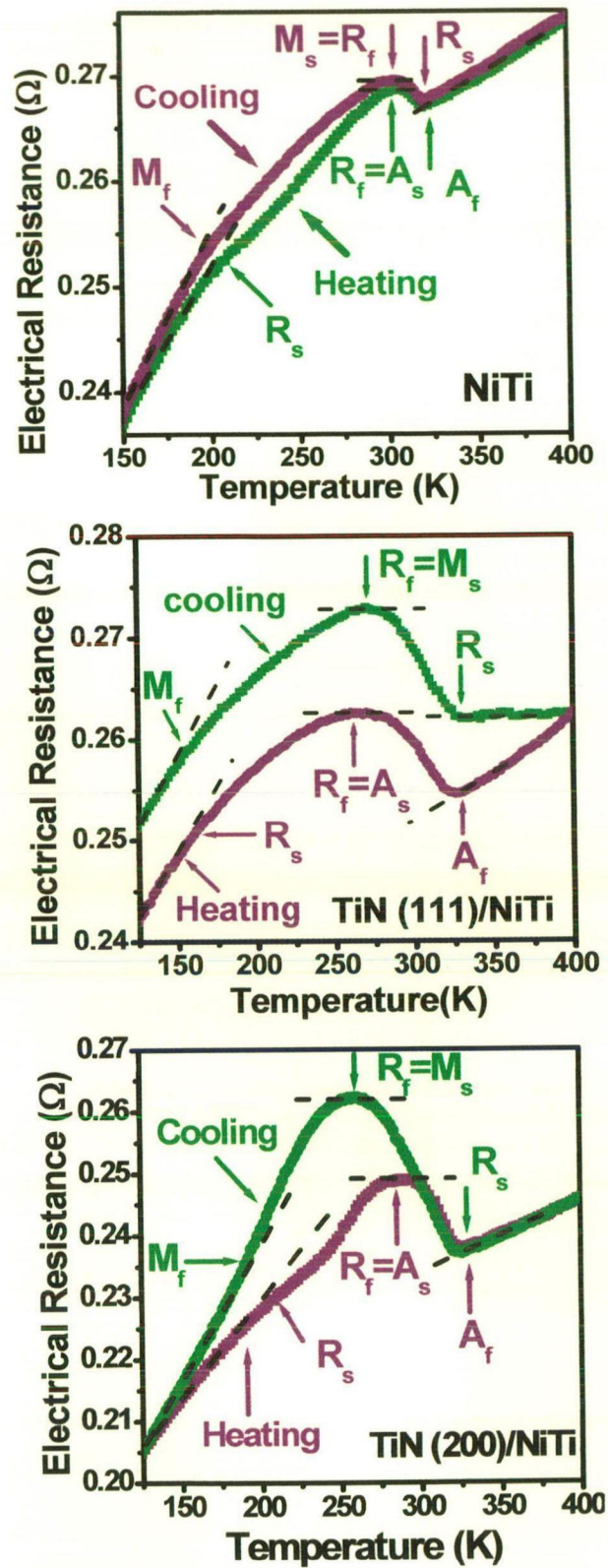
Figure 4.5   Electrical resistance versus temperature curve of **(a)** NiTi film, **(b)** TiN (111)/NiTi and **(c)** TiN (200)/NiTi heterostructures.

Table 4.3 Details of transformation temperatures obtained from electrical resistance versus temperature curves of NiTi, TiN (111)/NiTi and TiN (200)/NiTi thin films.

Sample Name	Transformation Temperature (K)						Hystresis
	Heating			Cooling			Width (K)
	R_s	$R_f = A_s$	A_f	R_s	$R_f = M_s$	M_f	
NiTi	208	302	320	318	304	200	18
TiN (111)/NiTi	164	264	326	328	270	158	80
TiN (200)/NiTi	206	286	326	322	260	192	62

M-phase → R-phase → B2 phase (during heating)

B2 phase → R-phase → M-phase (during cooling)

The values of M_s (the martensite start temperature) and A_f (austenite finish temperature) were found to be 304 and 320 K for sample A; 270 and 326 K for sample B; 260 and 326 K for sample C, respectively (**table 4.3**). The peak in the electrical resistivity curve confirms the formation of R-phase during phase transformations.

Figure 4.5 (b) and **(c)** shows the electrical resistance versus temperature plot of TiN (111)/NiTi (Sample B) and TiN (200)/NiTi (Sample C) heterostructure respectively. Hysteresis width were found to be 18K, 80K and 62K for samples A, B and C, respectively and it was observed that TiN coated NiTi films showed large hysteresis as compared to pure NiTi film, which could be due to constraints effect in NiTi films due to top TiN protective layer. Austenite transition temperature did not get much affected by the deposition of TiN protective layer over NiTi film while martensite transformation temperature shifted towards lower temperature. In case of TiN (111)/NiTi film, it was observed that the martensite final (M_f) temperature is approx. 158 K and hysteresis loop was not closed even at 90 K, which could be due to large residual stress in the deposited film. Residual stress in the deposited film is attributed to the intrinsic stress formed during film nucleation and growth, lattice mismatching and due to small grain size of top nanocrystalline TiN protective layer.

4.3.3 Mechanical properties

Figure 4.6 shows the normalized indentation load-depth curves for NiTi, TiN (111)/ NiTi, TiN (200)/NiTi thin films at three different temperatures of 298, 323 and 380 K. **Figure 4.6 (b)** and **(c)** exhibit a deflection in load-displacement curve at the contact depth of ~ 80 nm (shown by the circle), which could be due to the transition from upper TiN layer to underneath NiTi layer. The indentation induced superelastic energy recovery ratio (η_w) was also calculated using following relation **(17)**:

$$\eta_w = \frac{W_e}{W_t} = \frac{\displaystyle\int_{h_r}^{h_{max}} F dh}{\displaystyle\int_0^{h_{max}} F dh} \qquad (4.2)$$

where W_e is the reversible work and W_t is the total work done. Superelastic energy recovery ratio at room temperature was found to be 0.44, 0.42 and 0.49 for pure NiTi, TiN (111)/NiTi and TiN (200)/NiTi films, respectively. Low values of superelastic recovery under Berkovich tip were expected due to the generation of high peak strain levels below the tip that generates high density of dislocations through the conventional plastic deformation. High dislocation density stabilize the parent phase and prevent its transformation to martensite thus the high peak strains under a sharp indenting tip inhibit the superelastic recovery. The highest value of indent depth recovery ratio in NiTi using Berkovich indenter has been reported to be 45 % at low loads **(18)**. Inset of **figure 4.6** depicts the temperature dependence of superelastic energy recovery ratio (η_w). It was observed that TiN/NiTi films also exhibit SE energy recovery ratio as comparable to pure NiTi film, which could be due to combined composite properties from top nanocrystalline TiN layer and underneath NiTi layer.
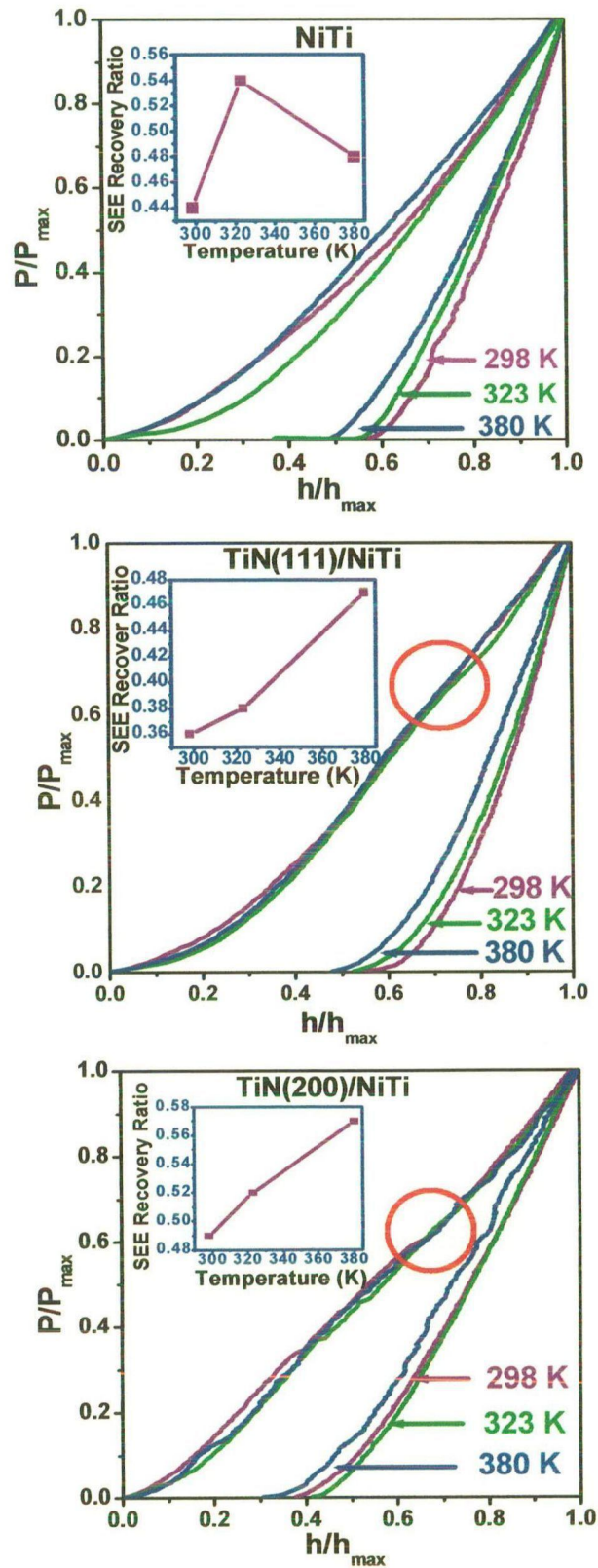
Figure 4.6   Normalized indentation load versus depth curves of **(a)** NiTi film, **(b)** TiN (111)/NiTi and **(c)** TiN (200)/NiTi heterostructures.

Table 4.4   Comparison of nanoindentation results for NiTi, TiN (111)/NiTi and TiN (200)/NiTi thin films.

Sample Name	Temperature (K)	Hardness (GPa)	Reduced Modulus (E_r) (GPa)	H/E_r
Sample A NiTi	298	7.3 ±0.6	134.8 ± 6.4	0.054 ± 0.002
	323	8.0 ± 1.2	123.2 ± 8.9	0.065 ± 0.004
	380	7.8 ± 1.1	102.6 ± 7.4	0.076 ± 0.004
Sample B TiN (111)/NiTi	298	5.9 ± 0.7	123.6 ± 8.7	0.047 ± 0.003
	323	6.1 ± 0.9	126.1 ± 8.9	0.048 ± 0.003
	380	6.6 ± 1.1	128.7 ± 10.3	0.051 ± 0.004
Sample C TiN (200)/NiTi	298	12.0 ± 0.8	139.8 ± 4.0	0.086 ± 0.003
	323	12.2 ± 1.0	140.2 ± 7.2	0.087 ± 0.004
	380	12.7 ± 0.9	142.6 ± 9.7	0.089 ± 0.004

The average hardness (H) and reduced elastic modulus (E_r) as reported in **table 4.4** were calculated for each sample using indentation load-depth curves at 298, 323 and 380 K. Sample C was found to exhibit maximum hardness (12.0 +/- 0.8 GPa) and elastic modulus (139.8 +/- 4.0 GPa). Hardness (H) to Young modulus (E) ratio has been proposed as the key factor to measure the behavior of wear resistance of bilayer coatings. It has been reported that the deformation around the indenter surface exhibit piling-up and sinking-in and the tendency of sinking-in increases with increasing H/E ratio **(18)**. **Figure 4.7 (c)** shows the bar chart of H/E ratio at room temperature for samples A, B and C. A relative low value of H/E ratio (0.054) for pure NiTi films indicate that more fraction of work is consumed in plastic deformation and large plastic strain is expected when contacting a material. In case of TiN (200)/ NiTi film, the H/E ratio (0.086) was found to be higher as compared to NiTi and TiN (111)/NiTi, which indicate that the TiN (200) passivated NiTi exhibit better wear resistance.
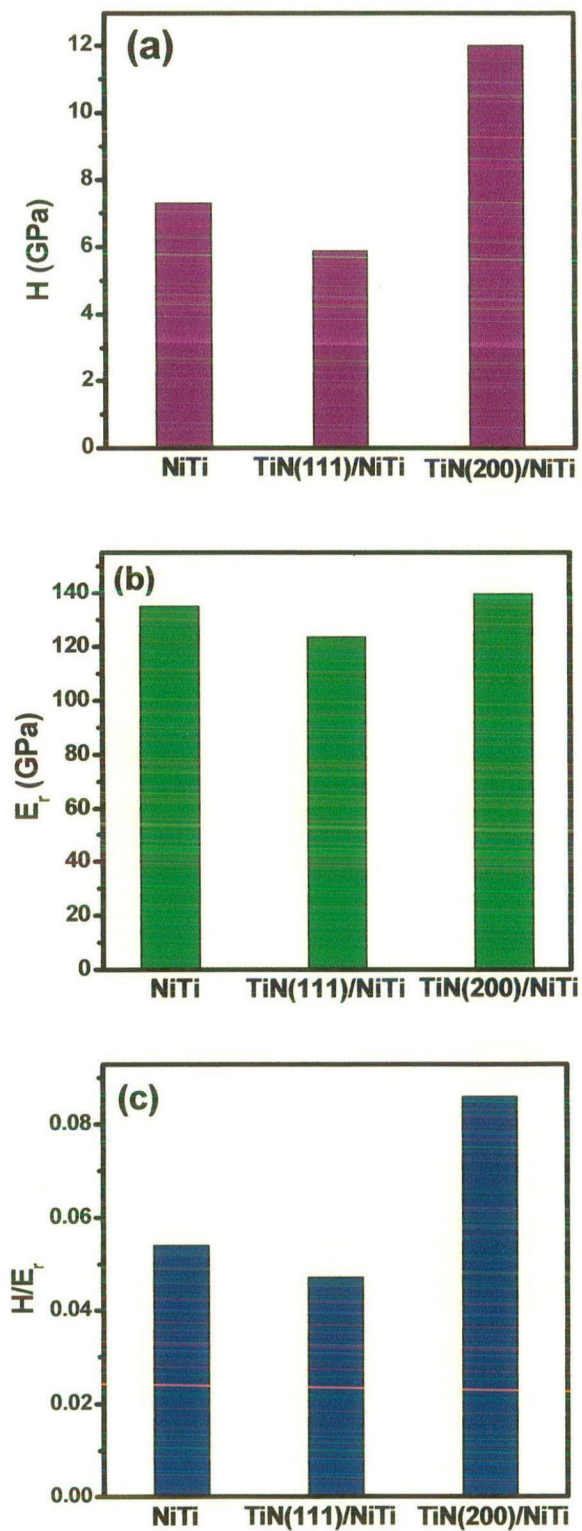
Figure 4.7   Bar chart of hardness (H), reduced modulus (E_r) and hardness to reduced modulus ratio curves at 298 K for samples A, B & C.

The dissipation energy in each indentation cycle was evaluated from numerical integration of the area between the loading and unloading curves. **Figure 4.8** shows the response of dissipation energy of sample A, B and C as a function of indentation cycle. In case of pure NiTi films, a slight initial decrease in the energy dissipation was observed that could be due to less mechanical work required to overcome the internal stress caused by the strain mismatch. Beyond a certain number of indentation cycles, i. e. 10-12, there was a slight increase in the dissipation energy and thereafter a stable steady state response was achieved for 12-16 cycles. A similar behavior of dissipation energy with loading cycle has been reported by M. Dolce et al **(19)** in case of their bulk austenitic NiTi alloys.

Figure 4.9 shows the surface topographical insitu-images taken over 20 μm x 20 μm using atomic force microscope in conjunction with nanoindenter for samples A, B and C. Images clearly reveals the sign of remnant impression of nanoindent on the surface of each sample and also indicate that the aggregate grain size distribution is reasonably uniform. The surface roughness was found to be minimum in case of TiN (200)/NiTi film (Sample C). Estimated values of average surface roughness were observed to be 8.12 nm, 6.45 nm and 3.74 nm for sample A, B and C respectively.
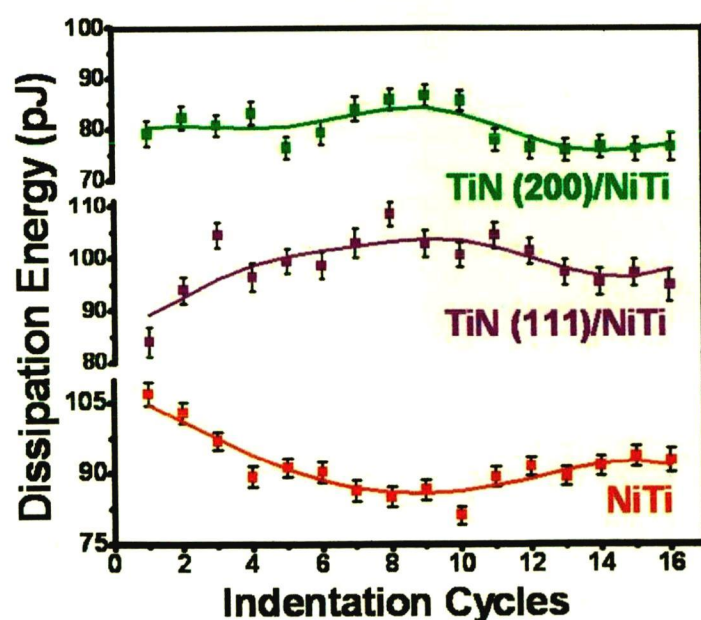
Figure 4.8   Dissipation energy versus indentation cycle for samples A, B and C at room temperature.
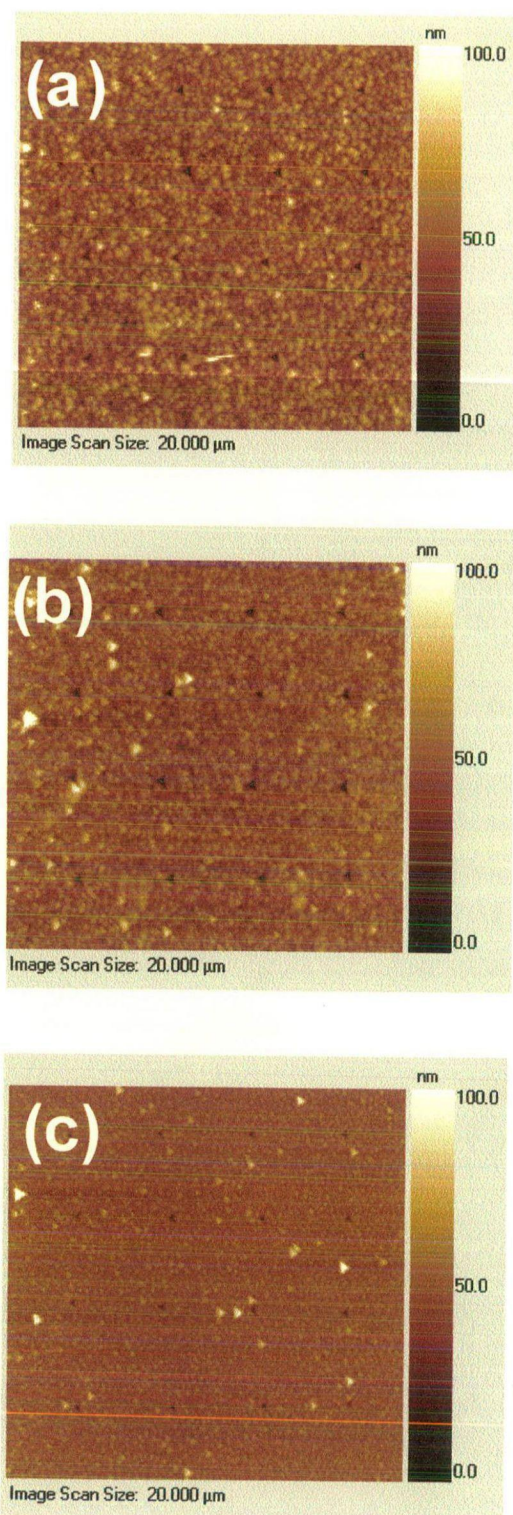
Figure 4.9   Surface topographical insitu images taken over 20 µm x 20 µm using AFM in conjunction with nanoindenter for **(a)** NiTi film, **(b)** TiN (111)/NiTi and **(c)** TiN (200)/NiTi heterostructures.

106

4.4   Conclusion

In summary, both NiTi and TiN/NiTi films with strong preferred in plane orientation were successfully grown on Si substrate by dc magnetron sputtering. The preferential orientation of the TiN films was observed to change from (111) to (200) with change in composition of sputtering gas. The shape of the crystallite was also observed to change from a faceted pyramid to non-faceted spherelike structure with change in crystallographic orientation of nanocrystalline TiN from (111) to (200). A systematic study was performed to see the influence of crystallographic orientation of TiN passivation layer on the structural, mechanical and electrical properties of NiTi thin films. The observation shows that phase transformation take place in TiN/NiTi heterostructure even after coating with protective TiN layer. TiN/NiTi films were observed to show large hysteresis compared to pure NiTi films, which could be due to constraint effect in NiTi films because of top TiN layer. Nanoindentation studies reveal relatively low surface roughness, high hardness, high reduced elastic modulus and thereby better wear behaviour for TiN (200)/NiTi thin films as compared to pure NiTi and TiN (111)/NiTi films. Therefore, the presence of nanocrystalline TiN layer with preferred (002) orientation on NiTi based shape memory thin films improves the surface and mechanical properties, while retaining the phase transformation effect.

4.5 References

(1) Humbeeck J. V., "Shape Memory Alloys: A Material and a Technology", Advanced Engineering Materials, 3, 837-850 (2001).

(2) Humbeeck J. V. and Stalmans R., "Shape memory alloys types and functionalities", Wiley, p. 951 (2002).

(3) Gill J. J., Chang D. T., Momoda L. A. and Carman G. P., "Manufacturing issues of thin film NiTi microwrapper", Sensors and Actuators A, 93, 148-156 (2001).

(4) Zhao X., Cai W. and Zhao L., "Corrosion behavior of phosphorus ion-implanted Ni50.6Ti49.4 shape memory alloy", Surface and Coating Technology, 155, 236-238 (2002).

(5) Wu S. K., Chu C. L. and Lin H. C., "Ion nitriding of TiNi shape memory alloys I. Nitriding parameters and microstructure characterization", Surface and Coating Technology, 92, 197-205 (1997).

(6) Hernandez R., Polizu S., Turenne S. and Yahia L. H., "Characteristics of porous nickel-titanium alloys for medical applications", Bio-Medical Materials and Engineering, 12, 37-45 (2002).

(7) Fu Y., Du H. and Zhang S., "Deposition of TiN layer on TiNi thin films to improve surface properties", Surface and Coating Technology, 167, 129-136 (2003).

(8) Shabalovskaya S. A., "Surface, corrosion and biocompatibility aspects of Nitinol as an implant material", Bio-Medical Materials and Engineering, 12, 69-109 (2002).

(9) Thompson A., "An overview of Nickel-Titanium alloys used in dentistry" International Endodontic Journal, 33, 297-310 (2000).

(10) Stüber M., Albers U., Leiste H., Seemann K., Ziebert C. and Ulrich S., "Magnetron sputtering of hard Cr–Al–N–O thin films", Surface & Coatings Technology, 203, 661–665 (2008).

(11) Chandra R., Kaur D., Chawla A. K., Phinichka N. and Barber Z. H., "Texture development in Ti-Si-N nanocomposite thin films", Material Science and Engineering A, 423, 111-115 (2006).

(12) Pelleg J., Zevin L. Z. and Lungo S., "Reactive-sputter-seposited TiN films on glass substrate", Thin Solid Films, 197, 117-128 (1991).

(13) Sumi H., Inoue H., Aguchi M. T., Sugano Y., Masuya H., Ito N., Kishida S. and Tokutaka H., "Characteristics of TiN films sputtered under optimized conditions of metallic mode deposition", Japanese Journal of Applied Physics, 36, 595-90 (1997).

(14) Maissel L. I. and Glang R., "Handbook of Thin Film Technology", Mcgrath Hill, (1970).

(15) Uchil J., Mohanchandra K. P., Kumara K. G., Mahesh K. K. and Murali T. P., "Thermal expansion in various phases of Nitinol using TMA", Physica B, 270, 289-297 (1999).

(16) Cheng Y. H., Tay B. K. and Lau S. P., "Influence of deposition temperature on the structure and internal stress of TiN films deposited by filtered cathodic vacuum arc", Journal of Vacuum Science and Technology A, 20, 1270-1274 (2002).

(17) Ni W., Cheng Y. T. and Grummon D. S., "Microscopic superelastic behavior of a nickel-titanium alloy under complex loading conditions", Applied Physics Letters, 82, 2811-2813 (2003).

(18) Ni W., Cheng Y. T., Lukitsch M. J., Weiner A. M., Lev L. C. and Grummon D. S., "Effects of the ratio of hardness to Young's modulus on the friction and wear behavior of bilayer coatings", Applied Physics Letter, 85, 4028-4030 (2004).

(19) M. Dolce and D. Cardone, "Mechanical behavior of shape memory alloys for seismic applications", International Journal of Mechanical Sciences, 43, 2631-2656 (2001).

Chapter 5

TiN/NiTi
Heterostructures for
Biomedical Applications

CHAPTER 5

TiN/NiTi HETEROSTRUCTURES FOR BIOMEDICAL APPLICATIONS

5.1   Introduction

In recent years the electrodes modified with various nanomaterials have been used for the electrochemical sensing of biologically important compounds as the surface modification has been found to exhibit electrocatalytic effect (1-5). As electrochemical methods are used to study various electrochemical properties (6-8), but these have distinct advantages (9, 10) over other conventional methods for determination of dopamine (DA), a catecholamine neurotransmitter generated in various parts of central and peripheral nervous system, hence, careful monitoring of dopamine concentration is considered necessary. Parkinson's disease, associated with tremor, rigidity, bradykinesia and postural instability, is one of the most dreadful neurodegenerative disorders of central nervous system (CNS). The disease occurs when dopaminergic neurons decrease or malfunction which is accompanied by a sharp decline in dopamine level (11, 12). Therefore, in the present investigation, the prepared nanocrystalline thin films have been tested for first time as working electrode for dopamine sensing.

5.2   Experimental details

The electrochemical experiments were performed with BAS (Bioanalytical Systems, West Lafayette, IN, USA) CV-50W Voltammetric analyzer. A conventional three electrode glass cell was used with a platinum wire as an auxiliary electrode, Ag/AgCl electrode as reference (model MF- 2052 RB-5B) and TiN or TiN/NiTi coated silicon as working electrodes. The nanocrystalline thin film deposited on silicon substrate was connected to a thin copper strip (5 mm × 60 mm) and molded between two pieces of scotch tape of size 50 mm × 18 mm. One side of the tape was punched for 3 mm diameter hole to provide the contact of films with the solution. The electrode was then ready for use and was kept in air with contact side upwards. All measurements were carried out at room temperature. Dopamine (DA) was purchased from Sisco Research Laboratory, India. All other reagents used were of analytical grade. All solutions were prepared in double distilled water. Phosphate buffer solutions were prepared according to the method of Christian and Purdy (13) and the final pH of the solutions was recorded with the pre-calibrated digital pH

meter. Stock solution of dopamine (DA) was prepared in doubly distilled water. Required amount of the stock solution was added to 2 ml of phosphate buffer solution (μ = 1.0 M, pH = 7.2) and the total volume was made to 8.0 ml with double distilled water. The electrochemical measurements were then carried out with voltammetric analyser. Differential pulse voltammetry employed had the following parameters: Initial E: 0 mV, Final E: 750 mV, Sweep rate: 20 mV/s, Sensitivity: 10 μA/V. The Corrosion behaviour of pure NiTi and TiN/NiTi films were recorded in 1M NaCl solution. Before measurement, each sample was immersed in to the electrolyte for 20 min. The sample area exposed to the electrolyte was 0.0707 cm^2 (3 mm diameter).

5.3   Electrochemical properties

5.3.1   Voltammetric behavior of dopamine

It was observed that TiN (200), TiN (200)/NiTi and TiN (111)/NiTi coated silicon electrode exhibit a sharp oxidation peak for dopamine at E_p ~ 400, 380, and 365 mV, respectively which is much lesser than oxidation peak potential observed at bare silicon (800 mV) as shown in **figure 5.1 (a)** and **(b)**. On the contrary, NiTi coated silicon does not show any oxidation peak for dopamine in the potential range 0-1000 mV (**Figure 5.1 (a)**). Since both the TiN/NiTi coated silicon electrodes showed better response for dopamine oxidation, a systematic concentration study of the dopamine was carried out at TiN (200)/NiTi coated silicon electrode in the concentration range 1-10 μM. The peak current was found to increase with increase in concentration of dopamine as shown in **figure 5.2**. The linear dependence of peak current on concentration (**figure 5.3**) can be represented by the relation:

$$i_p = 5.059 \, [DA] + 6.874 \tag{5.1}$$

where i_p is the current in nA and [DA] is the concentration of dopamine in μM. The correlation coefficient for the linear relation was 0.995. It was observed that TiN/NiTi exhibit dominant catalytic behavior as compared to TiN/Si film. One of the reasons for this behavior could be the fact that these films are deposited at high
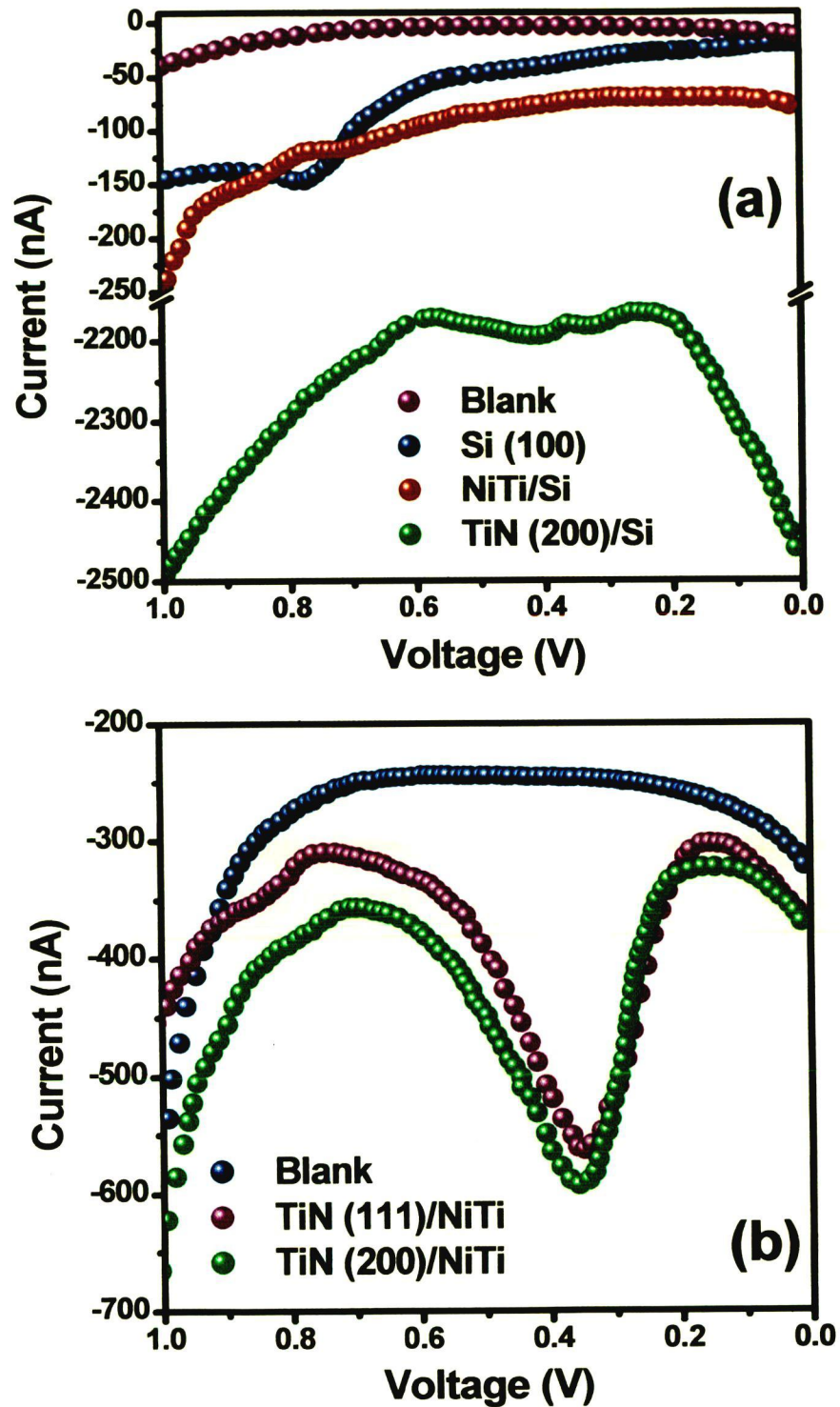
Figure 5.1   A comparison of voltammogram of dopamine at pH 7.2 at different working electrodes **(a)** Si (100), NiTi and TiN (200); **(b)** TiN (111)/NiTi and TiN (200)/NiTi.
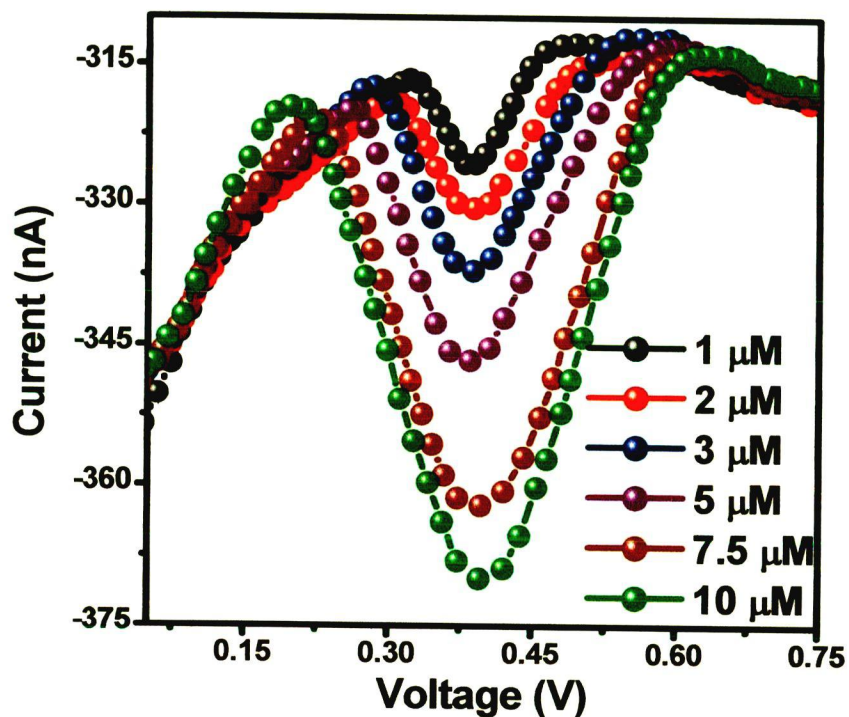
Figure 5.2   Voltammograms of dopamine at different concentration using TiN (200)/NiTi as working electrode.

$$I_p = 5.059*[DA] + 6.874$$
$$R^2 = 0.99534$$
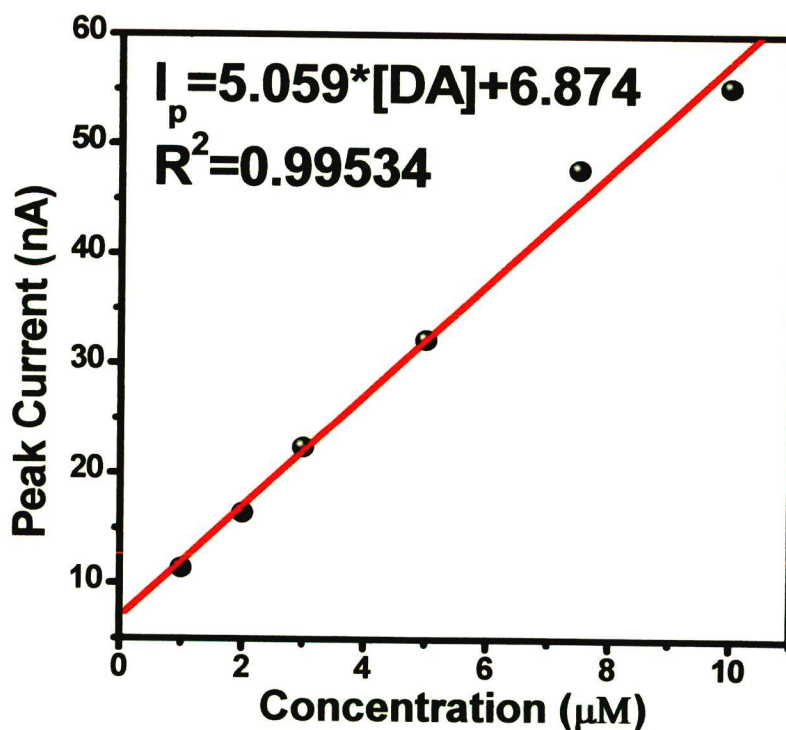
Figure 5.3   Observed dependence of peak current on concentration of dopamine at TiN (200)/NiTi.

116

substrate temperature (T_s = 823 K), hence, there are favorable chances of silicon diffusion in TiN film that can be responsible for the suppression of catalytic activity of TiN. While in the case of TiN/NiTi, NiTi is acting as a buffer layer and prevent the silicon diffusion to upper TiN film. Also the calculated value of lattice mismatches for TiN (111)/NiTi and TiN (200)/NiTi and was found to be 0.5% and 0.2%, respectively. Therefore, it is concluded that NiTi does not exhibit catalytic activity but acts as a good buffer layer and prevents the silicon diffusion to upper TiN layer.

5.3.2 Interference effect

Biological samples contain many electroactive metabolites, which can interfere in voltammetric determination of any compound. Among these ascorbic acid and uric acid are most abundantly present in biological samples. Hence, the effect of these two common interferents, which may interfere with determination of dopamine in blood or urine samples was also studied using TiN (200)/NiTi coated silicon electrode. It was found that ascorbic acid and uric acid showed well-defined peaks at modified electrode with Ep ~ 608 and 812 mV vs Ag/AgCl, respectively. To check the interference of these two compounds, voltammograms were recorded at fixed

Table 5.1   Effect of interferents on peak current of 5µM dopamine at pH 7.2.

Interferent	Concentration of inteferents (µM)	Peak current (i_p) of Dopamine (µA)	Change in i_p of Dopamine (µA)	Change in i_p of Dopamine (%)
Ascorbic Acid	50	0.351	0.005	1.4
	125	0.353	0.007	2.1
	250	0.356	0.010	2.8
	500	0.363	0.017	4.9
Uric Acid	50	0.349	0.003	1.1
	125	0.341	-0.005	1.4
	250	0.355	0.009	2.6
	500	0.360	0.014	4.2

concentration of dopamine (5 µM) with varying concentration of ascorbic acid and uric acid. It was found that peak current of dopamine remained practically unaffected when ascorbic acid and uric acid were added in the concentration range 50-500 µM as shown in **table 5.1**.

On the basis of the observations presented in **table 5.1**, it can ce concluded that ascorbic acid and uric acid do not interfere with voltammetric determination of dopamine even when they are in 100 fold excess with respect to dopamine. However, further increase in concentration of ascorbic acid beyond 100 times excess, oxidation peak of ascorbic acid showed a tendency to merge with oxidation peak of dopamine.

5.3.3   Stability of modified electrode

Stability and reproducibility of an electrode are the two important features which should be evaluated for analytical purpose. TiN (111)/NiTi and TiN (200)/NiTi coated silicon electrodes were tested for both the features so that a time period can be recommended for assured and accurate use of modified electrode. The variation in current response was observed for six successive sweeps in a solution of fixed concentration to check the reproducibility of the electrode. It was noticed that the current was within 97- 99 % of the i_p observed for the first sweep. To determine long term stability of TiN/NiTi coated silicon electrode, current response of dopamine was monitored daily for one week. The electrode was kept in dry conditions after use and it was found that the electrode retained 96 − 99 % current for first three days. After three days, a considerable decline in the peak current was observed and only 91-95 % of initial i_p was recorded. Thus, the electrode can be used for approximately three days without any significant error.

5.3.4   Corrosion resistance

Potentiodynamic polarization curves of NiTi, TiN (111)/NiTi and TiN (200)/NiTi films are shown in **figure 5.4**. The corrosion resistance of TiN coated NiTi films were found to be improved, which can be observed by a shift of whole polarization curve towards the region of lower current density and higher potential. The values of corrosion potential and corrosion current density were found to be 0.635 V and 1.1 X
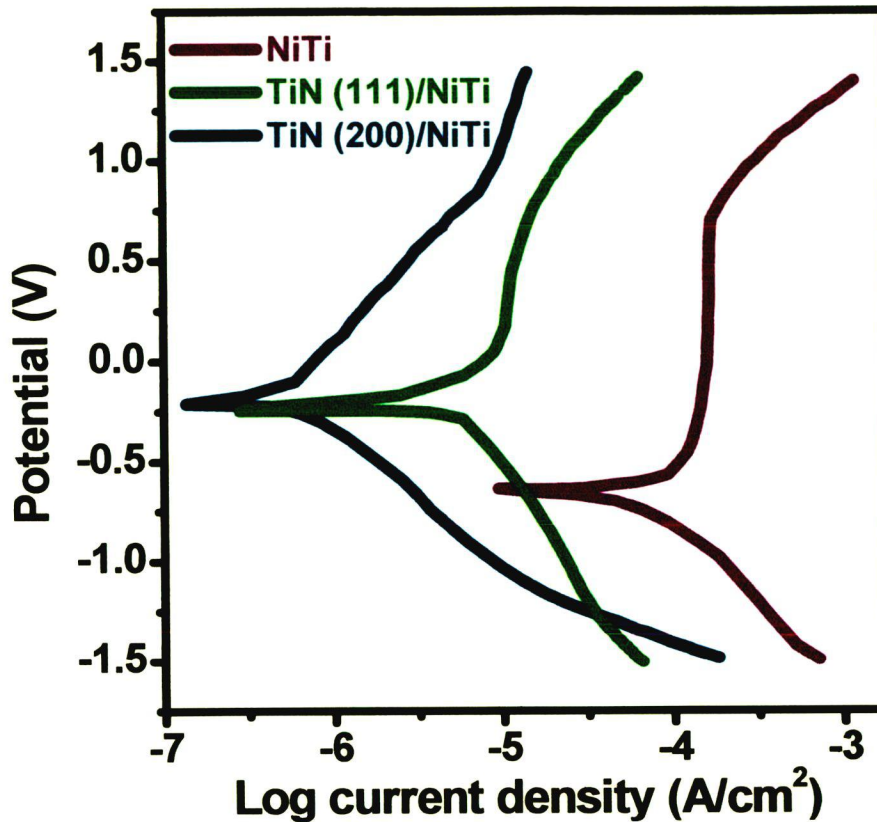
Figure 5.4   Potentiodynamic polarization curves of NiTi, TiN (111)/NiTi and TiN
(200)/NiTi films

10^{-5} A-cm^{-2} for pure NiTi film, 0.248 V and 2.8 X 10^{-7} A-cm^{-2} for TiN (111)/NiTi
film and 0.212 V and 1.4 X 10^{-7} A-cm^{-2} for TiN (200)/NiTi film, respectively. High
corrosion potential and low corrosion current density of the TiN coated NiTi films
suggests that these films exhibit a low corrosion rate and a good corrosion resistance.
TiN (200)/NiTi film exhibited better corrosion resistance than that of TiN (111)/NiTi
film, which could be due to the fact that TiN (200) coated film exhibit lower
surface roughness and lower inhomogeneous surface. The higher surface roughness
and inhomogeneities responsible for weak points on the surface cause corrosive
attacks.

5.4   Conclusion

Electrochemical test reveal that TiN coated NiTi film exhibited better
corrosion resistance as compared to pure NiTi film. It was also observed that TiN

119

(200)/NiTi coated silicon electrode showed better response as compared with NiTi coated silicon with straight line calibration in dopamine concentration range 1–10 μM. One of the probable reasons for this observation is that as TiN (200)/NiTi film exhibits higher real surface area due to small grain size as compared to NiTi film. TiN (200)/NiTi film showed better oxidation peak even at low concentration of dopamine. A significant decrease in peak potential was also observed at modified electrode. An advantage of using these nanocrystalline films in comparison to conventional films used for surface modification is that the films are sufficiently stable and do not require frequent replacements. Such replacement not only requires sufficient time but may also lead to change in the area of the electrode. In addition the films exhibit excellent electrocatalytic behavior. Thus, it is concluded that use of nanocrystalline TiN layer with preferred (200) orientation on NiTi thin films improves electrocatalytic properties and hence can be successfully used as working electrode in voltammetric determination of biomolecules.

5.5   References

(1) Goyal R. N., Bachheti N., Tyagi A. and Pandey A. K., "Differential pulse voltammetric determination of methylprednisolone in pharmaceuticals and human biological fluids", Analytica Chimica Acta, 605, 34-40 (2007).

(2) Goyal R. N., Oyama M. and Singh S. P., "Fast determination of salbutamol, abused by athletes for doping, in pharmaceuticals and human biological fluids by square wave voltammetry", Journal of Electroanalytical Chemistry, 611, 140-148 (2007).

(3) Tao Y., Lin Z., Chen X., Huang X., Oyama M., Chen X. and Wang X., "Functionalized multiwall carbon nanotubes combined with bis(2,2'-bipyridine)-5-amino-1,10-phenanthroline ruthenium(II) as an electrochemiluminescence sensor", Sensors and Actuators B: Chemical, 129, 758-763 (2008).

(4) Goyal R. N., Gupta V. K. and Chatterjee S., "Simultaneous determination of adenosine and inosine using single-wall carbon nanotubes modified pyrolytic graphite electrode", Talanta, 76, 662-668 (2008).

(5) Zhang J. and Oyama M., "Gold nanoparticle-attached ITO as a biocompatible matrix for myoglobin immobilization: Direct electrochemistry and catalysis to hydrogen peroxide", Journal of Electroanalytical Chemistry, 577, 273-279 (2005).

(6) Verma A., Joshi A. G., Bakhshi A. K., Shivaprasad S. M. and Agnihotry S. A., "Variations in the structural, optical and electrochemical properties of CeO_2-TiO_2 films as a function of TiO2 content", Applied Surface Science, 252, 5131-5142 (2006).

(7) Kamachi U. M., Bhuvaneswaran N., Shankar P. and Raj B., "Corrosion behavior of intermetallic aluminide coatings on nitrogen-containing austenitic stainless steels", Corrosion Science, 46, 2867-2892 (2004).

(8) Das S. R., Fachini I. R., Majumder S. B. and Katiyar R. S., "Structural and electrochemical properties of nanocrystalline $Li_xMn_2O_4$ thin film cathodes ($x = 1.0-1.4$)", Journal of Power Sources, 158, 518-523 (2006).

(9) Goyal R. N. and Singh S. P., "Simultaneous voltammetric determination of dopamine and adenosine using a single walled carbon nanotube - Modified glassy carbon electrode", Carbon, **46**, 1556-1562 (2008).

(10) Goyal R. N., Gupta V. K., Oyama M. and Bachheti N., "Gold nanoparticles modified indium tin oxide electrode for the simultaneous determination of dopamine and serotonin: Application in pharmaceutical formulations and biological fluids", Talanta, **72**, 976-983 (2007).

(11) Dawson T. M. and Dawson V. L., "Molecular Pathways of Neurodegeneration in Parkinson's Disease", Science, **302**, 819-822 (2003).

(12) Shih M. C., Hoexter M. Q. and Andrade L. A. F., "Parkinson's disease and dopamine transporter neuroimaging - A critical review", Revista Paulista de Medicina, **124**, 168-175 (2006).

(13) Christian G. D. and Purdy W. C., "The residual current in orthophosphate medium", Journal of Electroanalytical Chemistry, **3**, 363-367 (1962).

Chapter 6

Conclusion & Future Prospects

CHAPTER 6

CONCLUSION AND FUTURE PROSPECTS

6.1 **Grain size effect on structural, electrical and mechanical properties of NiTi shape memory alloy thin films**

6.2 **Influence of film thickness on phase transformation behavior of sputtered NiTi shape memory alloy thin films**

6.3 **Effect of crystallographic orientation of nanocrystalline TiN on structural, electrical & mechanical properties of TiN/NiTi heterostructures**

6.4 **Bio-medical application of TiN/NiTi heterostructures**

The main aim of the present study was to synthesize the device quality NiTi shape memory thin films and TiN/NiTi heterostructures on silicon substrate by dc magnetron sputtering technique in order to (i) study the influence of grain size and film thickness on the texture, surface morphology and phase transformation behavior of NiTi thin films; (ii) study the effect of crystallographic orientation of nanocrystalline TiN thin film on structural, electrical and mechanical properties of TiN/NiTi heterostructures and (iii) demonstrate the bio-medical applications of TiN/NiTi heterostructures. Brief summary and conclusions based on the results obtained are given below. The suggestions for the future work are proposed at the end.

6.1 Grain size effect on structural, electrical and mechanical properties of NiTi shape memory alloy thin films

We have designed and developed magnetron co-sputtering setup to deposit high quality shape memory alloy thin films. In the present study, NiTi thin films were grown on Si (100) substrate by dc magnetron sputtering in the temperature range from room temperature to 923 K. Substrate temperature was found to have a great impact on surface morphology, crystallite size, mechanical properties and phase transformation behavior of these films. XRD pattern showed that the film deposited at T_s of 623 K was amorphous in nature while the film deposited at 723 and 823 K exhibited the reflection from (110) plane of the austenite phase. With further increase in deposition temperature to 923 K, reflection from (-111), (002) and (110) planes of martensite structure was observed. Surface morphology of these films were found to change from non facet grains to facet grains with preferential in-plane orientation (martensite plates) with change in substrate temperature from 823 to 923 K. The NiTi film deposited at substrate temperature (T_S) of $\leq$ 623 K exhibited negative TCR value and non-metallic behavior while the film deposited at T_S of $\geq$ 723 K showed metallic behavior. Electrical resistance versus temperature curves conformed that in a volume containing many small grains, the ability of phase transformation due to autocatalytic nucleation decreases with increase in grain boundary area.

exhibits higher real surface area due to small grain size as compared to NiTi film. TiN (200)/NiTi film showed better oxidation peak even at low concentration of dopamine. A significant decrease in peak potential was also observed at modified electrode. An advantage of using these nanocrystalline films in comparison to conventional films used for surface modification is that the films are sufficiently stable and do not require frequent replacements. Such replacement not only requires sufficient time but may also lead to change in the area of the electrode. In addition the films exhibit excellent electrocatalytic behavior. Thus, it is concluded that use of nanocrystalline TiN layer with preferred (200) orientation on NiTi thin films improves electrocatalytic properties and hence can be successfully used as working electrode in voltammetric determination of biomolecules. Also, electrochemical test reveal that TiN coated NiTi film exhibited better corrosion resistance as compared to pure NiTi film.

Future Directions

Functionally graded NiTi thin films: Variation in Ni/Ti ratio through film thickness

To further improve the properties of NiTi films, functionally graded NiTi films can be fabricated by gradual change in Ni/Ti ratio through the film thickness. As the Ti or Ni content changes in the micrometer-thick film, the material properties could change from pseudo-elastic (similar to rubber) to shape memory. The integration of pseudo-elastic with shape memory characteristics produces a two-way reversible actuation. These functionally graded NiTi films can be fabricated using dc magnetron co-sputtering by slightly changing the target powers during deposition. In order to successfully develop functionally graded NiTi thin films for MEMS application, it is necessary to characterize, model and control the variations in composition, thermomechanical properties and residual stress in these films.

Composite Design: Combination of NiTi and piezoelectric films

Response time of the piezoelectric material is fast but the displacement is relatively small while NiTi films exhibit large force-displacement with slow response frequency. Therefore, a new hybrid heterostructures can be fabricated by coupling NiTi and PZT films. These heterostructures will allow the tuning or tailoring of static and dynamic properties of NiTi thin films, which may generate a larger displacement than conventional piezoelectric thin films and have an improved dynamic response compared with that of single layer NiTi films.